ABSTRACT

Title of Dissertation:	MULTISCALE TECHNOLOGIES FOR ENGINEERING AND CRYOPRESERVING OVARIAN TISSUES AND HUMAN IPSCs
	Samantha Stewart Doctor of Philosophy, 2023
Dissertation directed by:	Professor Xiaoming He, Fischell Department of Bioengineering

An estimated 9.8 million reproductive-age people with ovaries in the United States are impacted by fertility issues, oftentimes caused by the dysregulation of the tightly controlled process of ovarian follicle development. Impaired fertility can arise from disorders like polycystic ovarian syndrome (PCOS) or premature ovarian insufficiency (POI), which affect the function of the ovary, an integral reproductive organ that houses the ovarian follicles. POI can also negatively impact endocrine function, decreasing estrogen and leading to increased risk of osteoporosis, cardiovascular disease, and neurological disorders. Novel fertility preservation and restoration strategies, like ovarian tissue engineering, have emerged to address these effects of ovarian dysregulation and offer alternatives for those who wish to delay childbearing. Human induced pluripotent stem cells (hiPSCs) hold tremendous potential for tissue engineering and cell-based medicine, as they have the capacity of differentiating into ectodermal, mesodermal, endodermal, and germ cell lineages. In recent years, research into differentiating hiPSCs into cells like those that make up the ovary has garnered much interest, highlighting these cells as a promising source

for ovarian tissue engineering and other types of cell-based medicine and research. This work addresses critical challenges associated with engineering ovarian tissue for reproductive and cell-based medicine: (1) engineering the microenvironment for the cell/microtissue and (2) cryopreservation of the cells/microtissues. To understand the microenvironment of the ovary for informed tissue engineering system design, we spatially characterize the micromechanical properties of ovarian tissue from domestic cats to reveal both elastic and viscoelastic property heterogeneities, correlating these findings with the distribution of key extracellular matrix (ECM) molecules. We then developed a novel cryopreservation technology to enhance cryopreservation of ovarian follicles and hiPSCs, using sand to seed ice in the extracellular solution at high subzero temperatures during cooling. Together, this work investigates multiscale strategies for advancing ovarian tissue engineering, contributing to the advancement of reproductive medicine approaches for treating infertility and related endocrine dysfunction.

MULTISCALE TECHNOLOGIES FOR ENGINEERING AND CRYOPRESERVING OVARIAN TISSUES AND HUMAN IPSCs

by

Samantha Stewart

Dissertation submitted to the Faculty of the Graduate School of the
University of Maryland, College Park, in partial fulfillment
of the requirements for the degree of
Doctor of Philosophy
2023

Advisory Committee:
Professor Xiaoming He, Chair
Professor John P. Fisher
Associate Professor Kimberly M. Stroka
Dr. Nucharin Songsasen
Professor Carol Keefer

Acknowledgements

I would like to thank my advisor, Professor Xiaoming He, for his mentorship and all the opportunities and guidance he has provided me over these years.

I would like to thank all the current and former members of the Multiscale Biomaterials and Engineering Laboratory for their help, support, and comradery.

I would like to thank the members of my dissertation committee, Dr. John Fisher, Dr. Kimberly Stroka, Dr. Nucharin Songsasen, and Dr. Carol Keefer, for their help and advice.

I would like to thank the Spay Spa and Neuter Nook for providing the cat ovaries for the work in Chapter 2 – thank you for always being so helpful and friendly to "the ovary lady".

Finally, I could not have done this without the incredible love and support of my partner, friends, and family. Thank you all for sticking by me.

Statement of Contributions

This dissertation presents the accumulated doctoral research of the present author and collaborators. Dr. Xiaoming He, as the advisor, contributed to this dissertation through the conception of ideas, design and troubleshooting of experiments, review of figures, analysis and interpretation of data, editing of draft manuscripts, and finalization of manuscripts for all the work of this dissertation. The contributions of the present author and collaborators are briefly stated below:

Chapter 1: This chapter is an introduction written by the present author.

Chapter 2: This chapter was reproduced from a paper published as Stewart, S., Ou, W., Aranda-Espinoza H., Rahaman S., He, X. Micromechanical characterizations and viscoelastic modeling reveal elastic and viscoelastic heterogeneities in ovarian tissue and the significant viscoelastic contribution to the apparent elastic modulus determined by AFM indentation. *Acta Biomaterialia* 2023; 168: 286-297. The present author carried out all the experiments, created all the figures, analyzed the data, and prepared the draft manuscript with inputs from all other co-authors.

Chapter 3: This chapter was partly reproduced from a paper published as Jiang, B.*, Li, W.*, Stewart, S.*, Ou, W., Liu, B., Comizzoli, P., He, X. Sand-mediated ice seeding enables serum-free low-cryoprotectant cryopreservation of human induced pluripotent stem cells. *Bioactive Materials* 2021; 6(12): 4377-4388. The present author conducted the ice-seeding temperature measurement experiments, wrote the

relevant contents in the draft manuscript, and reviewed the whole manuscript. Jiang, B., and Li, W., conducted the iPSC cryopreservation and viability experiments, iPSC characterization and differentiation experiments, and wrote the relevant contents in the draft manuscript. Ou, W. performed SEM imaging and XDS analysis of the sand-PDMS film. All authors contributed to data analysis and reviewed the manuscript. This chapter was also partly reproduced from a paper prepared as Stewart, S., White, A., Ou, W., Nagashima, J., Songsasen, N., He, X. Sand-mediated ice seeding enhances slow-freezing cryopreservation of preantral ovarian follicles. The present author carried out all experiments, created all the figures, analyzed the data, and prepared the draft manuscript with assistance from all co-authors. White, A., and Ou, W. performed all animal work and retrieval of ovarian tissue from the mice.

Chapter 4: The present author wrote the concise conclusion for this dissertation.

Chapter 5: The present author wrote a future perspective of the studies presented in this dissertation.

Table of Contents

Acknowledgements ii
Statement of Contributions iii
Table of Contents v
List of Tables vii
List of Figures viii
Chapter 1 : Introduction 1
1.1 Ovarian follicles and human induced pluripotent stem cells (hiPSCs) 1
1.2 Engineering the microenvironment of the ovary 3
1.2.1 Micromechanical environment of the ovary 3
1.3 Cryopreservation of ovarian follicles and hiPSCs 5
1.3.1 Cryopreservation of isolated preantral ovarian follicles as an alternative fertility preservation strategy 6
1.3.2 Cryopreservation of hiPSCs 8
1.4 Dissertation overview and outline 9
Chapter 2 : Micromechanical characterizations and viscoelastic modeling reveal both elastic and viscoelastic heterogeneities in ovarian tissue and the significant contribution to the apparent elastic modulus determined by AFM indentation 11
2.1 Introduction 11
2.2 Results and Discussion 13
2.2.1 Heterogeneity of elastic modulus 15
2.2.2 Heterogeneity of viscoelastic properties 20
2.2.3 Significant contribution of viscoelasticity to apparent elastic modulus determined by AFM indentation 24
2.2.4 Possible connection of mechanical and compositional heterogeneities 26
2.3 Conclusions 32
2.4 Materials and Methods 33
2.4.1 Ovary collection 33
2.4.2 Atomic force microscopy (AFM) sample preparation 34
2.4.3 AFM indentation measurements 34
2.4.4 AFM data analysis 36
2.4.5 Ovary fixation and staining 40
2.4.6 Hyaluronic acid quantification 40
2.4.7 Collagen type I quantification 42
2.4.8 Statistical analysis 42
Chapter 3 : Sand-mediated ice seeding enhances slow-freezing cryopreservation of human induced pluripotent stem cells and mouse preantral ovarian follicles 44
3.1 Introduction 44
3.2 Results 48
3.2.1 Fabrication and characterization of sand-PDMS film 48
3.2.2 Ice-seeding with sand-PDMS film 51
3.2.3 Sand-mediated ice-seeding enhances immediate viability of cryopreserved ovarian follicles 56

3.2.4 Sand-mediated ice-seeding enhances in vitro growth of cryopreserved ovarian follicles 57
3.2.3 Enhanced cryopreservation of hiPSCs with sand-mediated ice seeding ... 62
3.2.4 High pluripotency and normal cell cycle of cryopreserved hiPSCs 65
4.2.5 Intact capacity of differentiation of the cryopreserved hiPSCs 66
3.3 Discussion 70
3.4 Conclusions 75
3.5 Materials and Methods 76
3.5.1 hiPSC Cell Culture 76
3.5.2 Isolation of ovarian follicles 76
3.5.3 Fabrication of sand-PDMS film for cryopreservation 77
3.5.4 Surface characterization of the sand-PDMS film 78
3.5.5 Measurement of ice-seeding temperature 79
3.5.6 Cryomicroscopy study of sand-mediated ice formation 79
3.5.7 Cryopreservation of hiPSCs and ovarian follicles 80
3.5.8 Live/dead assay and cell attachment efficiency 82
3.5.9 Teratoma assay for hiPSCs 83
3.5.10 Neural and cardiac differentiation of hiPSCs 84
3.5.11 Flow cytometry analysis of protein marker expression of hiPSCs 85
3.5.12 Cell cycle analysis of hiPSCs 86
3.5.13 In vitro culture of ovarian follicles 86
3.5.14 Statistical analysis 87
Chapter 4 : Conclusions 89
Chapter 5 : Future Research Directions 90
5.1 Impact of viscoelasticity on follicle growth and development 90
5.2 Combining cryopreservation technologies with the sand-PDMS film 91
Publications, and Conference Presentations, and Book Chapters 93
Chapter 6 Appendices 98
Appendix 1: Micromechanical characterizations and viscoelastic modeling reveal elastic and viscoelastic heterogeneities in ovarian tissue and the significant viscoelastic contribution to the apparent elastic modulus determined by AFM indentation 98
Appendix 2: Sand-mediated ice-seeding enhances cryopreservation of human induced pluripotent stem cells and mouse preantral ovarian follicles 104
Appendix 3: Intracellular Delivery of Trehalose for Cell Banking 106
Chapter 7 Bibliography 131

List of Tables

Table 2.1. Ages of cats tested. Ages of cats (in months) tested via AFM characterization to characterize apparent modulus or stress relaxation behavior grouped by reproductive age (younger, <6 months; older, >6 months). 33
Table 2.2 Parameters from viscoelastic modeling of ovarian tissue behavior. Model parameters extracted from fitting second order SLS model to stress relaxation data collected in cortex and medulla of reproductively younger and older cat ovarian tissues. 39

List of Figures

Figure 2.1 A schematic illustration of the characterization of mechanical properties of cat ovarian tissue. A, Schematic of mechanical testing of the cat ovary using atomic force microscopy (AFM) indentation. The ovary was embedded in an agarose gel and bisected to reveal the inner ovarian tissue. A line scan across the ovary was analyzed, mapping the mechanical properties at approximately 200 µm intervals. At each mapping site, force-indentation maps were taken to determine the apparent elastic modulus of the tissue using the Hertz model. Stress relaxation measurements were also performed by AFM indentation at each mapping site. Scale bar = 1 mm. **B**, Representative force-indentation curve that was used for Hertz model fitting to extract the apparent modulus. **C**, 2nd order standard linear solid (SLS) viscoelastic model used for fitting the stress relaxation data. The model is made up of elastic solid elements represented by springs and viscous Newtonian fluid elements represented by dashpots. The model consists of a purely elastic spring arm with modulus Ee in parallel with two viscoelastic Maxwell arms. The first Maxwell arm consists of a solid spring with modulus $E1$ and fluid dashpot with viscosity $\mu 1$. The second Maxwell arm has a solid spring with modulus $E2$ and fluid dashpot with viscosity $\mu 2$. The stress and strain are indicated as σ and ε, respectively. Each of the two Maxwell arms represents a different viscoelastic kinetics with $\tau 1$ and $\tau 2$ as the relaxation time constants, where $\tau 1 = \mu 1/E1$ and $\tau 2 = \mu 2/E2$. D, Extracellular matrix (ECM) characterization of the cat ovary. The representative image shows a fluorescence image of the cat ovary stained for hyaluronic acid (HA). The intensity of HA was quantified across the middle of the ovary, similar to the profile of AFM measurements in panel **A**, represented by the red box. Scale bar: 1 mm. 14

Figure 2.2 Characterization of the apparent elastic modulus of cat ovarian tissue. **A**, Apparent modulus (Ea) of all tested mapping sites (average of all individual force-indentation measurements at mapping site) across all ovaries tested (n=14). **B**, Histogram representing the overall distribution of apparent moduli (Ea, kPa) across all probed ovaries (n>100). The x-axis values correspond to upper limit of the bin (i.e., modulus value). Each value within the histogram represents one analyzed mapping site. Inset shows same data with finer bins, focusing on values from 0-6 kPa. 15

Figure 2.3 Analysis of apparent modulus (Ea, kPa) heterogeneity in cat ovaries. A, Apparent modulus line-scans of reproductively younger ovaries (<6 months, n=7). Each ovary linescan is represented by a different symbol. **B,** Apparent modulus line-scans of reproductively older ovaries (>6 months, n=7). Each ovary linescan is represented by a different symbol. **C,** Normalized apparent modulus line scan profiles of all the seven reproductively younger cat ovaries. The cortex (C, light blue shading) is noted as 0.0 – 0.3, and 0.7 – 1.0 of the tissue based on normalized position. The medulla (M, darker shading) is noted as 0.3 – 0.7 of the tissue based on normalized position. **D,** Normalized apparent modulus line scan profiles of all the seven reproductively older cat ovaries. The cortex (C, light orange shading) is noted as 0.0 – 0.3, and 0.7 – 1.0 of the tissue based on normalized position. The medulla (M, darker shading) is noted as 0.3 – 0.7 of the tissue based on normalized position. **E**, Individual apparent modulus for the cortex (C) and medulla (M) areas of each

reproductively younger (Y) cat ovary tested. **F**, Individual apparent modulus for the cortex and medulla areas of each reproductively older (O) cat ovary tested. **G**, Mean overall apparent modulus of the regions defined as cortex and medulla in both reproductively younger and older cats. **H**, Mean overall apparent modulus of reproductively younger cat ovaries versus apparent modulus of reproductively older cat ovaries. Student two-tailed, unpaired t-test for samples between age groups, student two-tailed paired t-test for values of cortex and medulla from same cat. *p < 0.05, and **p < 0.01. Error bars represent standard deviation. 17
Figure 2.4 Stereomicroscopic examination of ovarian tissue. A-B, Stereomicroscopy image of ovarian tissue without (**A**) and with (**B**) labeling with the perceived approximate areas of the cortex and medulla of the tissue based on tissue density and follicle location. Scale bar: 1 mm. 18
Figure 2.5 Characterization of viscoelastic heterogeneity in cat ovaries. A-B, Stress relaxation curves from areas of the cortex (C) and medulla (M) of reproductively younger (**A**, n=5) and older cats (**B**, n=5). **C-D**, Time constant for the first (**C**, τ_1) and second (**D**, τ_2) relaxation kinetics of the cortex and medulla of reproductively younger and older cats. **E-F**, Equivalent modulus (Eeq) versus time from areas of the cortex and medulla of reproductively younger (**E**) and older (**F**) cats. Dark red arrows indicate $Eeq, 0$. The dashed line represents the intrinsic elastic modulus (Ee) for the cortex and medulla. Values were obtained by fitting the 2nd order SLS viscoelastic model to the stress relaxation data in each physical area. Student two-tailed, unpaired t-test was used for comparing between the two different age groups, and student two-tailed paired t-test was used for comparing the values for cortex and medulla from same cat. *p < 0.05. Error bars represent standard deviation. 22
Figure 2.6 Characterization of the connection between the different moduli of cortex and medulla in cat ovarian tissue. A, Equivalent modulus at time zero ($E_{eq,0}$), apparent modulus (E_a), and intrinsic elastic modulus (E_e) of the ovarian cortex (C, light blue, circles), and medulla (M, dark blue, triangles) of reproductively younger cats (n=5). $E_{eq,0}$ and E_e were obtained by using the 2nd order SLS model to analyze the data from stress relaxation measurements. E_a was obtained using the Hertz model. B, $E_{eq,0}$, E_a and E_e of the ovarian cortex (C, light orange, circles), and medulla (M, brown, triangles) of reproductively older cats (n=5). Student two-tailed paired t-test. *p < 0.05, and **p < 0.01. Error bars represent standard deviation. 26
Figure 2.7 Distribution of hyaluronic acid (HA) in reproductively younger and older cat ovaries. A, Typical image of bisected cat ovary. The numbers 1, 2, and 3 indicate the edge, middle, and opposite edge locations of the ovary where images are further shown. Scale bar = 1 mm. **B**, Hematoxylin and Eosin (H&E) staining of regions of cat ovarian tissue, starting from the first edge (1) to the middle (2), to the other edge (3). Scale bar: 100 µm. **C**, Normalized intensity of HA staining fluorescence signal across the line profile of the ovaries of reproductively younger cats (n=3). **D**, Representative fluorescence images of the edge, middle, and edge of the reproductively younger cat ovarian tissue line profile showing HA (green) distribution. Nuclei are visualized using DAPI (blue). Scale bar: 100 µm. **E**, Normalized intensity of HA staining fluorescence signal across the line profile of the ovaries of reproductively older cats (n=3). **F**, Representative fluorescence images of

the edge, middle, and edge of the cat ovarian tissue line profile showing HA (green) distribution in reproductively older cats. Nuclei are visualized using DAPI (blue). Scale bar: 100 μm. Error bars represent standard deviation. 28
Figure 2.8 Distribution of collagen type I (COL-1) in reproductively younger and reproductively older cat ovaries. A, Normalized intensity of COL-1 staining fluorescence signal across the line profile of the ovaries of reproductively younger cats (n=3). **B**, Representative fluorescence images of the edge, middle, and edge of the reproductively younger cat ovarian tissue line profile showing COL-1 (red) distribution. Nuclei are visualized using DAPI (blue). **C**, Normalized intensity of COL-1 staining fluorescence signal across the line profile of the ovaries of reproductively older cats (n=3). **D**, Representative fluorescence images of the edge, middle, and edge of the cat ovarian tissue line profile showing COL-1 (red) distribution in reproductively older cats. Nuclei are visualized using DAPI (blue). Scale bars: 100 μm. 29
Figure 2.9 Hyaluronidase (HAse) treatment of older ovaries. **A**, Apparent modulus line-scan profiles of reproductively older ovaries treated with hyaluronidase (HAse, gray) to degrade HA in the tissue. Markers indicate mean apparent modulus values from one mapping site on the tissue, averaged from three separate 30 μm x 30 μm indentation maps taken at the 100 x 100 μm2 spatial window of the mapping site. Mapping sites were spaced 100 – 500 μm apart by manual stage adjustment. Position is normalized to the maximum width of the ovary, which varied because the size of the ovary varied between animals. **B**, Apparent modulus linescans based on normalized position across the ovary. Each ovary linescan is represented by a different symbol, showing all linescans from both untreated (orange) and HAse-treated (gray) ovaries. **C**, Mean apparent modulus of the regions defined as cortex and medulla in reproductively older cat ovaries both untreated (cortex: orange, medulla: brown) and treated with HAse (cortex: gray, medulla: dark gray). **D**, Normalized apparent modulus of the cortex and medulla of reproductively older cats with and without HAse treatment. Cortex and medulla values are normalized to the mean value of the cortex and medulla of reproductively older ovaries without HAse treatment. Error bars represent standard deviation. *$p < 0.05$, **$p < 0.01$ 31
Figure 3.1 Preparation and characterization of sand-PDMS film. **A**, A schematic illustration of the procedure for preparing the sand-PDMS film: The sand was first rinsed overnight with water, autoclaved, dried, and then sifted onto a thin and uncured PDMS layer over a fully cured PDMS film through a mesh strainer with 200 μm openings. The PDMS film embedded with sand was baked at 75 °C for 30 min to form the sand-PDMS film. The sand-PDMS film was cut into small pieces and each piece was stuck/attached onto the inner wall of a cryovial via its smooth face. **B**, Morphology and size distribution of sands before and after sifting them through the mesh strainer. Also shown is a high-magnification view of the sifted sands where the sharp morphology of the sands is more appreciable. The size distribution was quantified based on the area of sand particles on the films. Data collected by Jiang, B. **C**, Scanning electron microscopy (SEM) image, showing the presence and morphology of sands partially embedded in the PDMS film. Data collected by Ou, W. **D**, Energy dispersive X-ray spectroscopy (EDXS) quantification of the elemental composition of the sand-PDMS and pure PDMS films. The surface of the sand-

PDMS film contains an increased amount of silicon (Si) and oxygen (O) than the pure PDMS surface. Data collected by Ou, W. **E**, Quantification of Si counts for the sand-PDMS and pure PDMS films using EDXS. Data collected by Ou W. Scale bars: 200 μm **, $p < 0.01$ (n = 3 independent runs)..... 50
Figure 3.2 Sand enables ice seeding at high subzero temperature. **A**, Representative thermal histories in water containing no film (Control), pure PDMS film (PDMS), and sand-PDMS film (Sand-PDMS) during cooling. A sudden increase in temperature indicates ice seeding (which releases latent heat) in the sample. **B**, Quantitative data of the ice-seeding temperature in water under the aforementioned three conditions. **, $p < 0.01$ (n = 10 (for sand-PDMS film and pure PDMS film) or 20 (for Control), independent runs). **C**, Cryomicroscopy images at different times showing ice nucleation and growth around the sand particle during cooling the cell cryopreservation solution at subzero temperatures. Movie taken by Li, W., and analyzed by Stewart, S. Scale bar: 100 μm..... 52
Figure 3.3 High subzero ice seeding temperature is enabled by the sand-PDMS film. A, Representative thermal histories of follicle cryopreservation solution during slow-cooling of samples with no film (Control (Blank)) and Sand-PDMS film (Sand-PDMS film). The ice seeding temperature is indicated by a sudden increase in temperature due to the release of latent heat in the sample. **B**, Quantitative data of the ice-seeding temperature in follicle cryopreservation solution under the aforementioned two conditions (n=6 independent runs). * $p < 0.05$. 53
Figure 3.4 Ice nucleation/seeding with glass beads and plastic shards. (A) Scanning electron microscopy (SEM) image showing the presence and morphology of plastic shards and glass beads partially embedded in the PDMS film. The detailed morphology of the plastic shards and glass beads are more appreciable in the high-magnification views of the red dashed line-boxed areas. Scale bars: 200 μm. Images taken by Ou, W. (B) Representative thermal histories in water containing no film (Control), plastic shard-PDMS film, and glass bead-PDMS film during cooling. A sudden increase in temperature indicates ice seeding (which releases latent heat) in the sample. (C) Quantitative data of the ice-seeding temperature in water under the aforementioned three conditions. *, $p < 0.05$, **, $p < 0.01$ (n = 10 (for plastic shard-PDMS film and glass bead-PDMS film) or 20 (for control), independent runs)..... 55
Figure 3.5 Immediate viability of fresh and cryopreserved ovarian follicles. **A,** Immediate (after 2 h incubation in recovery medium at 37 °C) viability of fresh ovarian follicles, follicles cryopreserved without using the sand-film, and follicles cryopreserved using the sand-PDMS film assessed via live/dead (green/red) staining. The cryopreservation solution contains 10% DMSO, 10% FBS, and 0.1 sucrose in L15 medium. The blue dashed box shows a zoom-in image of a single follicle in the sample. Scale bar = 100 μm. **B**, Quantitative data of the immediate viability of ovarian follicles. Follicle was assessed by the viable follicle area (area staining only green, not green and red). Follicles with a viable area of more than 70% are considered viable, and immediate viability is calculated as the number of follicles with a viable area of more than 70% over the total number of follicles in each independent run (n=4). * $p < 0.05$. One-way ANOVA followed by a Tukey post hoc correction was used for statistical analysis. 58

Figure 3.6 Representative morphology of fresh and cryopreserved ovarian follicles during in vitro culture. Follicles cryopreserved with or without the sand-PDMS film were thawed and encapsulated in 0.25% alginate for 9 days of in vitro culture. Fresh follicles were encapsulated on the same day of isolation as a control. Images of the follicle were taken every other day of culture, starting on day 1. Scale bar = 50 μm. 59
Figure 3.7 Growth and long-term survival of fresh and cryopreserved ovarian follicles during in vitro culture. Growth curves of **A**, freshly isolated follicles, **B**, follicles cryopreserved without the sand-film, and **C**, follicles cryopreserved using the sand-film during 9 days of in vitro culture (n=4 independent runs). Each curve represents the growth curve of one individual follicle. Each independent run is represented by a different shade of the experimental group's color. The growth of each follicle is evaluated by the diameter of the follicle (D) over time normalized to the diameter of the follicle on day 1 (D1). A D/D1 ratio over 1 means the follicle is growing in diameter, while a D/D1 ratio less than one signifies that a follicle is shrinking and dying during the 9 days of culture. **D**, Survival of the ovarian follicles after 9 days of culture. The survival is calculated as the percentage of the number of follicles with a D/D1 greater than 1 on day 9 out of the total number of follicles in culture (n=4 independent runs). One-way ANOVA followed by a Tukey post hoc correction was used for statistical analysis. **E**, Mean growth curves of freshly isolated follicles and follicles cryopreserved using the sand-film during 9 days of in vitro culture (n=4 independent runs). * $p < 0.05$, ** $p < 0.01$, *** $p < 0.001$. Two-way ANOVA with Sidak's post-test and correction was used for statistical analysis. 62
Figure 3.8 The immediate and long-term viability of hiPSCs after cryopreservation under various conditions. **A**, Immediate (after 2 h incubation at 37 °C) viability of hiPSCs assessed by live/dead (green/red) staining after cryopreservation with different methods: conventional method (10% DMSO+10% serum with no ice seeding), sand-mediated ice seeding alone, no cryoprotectant and no ice seeding, 5% DMSO with no ice seeding, 2% DMSO with ice seeding, and 5% DMSO with ice seeding. Scale bar: 500 μm. **B**, Quantitative data of the hiPSC immediate viability and attachment efficiency (i.e., long-term viability) after the various cryopreservation conditions. For quantifying the attachment efficiency, the cryopreserved cells were thawed and cultured for 15 h, and the number of attached cells was counted by hemacytometer. The attachment efficiency is calculated as the percentage of cells counted after cryopreservation out of the number of cells initially cryopreserved. **, $p < 0.01$ (n = 3 independent runs) for the comparison of both immediate viability and attachment efficiency. Data collected and analyzed by Jiang, B., and Li, W. 64
Figure 3.9 Cryopreservation with sand-mediated ice seeding and 5% DMSO does not significantly affect the hiPSC pluripotency and cell cycle. A, Images of cryopreserved (Cryo) hiPSCs showing typical colony morphology and high expression of pluripotency protein markers OCT-4 and SSEA-4, similar to fresh (Control) hiPSCs with no cryopreservation. Scale bar: 100 μm. **B–C**, Representative peaks (**B**) and quantitative data (**C**, n = 3 independent runs) form flow cytometry analyses, showing the cryopreserved hiPSCs highly express pluripotency protein markers SSEA-4 and OCT-4 similar to the fresh control hiPSCs with no statistically

significant difference. The light blue peaks are isotype controls. **D–E**, Representative peaks (**D**) and quantitative data (**E**, n = 3 independent runs) from flow cytometry analyses, showing no statistically significant difference in the cell cycle distribution between the cryopreserved and fresh control hiPSCs. Data collected by Jiang, B..... 67
Figure 3.10 Cryopreservation with sand-mediated ice seeding and 5% DMSO does not significantly affect the differentiation capacity of the hiPSCs. **A**, The cryopreserved hiPSCs can efficiently differentiate into cells with typical neural cell morphology (neurites extending out of the cell body) and high expression of the neural specific marker TUJ-1. Cell nuclei are made visible by DAPI staining. **B**, The cryopreserved hiPSCs can efficiently differentiate into cells that highly express the cardiac specific markers cTnT. Cell nuclei are made visible by DAPI staining. **C**, The teratomas grown from the cryopreserved hiPSCs contain tissues from all the three germ layers including ectoderm (neural epithelium with hypernucelated neuroectodermal structures), mesoderm (the nidus of cartilage with surrounding condensed mesenchymal cells), and endoderm (gut epithelium with subnuclear vacuoles and tube-like structure). Scale bars: 100 μm. Data collected by Jiang, B. .. 69

Chapter 1 : Introduction

1.1 Ovarian follicles and human induced pluripotent stem cells (hiPSCs)

The ovarian follicle, made up of a germ cell (the oocyte) and layers of somatic support cells (granulosa and theca cells), is the functional unit of the ovary and plays a vital role in mammalian reproduction. Folliculogenesis, the growth and development of immature ovarian follicles in the ovary so that they can release mature, fertilizable oocytes, is a tightly regulated process by the hypothalamic-pituitary-ovarian axis [1]. Dysregulation of this tightly controlled process can cause impaired fertility, which affects roughly 13.1%. (or ~9.8 million) of reproductive-age people with ovaries in the USA [2], according to the national survey of family growth conducted by the Centers for Disease Control and Prevention (CDC). Infertility can arise from disorders like polycystic ovarian syndrome (PCOS) [3] and premature ovarian insufficiency (POI) [4], which both negatively impact function of the ovary, an integral reproductive organ. Chemotherapy and radiation treatments for cancer, while increasing cancer survival rates in both pre- and post-pubertal patients, can be especially damaging to the ovaries [5-7]. Alkylating agents in the treatment of childhood cancer have resulted in acute ovarian insufficiency, premature menopause, and poor reproductive outcomes [8, 9]. An increased risk of ovarian damage and POI is also associated with nononcologic conditions, like various hematological disorders, autoimmune disorders, genetic disorders, endometriosis, and their treatments [10-12]. Hematopoietic stem cell transplantation, used in treatment of various non-cancerous conditions and requiring

large doses of chemotherapy and radiation to destroy existing bone marrow, has been found to be associated with a 65-85% risk of POI [13]. Aging also greatly impacts ovarian function and childbearing potential. The mammalian ovary contains a finite number of ovarian follicles formed during embryonic development; humans with ovaries are born with ~1 million follicles that are non-renewable and degenerate over time [14]. Fertility in people with ovaries begins to significantly decrease after 32 years of age, with this deterioration accelerating by age 37, and ultimately complete loss at ~50 years old [15]. Beyond the clinic, fertility preservation strategies are greatly needed for animal genetic conservation, crucial for maintaining biodiversity and agricultural applications [16, 17].

In addition to impaired fertility, POI can cause additional endocrine dysfunction that affects patients' daily lives [18]. This can result in estrogen deficiency, which in turn can lead to lower bone mineral density (osteopenia and osteoporosis) [19]. POI is also associated with an increased risk of cardiovascular disease and neurological disorders due to the endocrine effects on metabolism [20]. Thus, there is a demonstrated need for novel fertility restoration and preservation strategies, like ovarian tissue engineering, to address these concerns [5, 21].

Human induced pluripotent stem cells (hiPSCs) have tremendous potential for tissue engineering and cell-based medicine, as they are able to differentiate into ectodermal, mesodermal, endodermal, and germ cell lineages [22, 23]. The use of hiPSCs allows for personalized medicine, as the cells can be reprogrammed from the patient's own cells [24], and avoids the ethical concerns associated with the use of human embryonic stem cells (hESCs) [25]. In recent years, hiPSCs and hESCs have

been differentiated into cells like those that make up the ovary to treat infertility and endocrine dysfunction [26-29]. The exploration of hiPSCs for ovarian tissue engineering is an exciting and promising strategy for fertility preservation/restoration and to treat endocrine dysfunction resulting from POI. Beyond this application, hiPSCs show great promise for research and therapy for many diseases and disorders beyond those that center around the ovary, like neural and cardiovascular diseases [30, 31].

1.2 Engineering the microenvironment of the ovary

There are a number of challenges associated with engineering ovarian tissue, specifically ovarian follicles, for fertility preservation/restoration applications. Understanding and engineering the cell/tissue microenvironment and how the cells/tissues interact with the components of the system is vital for the success of tissue engineered systems [32].

1.2.1 Micromechanical environment of the ovary

The ovarian stroma, the components of the ovary that are not ovarian follicles, contains connective tissue, nerves, blood and lymphatic vessels, immune cells, ovarian stromal cells, and extracellular matrix (ECM) that play key roles in follicle development and ovarian function [5, 33]. The ECM, composed of fibril- and network forming proteins and glycosaminoglycans, not only provides a three-dimensional (3D) network to support the tissue architecture, but also helps to regulate follicle development through cell-ECM and cell-cell interactions. The ovary is comprised of two distinct regions—the outer cortex and the inner medulla—which have different stromal cell organization, ECM distribution, and structure [33-35]. Stromal cells,

spindle-shaped similar to fibroblasts, are organized parallel to the ovary surface and have a rounded structure in the ovarian cortex [5]. The collagen-rich cortex also has a higher ECM density than the medulla [33]. Conversely, the medulla has an ECM density lower than that of the cortex. During development, immature follicles in the cortex are activated and continue to grow as they migrate toward the medulla. The maturing follicle then completes its development along the perimedullar zone before ovulation at the ovarian surface. The difference in the physical environment of these two regions may direct follicle growth and could play an important role in ovarian tissue engineering [35].

Although the field has noted the physical differences in the cortex and medulla, few studies have characterized the mechanical properties of ovarian tissue [36-38], especially how they may differ between the cortex and medulla. Few studies thus far have explored the viscoelastic (time-dependent) behavior of ovarian tissue and none has investigated the viscoelastic heterogeneity in the ovary [39], even though biological tissue is a viscoelastic material [40, 41]. Mounting evidence also suggests that viscoelastic properties can affect cell behavior in ways that are not predicted when considering only elastic behavior [41]. Atomic force microscopy (AFM) indentation can be used to measure mechanical properties of biological tissues with high spatial resolution, allowing differentiation of mechanical properties between the cortex and medulla as identified using the microscope integrated in the system. With the proper probe selection, viscoelastic (time-dependent) properties can also be characterized using AFM indentation technique [40].

The mechanical behavior of soft tissues is mainly governed by the content, distribution, and organization of ECM components, like collagen and elastin fibers [42]. For example, collagens contribute to the tensile strength, while glycosaminoglycans, like hyaluronic acid (HA), work to restrain water, conferring elasticity to tissues and maintain osmotic equilibrium [43]. Collagen, found abundantly in the ovarian stroma, forms a viscoelastic matrix and exhibits stress relaxation as evidenced by in vitro testing of collagen gels, showing the resistance of the gel to a deformation relaxing over time [44, 45]. Although the ECM in the ovary has been characterized for several species [46-48], there is no comprehensive study that has explored the relationship between ECM distribution in the cortex and medulla and the mechanical properties of the cortex and medulla.

1.3 Cryopreservation of ovarian follicles and hiPSCs

Cryopreservation involves cooling cells and tissues to low temperatures to slow down metabolic processes and preserve them in a suspended state of animation for long-term storage. To protect the cells/tissues from damage during the cryopreservation process, cryoprotectants (CPA) are added to the cryopreservation solution. These can be penetrating CPAs, such dimethyl sulfoxide (DMSO) and propylene glycol (PG), which can be potentially toxic in high concentrations, or non-penetrating CPAs, such as trehalose and sucrose, which are usually nontoxic to cells [49].

1.3.1 Cryopreservation of isolated preantral ovarian follicles as an alternative fertility preservation strategy

Post-pubertal patients facing infertility have several options for preserving their fertility through cryopreservation. Mature oocyte and embryo cryopreservation are currently the most widely explored techniques [50]. For this method, at least one cycle of controlled hormonal ovarian stimulation is needed to collect mature oocytes either for immediate banking or *in vitro* fertilization (IVF) to produce embryos [51]. This option is not suitable for patients with aggressive diseases who cannot delay treatment to undergo hormonal stimulation. Data from a meta-analysis of seven studies investigating survival in patients with operable primary breast cancer suggests that overall survival decreased by 15% for every 4-week delay in initiation of chemotherapy [52]. Moreover, the hormonal stimulation may be contraindicated in patients with hormone-responsive diseases [53]. If a patient is a candidate for hormonal stimulation, it is usually preferred to cryopreserve embryos rather than oocytes for fertility preservation, as oocytes are more difficult to cryopreserve [54]. However, embryo cryopreservation does not allow for reproductive autonomy for the patient—they must rely on a sperm source, from either a partner or donor, in order to preserve their future fertility [10]. Additionally, patients may have legal, moral, ethical, and religious concerns regarding the freezing of embryos. [55]. Patients who have not yet undergone puberty do not have oocyte or embryo cryopreservation as options for preserving their fertility before treatment in cases of malignant disease. Conventional embryo technologies also currently play a negligible role in the reproductive management of

many animal species that are either difficult to recover mature oocytes from or resist (or are extremely sensitive to) hormone stimulation [17, 56-58].

Ovarian tissue cryopreservation (OTC) is the only viable option for pre-pubertal patients and post-pubertal patients who cannot undergo controlled ovarian stimulation [59]. OTC has also been indicated for those who wish to delay childbearing or postpone menopause [60]. For OTC, part or all of the ovarian tissue is surgically removed and banked at low temperature for future orthotopic or heterotopic transplantation. Although promising, this approach carries the risk of re-introducing malignant cells (e.g., leukemic cells, circulating tumor cells in the blood of ovary, primary ovarian cancer cells) back into patients and causing disease recurrence [61-63]. Although preantral follicles can be isolated after cryopreservation of slices of ovarian cortex, cryopreservation of freshly isolated preantral follicles offer distinct advantages over tissue freezing [64]. Cryopreservation of pieces of ovarian cortex can present technical problems due to the heterogenous cell population. Because of the small size of preantral follicles, CPA can permeate the follicle much more readily than through a larger tissue volume. Additionally, high follicular loss has been observed after ovarian tissue transplantation due to ischemia-reperfusion [65, 66]. Follicles are difficult to recover after ovarian tissue cryopreservation due to the difficulty in quantitatively and quantitatively evaluating the follicle population in tissue fragments, as follicles are unevenly distributed in the cortex [67, 68].

Encouraging results have already been obtained from investigations into cryopreservation of isolated follicles in several animal species [69-71]. Isolated secondary murine follicles cryopreserved in alginate hydrogels had ~70% survival after

cryopreservation and in vitro growth similar to freshly isolated controls during 12 days of culture [70]. However, these protocols rely on expensive or time-consuming materials/methods for seeding ice in the samples at high subzero temperature, an integral cryopreservation step to ensure good cryopreservation outcomes for ovarian tissue [72].

1.3.2 Cryopreservation of hiPSCs

The ready availability of hiPSCs enabled by long-term cryopreservation or low-temperature banking is necessary for wide distribution and eventual success of the emerging stem-cell based medicine [73-76]. These hiPSCs need to maintain high viability and pluripotency after the cryopreservation process. Conventional cryopreservation of hiPSCs uses slow-freezing with the addition of 10% DMSO as the penetrating CPA and 10% fetal bovine serum (FBS) or serum replacement. Although DMSO is an effective CPA, the organic solvent is highly toxic to cells and tissues at body temperature [77-80]. The hiPSCs cryopreserved with DMSO require careful washing to remove the CPA before use, which can result in loss of up to 10% of the cells with each washing step [81]. Additionally, DMSO has been linked to causing unwanted differentiation of hiPSCs [82] and changes in the epigenetic landscape of cardiac cells [83]. The use of FBS in the cryopreservation solution poses a risk for the clinical translatability of hiPSCs, as it carries the risk of spontaneous differentiation and introduction of xenogeneic pathogens into the sample [84, 85]. These risks highlight the need for better hiPSC cryopreservation technologies.

1.4 Dissertation overview and outline

The overall goal of this dissertation is to develop multiscale technologies for engineering and cryopreserving ovarian follicles and hiPSCs to further advance their utility for cell-based therapy. **Chapter 1** (this chapter) gives an introduction and broad background of the challenges this dissertation research is aiming to address and offers a summary/outline of the research.

Chapter 2 characterizes the micromechanical properties of ovarian tissue from reproductively younger and older domestic cats. AFM indentation is used to determine values for the elastic and viscoelastic properties of the cortical and medullar regions, which shows not only elastic but also viscoelastic heterogeneities in the ovary. Mathematical modeling using a second-order standard linear solid viscoelastic model reveals that the apparent modulus reported in literature is not the true elastic modulus and has a contribution from viscoelastic behavior. The distribution of two important ECM molecules, collagen type I and HA, is explored and linked to the mechanical properties characterized by AFM indentation.

Chapter 3 details a novel cryopreservation method, using sand as a biocompatible ice nucleator to seed ice in the extracellular space at high subzero temperatures to enhance cryopreservation outcomes of ovarian follicles and hiPSCs. Sand is immobilized on a polydimethylsiloxane (PDMS) film and adhered to the wall of a cryovial to initiate ice formation in the sample in a controlled instead of spontaneous fashion. The ice-seeding ability of the sand is tested and characterized. Preantral ovarian follicles and hiPSCs are frozen in the sand-PDMS film-laden cryovial using a slow-freezing procedure. The cell/microtissue quality is assessed after

cryopreservation, storage in liquid nitrogen (LN2), and thawing of the samples. The immediate viability and growth potential of the ovarian follicles is investigated after thawing. The viability, attachment, cell cycle, pluripotency, and differentiation capacity are assessed for the cryopreserved hiPSCs.

Chapter 4 provides conclusions for the research in this dissertation and **Chapter 5** discusses potential avenues for future studies and applications of the work.

Chapter 2 : Micromechanical characterizations and viscoelastic modeling reveal both elastic and viscoelastic heterogeneities in ovarian tissue and the significant contribution to the apparent elastic modulus determined by AFM indentation*

2.1 Introduction

The ovarian follicle is the fundamental functional unit of the ovary, made up of a female germ cell (oocyte) and surrounding layers of somatic support cells. The activation and growth of the ovarian follicles are tightly regulated so that usually one follicle releases a mature, fertilizable egg per cycle for humans. Ovarian disorders like PCOS, exposure to aggressive disease treatment (e.g., chemotherapy), and environmental/occupational biohazard exposures can all result in infertility due to dysregulation of this precisely controlled process [10, 86, 87]. Aging also impacts fertility as the ovarian follicle reserve is nonrenewable [88], and many patients wish to delay childbearing beyond peak fertility age. Many fertility restoration strategies aim to replicate the *in vivo* conditions for activation and growth of immature ovarian follicles *in vitro,* to meet the increasing demand for fertility preservation [5, 21, 86]. Although the effects of many growth factors, hormones, and chemical medium additives on *in vitro* follicle culture have been studied and demonstrated [89, 90], the effect of the follicle's surrounding mechanical environment on folliculogenesis has

* Reprinted (adapted) with permission from: Stewart, S., Ou, W., Aranda-Espinoza, H., Rahaman, S., He, X. Micromechanical characterizations and viscoelastic modeling reveal elastic and viscoelastic heterogeneities in ovarian tissue and the significant viscoelastic contribution to the apparent elastic modulus determined by AFM indentation. Acta Biomaterialia 168 (2023) 286-297. Copyright 2023 Elsevier.

attracted tremendous attention recently [91-94], with increasing evidence showing that mechanical regulation plays a vital role in follicle development [35, 95].

The ovary is comprised of two distinct physical regions—the outer cortex and inner medulla—which have different stromal cell organization and ECM distribution [33]. These differences in structure between the two regions lead to differences in mechanical properties: the cortex is more rigid than the medulla. The mechanical properties in these two zones play a crucial role in mechanotransduction for the follicle during its growth and development, and accounting for mechanical heterogeneity in follicle culture has previously been shown to improve antrum formation in outbred deer mice [34]. The actual mechanical properties of the ovary in these two distinct regions, however, have not been well characterized. Most reported values of the elastic modulus of ovarian tissue have focused on bulk characterization methods at the ovarian surface or focus solely on regions in the ovarian cortex [47]. Recent mechanical characterization of the mouse ovarian interior [96] and the cortex and the medulla regions of bovine ovaries [97] shows that the modulus varies depending on the area of the tissue, further motivating study of how mechanical properties may differ in the cortex and medulla. Moreover, the ovary is a dynamic, mechanically responsive structure, with follicles interacting with their surrounding matrix over time [98, 99]. The magnitude of these forces depends not only on the elastic behavior of the surrounding ovarian tissue, but also the viscoelastic response, which has not been well studied.

In this work, we use atomic force microscopy (AFM) indentation to spatially characterize the elastic and viscoelastic properties in ovarian tissue of domestic cats for

revealing the direct mechanical microenvironment that follicles experience in the cortex and medulla. We tested tissue from reproductively younger and older (i.e., pre and post-puberty) samples to investigate how aging impacts the mechanical properties of ovarian tissue. The apparent elastic modulus was measured at points across the bisected ovary to determine the modulus range for cat ovarian tissue. Furthermore, we investigated viscoelastic behavior differences in the cortex and medulla of ovarian tissue for the first time and fit our experimental data with viscoelastic models to characterize the stress-relaxation behavior of the two different physical regions in the ovary. Combining this mechanical data with spatial distribution of key extracellular matrix (ECM) components in the ovary, hyaluronic acid (HA) and collagen type I (COL-1), we thoroughly characterize the mechanical microenvironment experienced by follicles during different reproductive ages. These insights into the ovarian physical environment can be used in rational design of biomaterials for building biomimetic culture systems to enhance assisted reproduction technologies.

2.2 Results and Discussion

In this study, we characterized the micromechanical (both elastic and viscoelastic) behavior of cat ovarian tissue. To spatially resolve differences between the cortical and medullar regions of the ovary, AFM probe indentation was used for analyzing the mechanical environment experienced by the ovarian follicles. The ovary was bisected to reveal the ovarian interior and embedded in agarose gel to stabilize it during the measurement. Measurements were performed across a line in the middle of the ovary, from one edge through to the other edge (**Fig. 2.1A**), to study the elastic and viscoelastic heterogeneity of the tissue. The apparent modulus was extracted from the

resultant force-indentation curves (**Fig. 2.1B**) to create a modulus profile across each ovary tested. A second order SLS model (**Fig. 2.1C**) was fit to stress relaxation measurements of the ovarian tissue to characterize the viscoelastic behavior of the cortex and medulla of each ovary. Finally, the spatial distributions of ECM molecules, HA and COL-1, were analyzed across the same middle region of the ovary (**Fig. 2.1D**) to relate the mechanical properties to the tissue composition.

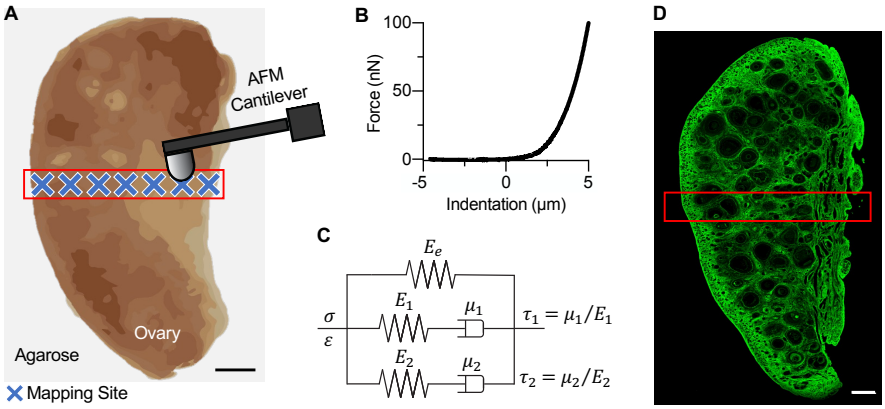

Figure 2.1 A schematic illustration of the characterization of mechanical properties of cat ovarian tissue. A, Schematic of mechanical testing of the cat ovary using atomic force microscopy (AFM) indentation. The ovary was embedded in an agarose gel and bisected to reveal the inner ovarian tissue. A line scan across the ovary was analyzed, mapping the mechanical properties at approximately 200 μm intervals. At each mapping site, force-indentation maps were taken to determine the apparent elastic modulus of the tissue using the Hertz model. Stress relaxation measurements were also performed by AFM indentation at each mapping site. Scale bar = 1 mm. **B**, Representative force-indentation curve that was used for Hertz model fitting to extract the apparent modulus. **C**, 2nd order standard linear solid (SLS) viscoelastic model used for fitting the stress relaxation data. The model is made up of elastic solid elements represented by springs and viscous Newtonian fluid elements represented by dashpots. The model consists of a purely elastic spring arm with modulus E_e in parallel with two viscoelastic Maxwell arms. The first Maxwell arm consists of a solid spring with modulus E_1 and fluid dashpot with viscosity μ_1. The second Maxwell arm has a solid spring with modulus E_2 and fluid dashpot with viscosity μ_2. The stress and strain are indicated as σ and ε, respectively. Each of the two Maxwell arms represents a different viscoelastic kinetics with τ_1 and τ_2 as the relaxation time constants, where $\tau_1 = \mu_1/E_1$ and $\tau_2 = \mu_2/E_2$. D, Extracellular matrix (ECM) characterization of the cat ovary. The representative image shows a fluorescence image of the cat ovary stained for hyaluronic acid (HA). The intensity of HA was quantified across the middle of the ovary, similar to the profile of AFM measurements in panel **A**, represented by the red box. Scale bar: 1 mm.

2.2.1 Heterogeneity of elastic modulus

We measured the apparent modulus (E_a) of 14 ovaries collected from domestic cats (n=14). This modulus is referred to as "apparent" because this value could be impacted by the indentation rate of the probe and not reflect the true intrinsic material property [100]. The ovary shows a wide range of modulus values across the tissue (0.2 kPa – 17.9 kPa, **Fig. 2.2A**) with a mean apparent modulus across all ovaries of 2.7 ± 0.3 kPa. The distribution of values shows that most measured sites on the ovary had a modulus under 3 kPa (**Fig. 2.2B**).

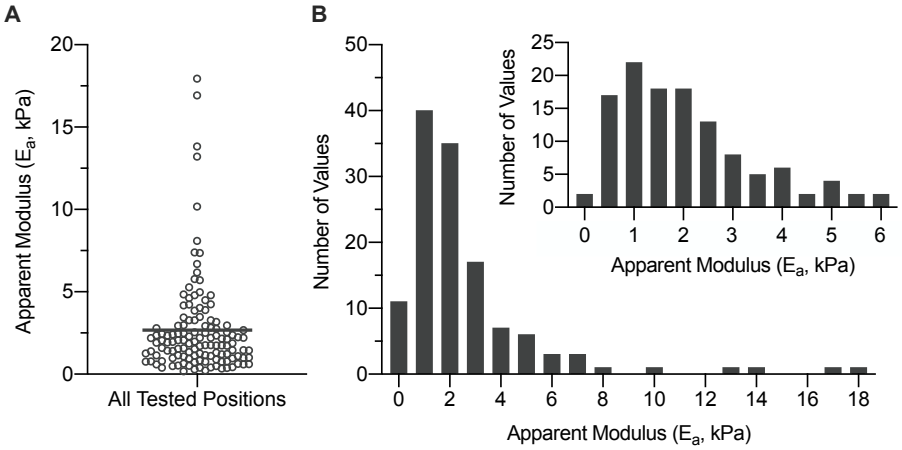

Figure 2.2 Characterization of the apparent elastic modulus of cat ovarian tissue. **A**, Apparent modulus (E_a) of all tested mapping sites (average of all individual force-indentation measurements at mapping site) across all ovaries tested (n=14). **B**, Histogram representing the overall distribution of apparent moduli (E_a, kPa) across all probed ovaries (n>100). The x-axis values correspond to upper limit of the bin (i.e., modulus value). Each value within the histogram represents one analyzed mapping site. Inset shows same data with finer bins, focusing on values from 0-6 kPa.

Interestingly, our range of measured values is similar to those reported for modulus of dissected mouse ovarian tissue [96] and whole-ovary measurements of reproductively young (pre-puberty) mice [47]. To our knowledge, this work is the first report of AFM characterization of ovarian tissue modulus for the domestic cat. The wide range and

distribution of the apparent modulus data underscores the importance of exploring the micromechanical environment rather than relying on bulk modulus characterization.

The apparent modulus of the cat ovarian tissue was further analyzed based on reproductive age. Ovaries from 7 cats below 6 months of age were characterized as reproductively younger (pre-puberty), and ovaries from 7 cats above 6 months of age were characterized as reproductively older (post-puberty) [101]. Looking at the individual line modulus scans of each ovary, for both reproductively younger and older cats, there is heterogeneity of the apparent modulus across the tissue (**Fig. A.1**). The modulus is highest at the two edges and decreases into the middle, with few exceptions. This is more clearly seen when plotting all the modulus profiles of all 7 cats together for reproductively younger (blue) and reproductively older (orange) ovaries in **Figure 2.3A and 2.3B**, respectively. For both age groups, the ovarian tissue shows its highest modulus value in both outer edges of the tissue, with a dip in the middle region. Noticeably higher modulus values can be seen in the two edges of reproductively older ovaries (~5-7 kPa) than reproductively younger ones (~2-4 kPa), with similar values in the middle interior for both reproductive age groups (~1.5 kPa). Again, for both age groups, the higher modulus values are seen in the outer edges of the tissue, with the lower modulus values measured in the middle of the ovary.

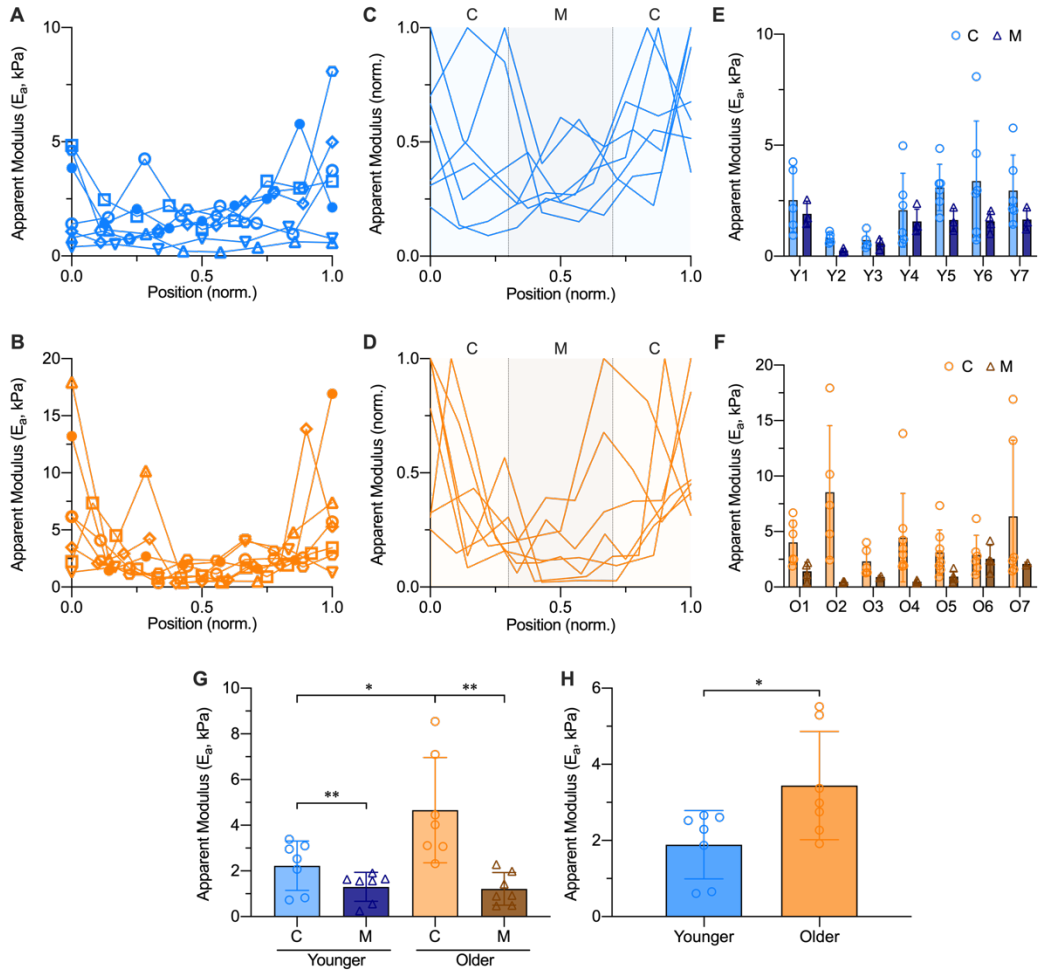

Figure 2.3 Analysis of apparent modulus (E_a, kPa) heterogeneity in cat ovaries. A, Apparent modulus line-scans of reproductively younger ovaries (<6 months, n=7). Each ovary linescan is represented by a different symbol. **B,** Apparent modulus line-scans of reproductively older ovaries (>6 months, n=7). Each ovary linescan is represented by a different symbol. **C,** Normalized apparent modulus line scan profiles of all the seven reproductively younger cat ovaries. The cortex (C, light blue shading) is noted as 0.0 – 0.3, and 0.7 – 1.0 of the tissue based on normalized position. The medulla (M, darker shading) is noted as 0.3 – 0.7 of the tissue based on normalized position. **D,** Normalized apparent modulus line scan profiles of all the seven reproductively older cat ovaries. The cortex (C, light orange shading) is noted as 0.0 – 0.3, and 0.7 – 1.0 of the tissue based on normalized position. The medulla (M, darker shading) is noted as 0.3 – 0.7 of the tissue based on normalized position. **E**, Individual apparent modulus for the cortex (C) and medulla (M) areas of each reproductively younger (Y) cat ovary tested. **F**, Individual apparent modulus for the cortex and medulla areas of each reproductively older (O) cat ovary tested. **G**, Mean overall apparent modulus of the regions defined as cortex and medulla in both reproductively younger and older cats. **H**, Mean overall apparent modulus of reproductively younger cat ovaries versus apparent modulus of reproductively older cat ovaries. Student two-tailed, unpaired t-test for samples between age groups, student two-tailed paired t-test for values of cortex and medulla from same cat. *$p < 0.05$, and **$p < 0.01$. Error bars represent standard deviation.

The modulus heterogeneity in each and all of the seven ovaries can be better appreciated by normalizing the linescan of modulus for each ovary to its respective maximum modulus measured in each linescan (**Fig. 2.3C-D**). Based on aforementioned analysis and stereoscopic examination of tissue architecture of the tested ovaries (**Fig. 2.4**), we designated 0.0-0.3 and 0.7-1.0 (based on normalized position) of the ovary as cortex (C, **Fig. 2.3A-D**) and 0.3-0.7 (based on normalized position) of the ovary as medulla (M, **Fig. 2.3A-D**), to analyze the mechanical properties in those physical regions. The data of apparent modulus from the linescans show that there is a larger difference between the cortex and medulla for reproductively older cats than that for reproductively younger cats. **Figure 2.3E-F** show the moduli for the cortex and medulla of each individual ovary tested from reproductively younger and reproductively older cats, respectively. The cortex of reproductively older cats has a modulus 1.5-18 times higher than the medulla. The cortical modulus of reproductively younger cats, meanwhile, is only 1.3-3.2 times higher than the medullar modulus. Consistent with the long-standing hypothesis that the cortex and medulla have distinct mechanical properties [102], the cortex has a significantly higher modulus than the

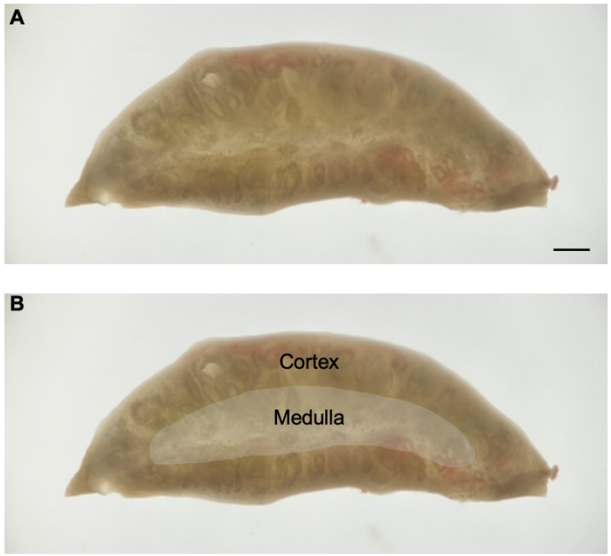

Figure 2.4 Stereomicroscopic examination of ovarian tissue. A-B, Stereomicroscopy image of ovarian tissue without (**A**) and with (**B**) labeling with the perceived approximate areas of the cortex and medulla of the tissue based on tissue density and follicle location. Scale bar: 1 mm.

medulla: ~2 times and >4 times on average for the reproductively younger and older cats, respectively (**Fig. 2.3G**). This difference is statistically significant for ovaries from both reproductively younger and older cats, although the difference is not as stark for the reproductively younger cats. The apparent modulus of the cortex in the reproductively older ovarian tissue is approximately twice as high as the apparent modulus of the cortex in reproductively younger ovarian tissue (4.7 ± 0.9 kPa vs. 2.2 ± 0.4kPa). Interestingly, there is no difference between the apparent modulus of the medulla based on reproductive age (1.2 ± 0.3 kPa for older, 1.3 ± 0.2 kPa for younger). This could be due to the presence of larger follicles in the cortex of the reproductively older ovaries than those in the cortex of reproductively younger ovaries. These larger follicles, due to the reproductive maturity of the older cats, could offer more reinforcement to the surrounding stromal tissue and cause the increased modulus [96]. Within the 30 x 30 μm^2 mapping areas, local modulus variation arises in mapping points located in the cortex but not in the medulla, similar to the trend observed in mouse ovarian tissue [96]. In other words, in areas with higher apparent modulus, there was greater local variation in apparent modulus.

Analyzing the mean apparent modulus value of the ovary as a whole, ovaries from reproductively older cats show a statistically significant higher apparent modulus than ovaries from reproductively younger cats (3.4 ± 0.5 kPa versus 1.9 ± 0.3 kPa, **Fig. 2.3H**), suggesting that the ovarian mechanical environment is impacted by aging. Indeed, increased collagen/stromal deposition has been linked to aging in ovaries from humans and animal models [39, 47, 103-105]. This increased modulus and collagen deposition, indicative of tissue fibrosis, has been linked to loss of ovarian function and

fertility diseases like polycystic ovarian syndrome (PCOS) [106]. In this study, however, the reproductively older cat group is made up of domestic cats that have recently reached sexual maturity and are still fertile, suggesting that the increase in modulus gradient between the cortex and medulla of the reproductively older ovaries and overall modulus may play an important role in fertility. During folliculogenesis, activated follicles migrate from the ECM-dense outer cortex to the inner, softer perimedulliary zone where they grow in size and mature the oocyte until ovulation at the ovarian surface. These findings further support the hypothesis that mechanical heterogeneity between the cortex and medulla in the ovary plays an integral role in fertility [34].

2.2.2 Heterogeneity of viscoelastic properties

Although most studies on the mechanical properties have been focused on the elastic behavior of ovarian tissue, biological tissue is a viscoelastic material. Growing evidence suggests that viscoelastic properties can affect cell behavior in ways that are not predicted when considering only elastic behavior [41]. We used AFM indentation to characterize the viscoelastic behavior of ovarian tissue in the cortex and medulla of ovarian tissues from the two reproductive age groups (younger and older). We observe viscoelastic stress relaxation of the ovarian tissue in the cortex and medulla of all cats (n=5, for each biological age group). The viscoelastic behavior is modeled by a second-order standard linear solid (SLS) model, consisting of one purely elastic element (spring) and two Maxwell viscoelastic arms in parallel (**Fig. 2.1C** and **Eq. 2.1-3**). Each of the two Maxwell viscoelastic arms is made of one purely elastic element and one purely viscous element in series. This model can be used to predict the measured

viscoelastic response well ($R^2 > 0.98$) as seen in **Figure 2.5A-B**. The 1st order SLS model (**Fig. A1.2**) was initially used to model stress relaxation, but the fitting was poor, so the 2nd order model was used for all further analyses. The stress relaxation behavior of ovarian tissue in both the cortex and medulla of reproductively younger and older cats is given in **Figure 2.5A and B**, respectively. For all cases, the tissue relaxes quickly in the first 5 s in response to the applied strain, then slowly relaxes for the duration of the measurement. It is worth noting that the stress relaxation data given in **Figure 2.5A-B** show that the first derivative (or slope) of stress versus time curve at time 0 (i.e., $\left.\frac{d\sigma}{dt}\right|_0$) is nonzero. Additionally, the duration of the relaxation measurement was stopped at 60 s, as this is sufficient to capture the longer relaxation kinetics evidenced by the stress relaxing towards a plateau/asymptote by the end of the measurement.

By fitting the viscoelastic model to the experimental data, we can describe this relaxation behavior with two relaxation time constants τ_1 and τ_2 (**Fig. 2.5C-D**). These two time constants for the relaxation behavior may correspond with different components of the mechanical environment that dominate separate sections of the tissue viscoelastic response. The range of the two time constants reported here is relevant to those reported for cell behaviors that may be important to consider during follicle growth and development. The τ_1 values observed here (~1 s) fall on the timescale over which cells respond to oscillations in force (~1 s) [107]. The τ_2 values reported here (~20-40 s) are similar to the timescales over which cells exert traction force (minutes)[108] and undertake spreading (minutes to hours) [109, 110]. There is no significant difference in τ_1 between the two ovarian tissue regions or two age

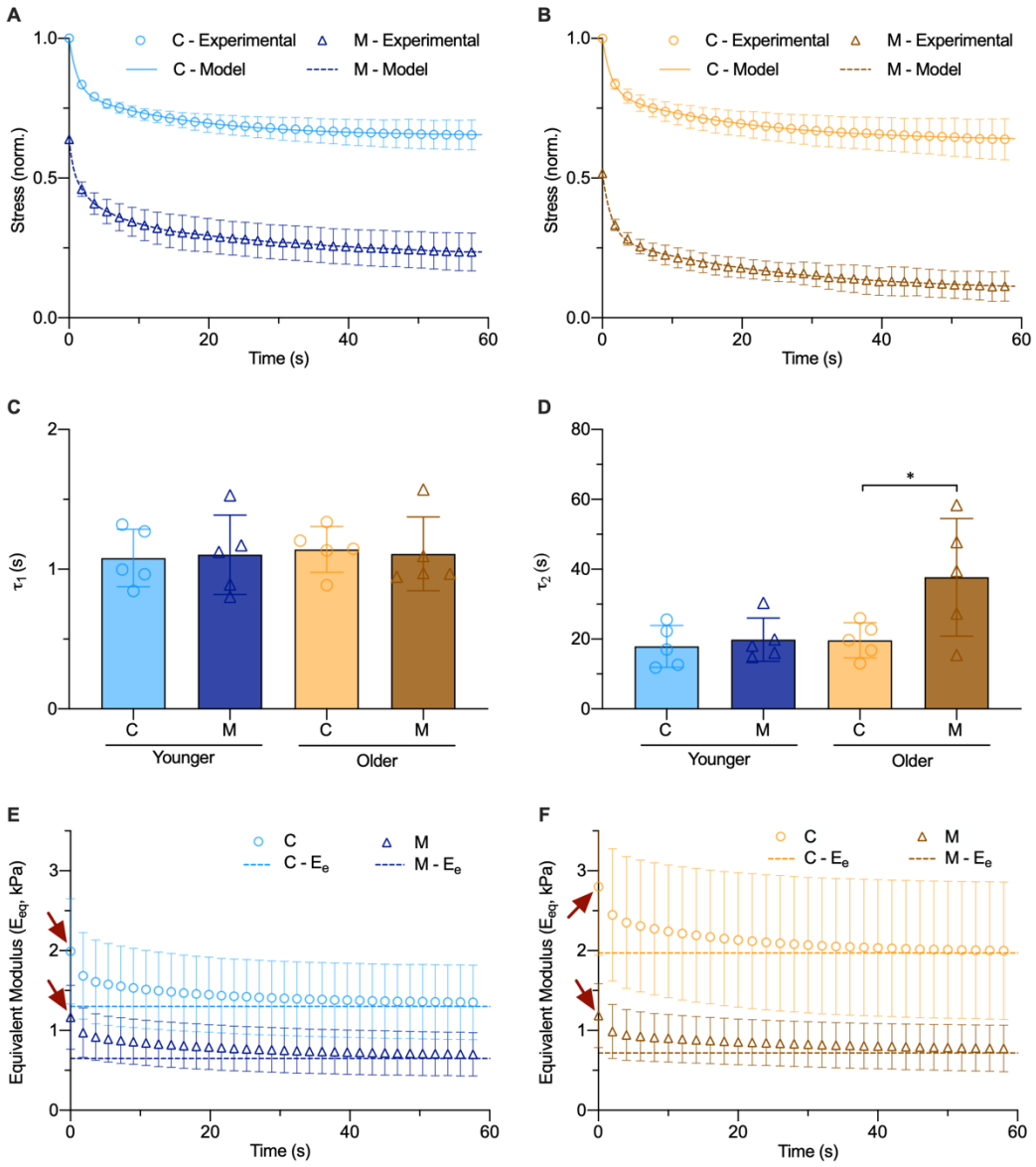

Figure 2.5 Characterization of viscoelastic heterogeneity in cat ovaries. A-B, Stress relaxation curves from areas of the cortex (C) and medulla (M) of reproductively younger (**A**, n=5) and older cats (**B**, n=5). **C-D**, Time constant for the first (**C**, τ_1) and second (**D**, τ_2) relaxation kinetics of the cortex and medulla of reproductively younger and older cats. **E-F**, Equivalent modulus (E_{eq}) versus time from areas of the cortex and medulla of reproductively younger (**E**) and older (**F**) cats. Dark red arrows indicate $E_{eq,0}$. The dashed line represents the intrinsic elastic modulus (E_e) for the cortex and medulla. Values were obtained by fitting the 2nd order SLS viscoelastic model to the stress relaxation data in each physical area. Student two-tailed, unpaired t-test was used for comparing between the two different age groups, and student two-tailed paired t-test was used for comparing the values for cortex and medulla from same cat. *$p < 0.05$. Error bars represent standard deviation.

groups, with all time constants being ~1 s on average and less than ~1.5 s nearly always. There is also no significant difference between τ_2 in the cortex and medulla for reproductively younger cat ovarian tissue. However, there is a statistically significant difference in the second relaxation time constant between the cortex and medulla of reproductively older cat ovarian tissue (19.6 ± 2.2 s versus 37.7 ± 7.5s). The τ_2 relaxation time constant in the cortex and medulla of younger ovaries and in the cortex of older ovaries are all very similar (~20 s), however, the τ_2 relaxation time constant in the medulla of older ovaries spans a much wider range. There are no noticeable differences in viscoelastic behavior between the cortex and medulla of reproductively younger cat ovaries at any timescale, but reproductively older cat ovaries show distinct viscoelastic phenotypes in the cortex and medulla at longer timescales. This difference may have implications for how follicles exert forces on and grow in the surrounding matrix in the two regions, given that the τ_2 relaxation times are on the timescale like that reported for traction forces and cell spreading. Because the reproductively older ovaries are tested from domestic cats who have reached sexual maturity, this difference in viscoelastic behavior in physical regions of the ovary that is revealed with age may play a role in follicle development and could be a key consideration for ovarian follicle culture systems. Recent mechanical mapping of the mouse ovary using Brillouin microscopy suggests that the cortex may be more elastic than the interior (i.e., medulla), which appears more viscous, based on ratios of the storage/elastic and loss/viscous moduli in these regions inferred by the measurement method [94]. Also, although no data were reported for the ovarian medulla, a recent study on AFM-based probing of the viscoelastic behavior of human ovaries shows significant impact of age on the

cortical tissue [39]. Our findings in the domestic cat, together with these observations, suggest that viscoelastic heterogeneity in the ovary and how the viscoelastic behavior may change with reproductive age are important considerations for follicle growth and development.

2.2.3 Significant contribution of viscoelasticity to apparent elastic modulus determined by AFM indentation

We also used the second order SLS model to evaluate the intrinsic elastic modulus (E_e) and the equivalent modulus (E_{eq}) of the cortex and medulla of reproductively younger and older cats, and the data are given in **Figure 2.5E-F**. For both regions in both age groups, the equivalent modulus shows a trend of exponential decay over time, reaching an asymptote at the tissue's intrinsic elastic modulus, E_e. These data further show the viscoelastic behavior of the tested ovarian tissue. The equivalent modulus at time 0 is affected by the viscous behavior of the tissue, with the true intrinsic elastic modulus of the tissue being lower than the equivalent modulus at time 0 ($E_{eq,0}$). This is further explored by comparing E_e, $E_{eq,0}$, and the apparent modulus (E_a) that is calculated from the Hertz model and conventionally reported in the literature for AFM indentation studies. These three moduli for the cortex (C) and medulla (M) of reproductively younger and older cat ovaries are shown in **Figure 2.6A and B**, respectively. The same trends seen for the apparent modulus (E_a) held for the equivalent modulus at time 0 ($E_{eq,0}$) and the intrinsic elastic modulus (E_e), with the cortex showing statistically significant higher moduli than the medulla in both reproductively younger and older cats. Interestingly, we see that the values for the

intrinsic elastic modulus are lower than the values for both the equivalent modulus at time zero and apparent modulus. Looking at all the modulus values evaluated from the stress relaxation measurements, we can see a statistically significant difference between $E_{eq,0}$ and E_e and between E_a and E_e However, there is no statistically significant difference between $E_{eq,0}$ and the apparent modulus (E_a) calculated from the Hertz model. The apparent modulus and the equivalent modulus at time zero are significantly higher than the intrinsic elastic modulus because these measurements are impacted by the viscoelastic behavior of the material. By fitting the 2nd-order SLS model to the experimental relaxation data, we are able to differentiate the elastic and viscous portions of the material behavior. The apparent modulus, most frequently used in AFM indentation characterization of biological tissue, is in fact comprised of both the intrinsic elastic modulus and the contribution of the viscoelasticity. It is worth noting that the equivalent modulus, $E_{eq,0}$, is affected by the initial stress, applied strain, and relaxation kinetics at time 0 (**Eq. A14**), which may explain the large variation in apparent elastic modulus values reported in the literature for AFM indentation. Standardization of the method for modulus measurement using AFM indentation is necessary to solve the problem.

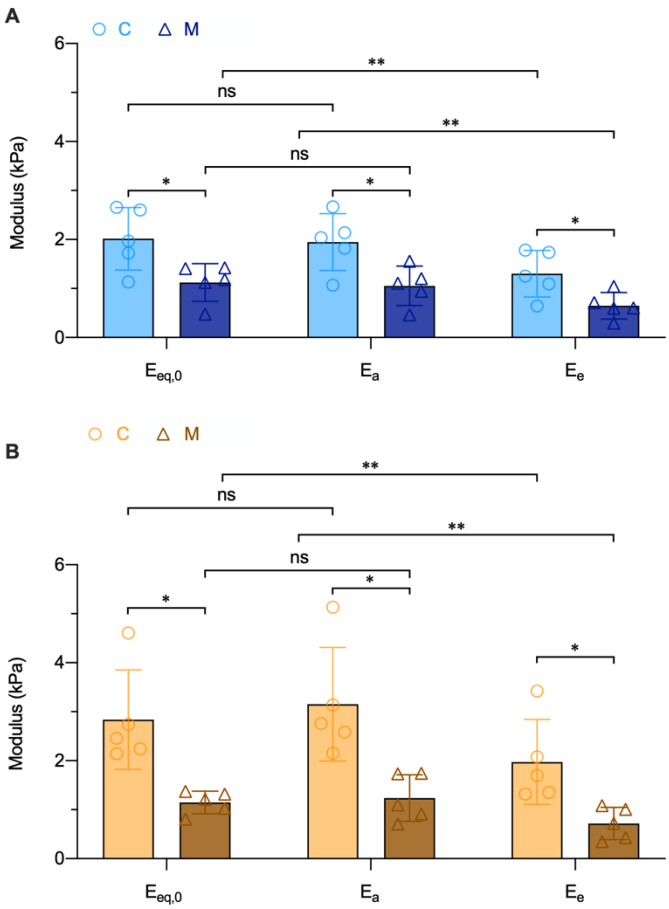

Figure 2.6 Characterization of the connection between the different moduli of cortex and medulla in cat ovarian tissue. A, Equivalent modulus at time zero ($E_{eq,0}$), apparent modulus (E_a), and intrinsic elastic modulus (E_e) of the ovarian cortex (C, light blue, circles), and medulla (M, dark blue, triangles) of reproductively younger cats (n=5). $E_{eq,0}$ and E_e were obtained by using the 2nd order SLS model to analyze the data from stress relaxation measurements. E_a was obtained using the Hertz model. B, $E_{eq,0}$, E_a and E_e of the ovarian cortex (C, light orange, circles), and medulla (M, brown, triangles) of reproductively older cats (n=5). Student two-tailed paired t-test. *$p < 0.05$, and **$p < 0.01$. Error bars represent standard deviation.

2.2.4 Possible connection of mechanical and compositional heterogeneities

The distribution and organization of extracellular matrix in the cortex and medulla of the ovary has been hypothesized to contribute to differences in mechanical properties between the two physical regions. We chose to examine the distribution of hyaluronic acid (HA) and collagen type I (COL-1), two common ECM macromolecules that have significance in the ovarian microenvironment and have been explored as

biomaterials for in vitro culture of ovarian follicles [33, 34, 46, 47, 111-114]. ECM distribution was characterized in the same orientation as the AFM indentation testing – transversely across the middle of the ovary (**Fig. 2.7A**). Consistent with previous findings in the ovary of other species, H&E staining of the cat ovary shows that the outer cortex regions (1 and 3) are rich with ECM and densely organized tissue, whereas the inner medulla (2) has less, more randomly distributed ECM (**Fig. 2.7B**). By fluorescently labeling these areas with biotinylated HA binding protein (HABP), we can see that HA is found in high density in the outer regions 1 and 3 of the ovary, while sparsely found in the inner region (2) in both reproductively younger (**Fig. 2.7C-D**) and reproductively older (**Fig. 2.7E-F**) ovarian tissues. This trend of HA distribution, with more HA seen in the outer edges (cortex) and less HA seen in the interior (medulla) aligns well with the measured apparent modulus (E_a) profile, where the highest modulus values seen at the outer edges of the ovarian tissue for both reproductively younger and older cats (**Fig. 2.4A-D**). Of note, the round holes in the micrographs of HA staining are due to the presence of follicles in the tissue; the round holes in the edge (1) images are in the same location of the early-stage follicles stained in the H&E images of the similar location. However, such trend is not observable for COL-1 in the cat ovary. For both reproductively younger (**Fig. 2.8A-B**) and older (**Fig. 2.8C-D**) cats, COL-1 is seen distributed throughout the ovary, with similar density in the cortical and medullar regions. COL-1 shows a high level of intensity across the ovary in samples from both reproductively younger and older cats.

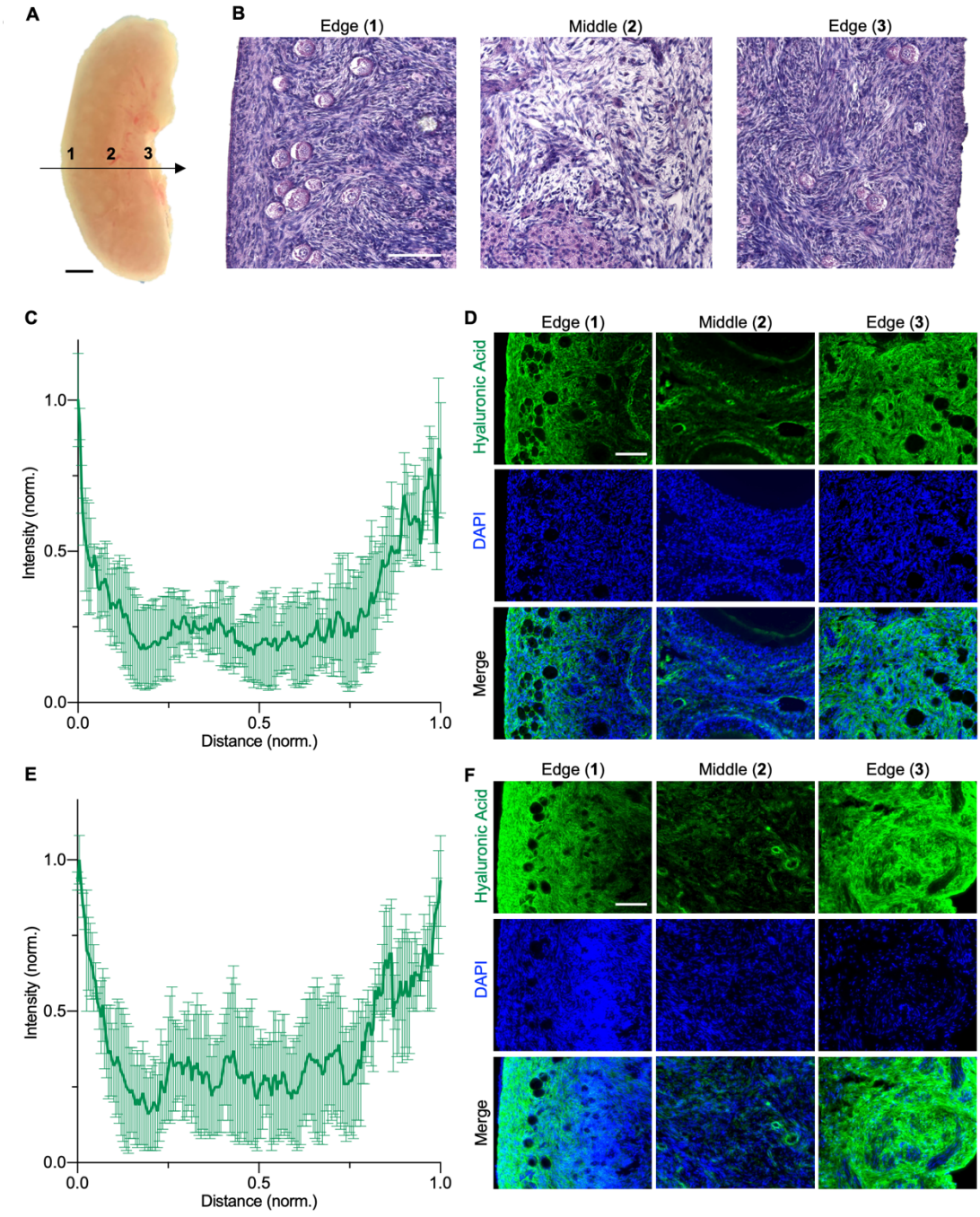

Figure 2.7 Distribution of hyaluronic acid (HA) in reproductively younger and older cat ovaries. A, Typical image of bisected cat ovary. The numbers 1, 2, and 3 indicate the edge, middle, and opposite edge locations of the ovary where images are further shown. Scale bar = 1 mm. **B**, Hematoxylin and Eosin (H&E) staining of regions of cat ovarian tissue, starting from the first edge (1) to the middle (2), to the other edge (3). Scale bar: 100 µm. **C**, Normalized intensity of HA staining fluorescence signal across the line profile of the ovaries of reproductively younger cats (n=3). **D**, Representative fluorescence images of the edge, middle, and edge of the reproductively younger cat ovarian tissue line profile showing HA (green) distribution. Nuclei are visualized using DAPI (blue). Scale bar: 100 µm. **E**, Normalized

intensity of HA staining fluorescence signal across the line profile of the ovaries of reproductively older cats (n=3). **F**, Representative fluorescence images of the edge, middle, and edge of the cat ovarian tissue line profile showing HA (green) distribution in reproductively older cats. Nuclei are visualized using DAPI (blue). Scale bar: 100 µm. Error bars represent standard deviation.

Although COL-1 distribution does not correlate with the modulus pattern in the cat ovarian tissue, HA distribution matches fairly well with the modulus by position seen in **Fig. 2.3**, suggesting that HA may be a key ECM material that contributes to the mechanical gradient in the ovary.

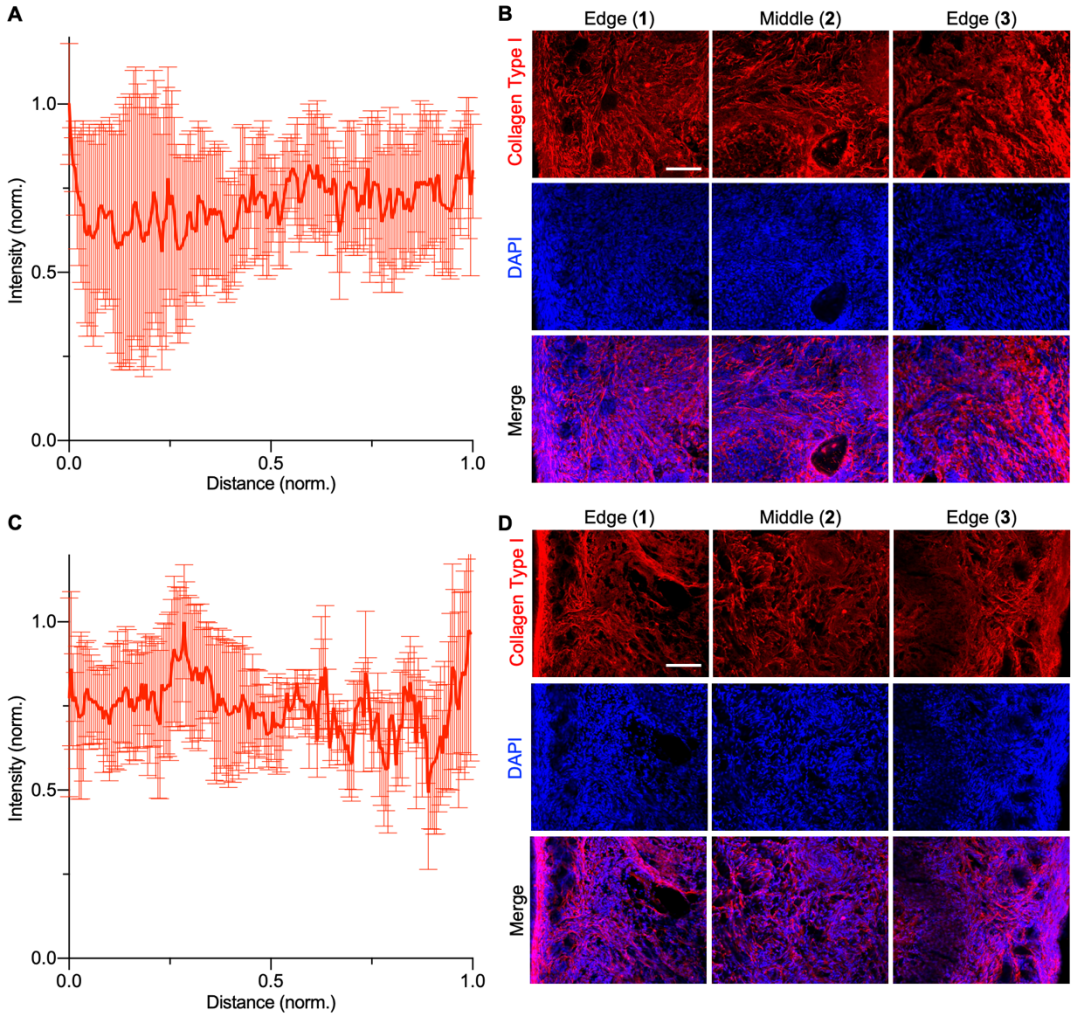

Figure 2.8 Distribution of collagen type I (COL-1) in reproductively younger and reproductively older cat ovaries. A, Normalized intensity of COL-1 staining fluorescence signal across the line profile of the ovaries of reproductively younger cats (n=3). **B**, Representative fluorescence images of the edge, middle, and edge of the reproductively younger cat ovarian tissue line profile showing COL-1 (red) distribution. Nuclei are visualized

using DAPI (blue). **C**, Normalized intensity of COL-1 staining fluorescence signal across the line profile of the ovaries of reproductively older cats (n=3). **D**, Representative fluorescence images of the edge, middle, and edge of the cat ovarian tissue line profile showing COL-1 (red) distribution in reproductively older cats. Nuclei are visualized using DAPI (blue). Scale bars: 100 μm.

To further examine how HA may contribute to the increased modulus seen in the cortex compared to the medulla, ovaries from reproductively older cats were treated with hyaluronidase (HAse) to degrade HA in the tissue and then tested using AFM indention to measure the apparent modulus across the ovary. The modulus profiles of the HAse-treated ovaries still show heterogeneity, with the modulus being the highest at the edges of the tissue and decreasing towards the center (**Fig. 2.9A**). Importantly, comparing the average modulus linescan of HAse-treated ovaries to untreated ones, the cortex modulus values of the HAse-treated ovaries are lowered, but the medulla modulus values remain similar to that of the untreated ones (**Fig. 2.9B**). The apparent modulus of the cortex region shows a statistically significant decrease in the HAse-treated ovaries compared to those in the untreated group (**Fig. 2.9C**). There is no statistically significant difference in the modulus between the medulla of the HAse-treated and untreated ovaries. By normalizing the cortex and medulla modulus values of both treated and untreated ovaries to the mean modulus measured in the untreated ovaries, the HAse treatment can be seen to reduce the cortex modulus by ~50% (**Fig. 2.9D**). These data show that HA in the cortex is a significant (albeit not the only) contributor to the mechanical heterogeneity in older cat ovaries.

The viscoelastic heterogeneity in the cortex and medulla seen in older cats (**Fig. 2.4B**) may relate to the ECM distribution. The cortex in reproductively older cat ovaries has a high apparent modulus and shorter second relaxation time constant than the medulla that has a lower modulus and much higher and wider spanning second

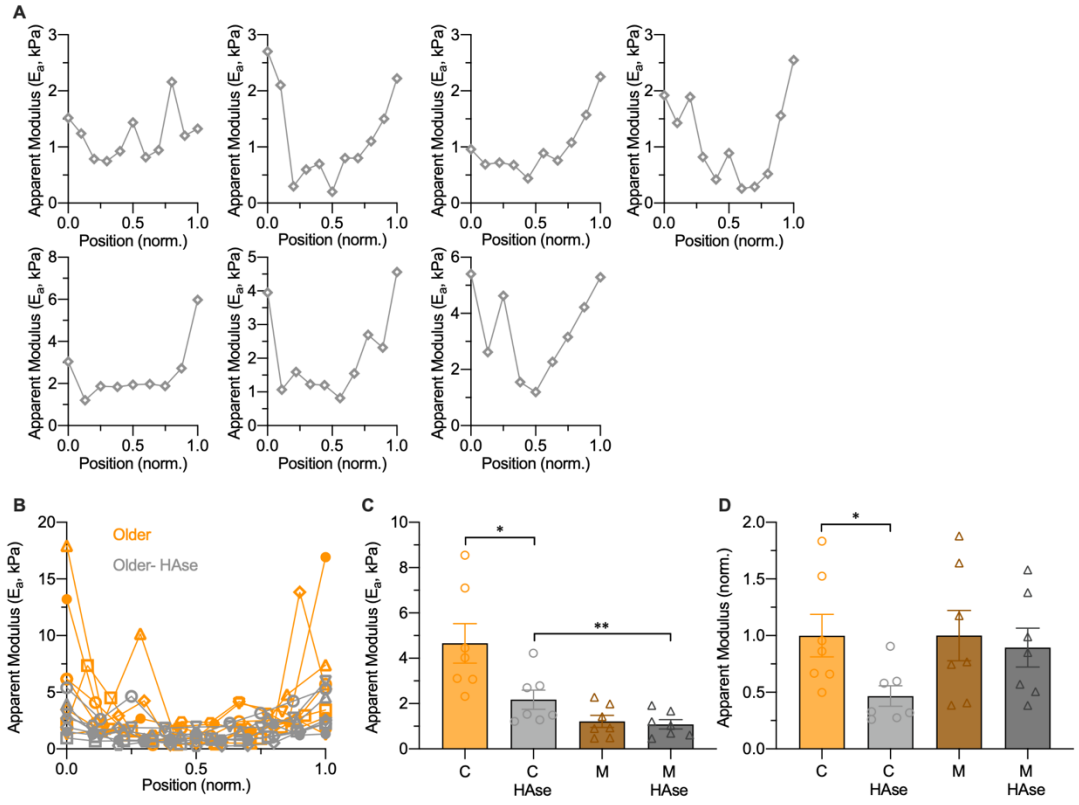

Figure 2.9 Hyaluronidase (HAse) treatment of older ovaries. **A**, Apparent modulus linescan profiles of reproductively older ovaries treated with hyaluronidase (HAse, gray) to degrade HA in the tissue. Markers indicate mean apparent modulus values from one mapping site on the tissue, averaged from three separate 30 µm x 30 µm indentation maps taken at the 100 x 100 µm2 spatial window of the mapping site. Mapping sites were spaced 100 – 500 µm apart by manual stage adjustment. Position is normalized to the maximum width of the ovary, which varied because the size of the ovary varied between animals. **B**, Apparent modulus linescans based on normalized position across the ovary. Each ovary linescan is represented by a different symbol, showing all linescans from both untreated (orange) and HAse-treated (gray) ovaries. **C**, Mean apparent modulus of the regions defined as cortex and medulla in reproductively older cat ovaries both untreated (cortex: orange, medulla: brown) and treated with HAse (cortex: gray, medulla: dark gray). **D**, Normalized apparent modulus of the cortex and medulla of reproductively older cats with and without HAse treatment. Cortex and medulla values are normalized to the mean value of the cortex and medulla of reproductively older ovaries without HAse treatment. Error bars represent standard deviation. *$p < 0.05$, **$p < 0.01$

relaxation time constant. HA and COL-1 are both highly expressed in the cortex, while the medulla shows lower expression of HA but similar expression of COL-1. This suggests that distribution of HA and COL-1 in the cortex contributes more to its elastic behavior, while the low expression of HA and homogeneous distribution of COL-1 in the medulla contributes more to its viscoelastic behavior. HA and collagen have been

linked to the mechanics of the ovary in other species. In mice, HA was reported to decrease in the ovarian stroma with the increase in age, and this is associated with increased ovarian stiffness [47], possibly due to aging-related formation of fibrotic tissue that is abundant in highly crosslinked collagen with high modulus. Indeed, the same study reported an important role for collagen in aging-related increase in stiffness by showing that treatment of reproductively older ovaries with collagenase softens the tissue environment to that of the reproductively younger mouse ovaries [47]. Further, COL-4 distribution in the mouse ovary has been shown to follow a similar distribution pattern as we report for HA in the cat, with higher expression seen near the outer edges and lower in the middle [96]. However, in bovine ovaries, the amount of COL-4 was reported to not differ between the cortex and the medulla [97]. These differences in trends between species merit further investigation to identify key ovarian matrisome components and their contributions to the mechanical differences between the ovarian cortex and medulla.

2.3 Conclusions

We have spatially mapped the elastic and viscoelastic behavior of the cat ovary interior for the first time, revealing mechanical differences between the cortex and medulla. We further show that age has an impact on the modulus of the cat ovary, adding to the supporting body of research demonstrating that ovarian tissue stiffens with age. Importantly, we are able to differentiate between the elastic and viscoelastic material behavior of the ovarian tissue with the 2nd-order SLS model for viscoelasticity, showing that the intrinsic elastic modulus is significantly lower than the apparent modulus reported in literature to characterize biological tissue by AFM indentation

measurements. We link this heterogeneous spatial tissue property with that of density of an important ECM macromolecule, HA, to understand the relationship between the ECM components and the micromechanical environment experienced by ovarian follicles. This mechanical characterization of real cortex and medulla elastic and viscoelastic behaviors of the ovarian microenvironment can help guide the development of better 3D ovarian follicle culture platforms for reproductive medicine to treat infertility due to dysfunctional follicle development associated with diseases like premature ovarian failure (POF) and PCOS.

2.4 Materials and Methods

2.4.1 Ovary collection

Whole ovaries were obtained by routine ovariohysterectomy of cats of 2 months – 2 years old performed at the Spay Spa and Neuter Nook (Davidsonville, MD, USA). Ovaries were stored and transported in L-15 medium containing 0.5% penicillin/streptomycin (Invitrogen, Carlsbad, CA, USA) and kept on ice until use within 24 h of surgery. The ages of the cats from whom ovarian tissues were tested are listed in **Table 2.1**.

Table 2.1. Ages of cats tested. Ages of cats (in months) tested via AFM characterization to characterize apparent modulus or stress relaxation behavior grouped by reproductive age (younger, <6 months; older, >6 months).

Test	Age Classification	Age of Cat (months)							Average Age (months)
Apparent Modulus	**Younger**	2	2.5	5	3.5	5.5	5	5	4.1 ± 1.4
	Older	11	24	8	9	7	10	12	11.6 ± 5.7
Stress Relaxation	**Younger**	5	5	2	4	4			4.0 ± 1.2
	Older	12	12	10	24	24			16.4 ± 7.0

2.4.2 Atomic force microscopy (AFM) sample preparation

Under stereomicroscope, ovaries were cleared of extraneous tissue (uterus, oviduct, and fat) from the reproductive tract in L-15 medium supplemented with 0.5% penicillin/streptomycin and washed with 1x phosphate buffed saline (PBS). A 2% (w/v) agarose solution was prepared by microwaving for 2 min to dissolve the agarose and allowed to cool (~5 min) and partially solidify in a 35 mm petri dish. The whole ovary was embedded in the cooled agarose solution, which was left to solidify completely (~15 min). The ovary was then bisected in the agarose gel using a razor blade and fixated on a 35 mm imaging dish (ibidi, Fitchburg, WI, USA) with transglutaminase (Moo Gloo, Modernist Pantry, Portsmouth, NH, USA) using a previously reported protocol[115]. Briefly, a 1:4 (v/w) transglutaminase:deionized water slurry was prepared according to the manufacturer's instructions, applied to the dish, and allowed to set for 10 min. Then, the bisected ovary slice was placed on the dish and allowed to cure for 30 min. Afterwards, 1x PBS was added to the dish to keep the tissue hydrated. The imaging dish with ovary sample was placed in a stage incubator attachment for AFM testing.

2.4.3 AFM indentation measurements

A NanoWizard 4 XP Bioscience AFM (Bruker, Billerica, MA, USA) mounted on an inverted light microscope was used for all AFM measurements. Material properties were measured by indentation across a transverse section of the ovary. A microrheology cantilever with a 10 μm (radius) spherical probe tip (Bruker) and nominal spring constant of 0.25 N/m was used for all indentations. The stage incubator maintained the fluid environment temperature at 37 °C for the duration of the

measurements. Before each experiment, the sensitivity of the cantilever was calibrated using a force curve collected in 1x PBS on a clean glass slide. The spring constant of the cantilever was determined by the thermal noise spectrum collected in 1x PBS with the AFM instrument [116].

Samples were equilibrated on the AFM heated incubator stage in 1x PBS before data collection began. Using the microscope viewing display, the probe was lowered over a region of the ovary just at the interface with the surrounding agarose gel (outer edge of the ovary) for indentation measurements. Care was taken during the measurement to test the ovarian stroma (visible through the AFM microscope) and avoid indenting the follicles in the ovarian tissue. Indentation-based measurements were carried out across a line profile of exposed ovary at mapping sites (**Fig. 2.1A**) approximately 200 μm apart by manually adjusting the stage position. At each of these mapping sites, three 30 x 30 μm^2 non-overlapping force maps were taken in the 100 x 100 μm^2 spatial window for the measurement site. Each 30 x 30 μm^2 force map consisted of 64 force-indentation measurements, resulting in 192 force-indentation measurements for each mapping site. Each force-indentation measurement was analyzed to extract the apparent modulus, and modulus values for each mapping site (192) were averaged to give one apparent modulus value for each mapping site. For samples tested for viscoelastic behavior, 3 stress relaxation measurements were taken at each mapping site in the tissue. The stress relaxation measurements were performed using the AFM's piezoelectric drive to control the z-position of the cantilever. First, the cantilever tip (i.e., probe) was made to contact the surface of the ovarian tissue by imposing a small setpoint force (<1 nN). Then, the probe was retracted, and force data

was collected for 30 s at 2 Hz to establish a baseline and capture system drift during the measurement. Then, the probe was indented into the tissue at a rate of 2.0 μm/s and data was collected at 5 Hz for 2 s. The probe was held at the resultant indentation displacement (constant indentation depth of 4 μm) for 60 s while the force data was collected at 5 Hz. The cantilever then was retracted above the tissue. The thickness of the bisected ovarian tissue tested was on the millimeter scale (approximately 1 mm).

2.4.4 AFM data analysis

The approaching curves of the indentation measurements (**Fig. 2.1B**) were analyzed to determine the values for apparent (elastic) modulus using the BioAFM's data analysis software according to the software workflow for evaluating the modulus. Briefly, linear baseline fitting was performed in the region of the curve where the probe was not in contact with the tissue (position of – 5 – 0 μm in **Fig. 2.1B**) to remove the effect of system drift on analysis. Then, the deflection-extension curves were converted into true force-distance curves using the measured value of the cantilever spring constant and sensitivity. Each force curve was accepted or rejected based on requiring a minimum of 25 nN of experienced cantilever force to ensure good indentation into the tissue. Then, the contact point of the force-deflection curve was chosen via the software to establish the beginning of tissue indentation. The apparent modulus was determined by a Hertz model [117] fit of the indentation curve into the tissue using the BioAFM's data analysis software, assuming a spherical probe tip with a radius of 10 μm. An assumed Poisson's ratio of 0.45 was used for the model fitting, representative of the values quoted for soft tissues[118].

Stress relaxation measurements were exported into MATLAB 2021 (Mathworks, Natick, MA, USA) for further processing. First, the effects of system drift during the experiment were corrected by using linear baseline fitting of the first 30 s of force data collected off the tissue and extrapolating that linearly for subtracting from the measured force when the strain was held constant (stress relaxation). The 60 s of measured force during the relaxation experiment was converted to stress based on the contact area of the AFM probe. The stress relaxation data was fit with a second-order standard linear solid (SLS) model of viscoelasticity consisting of a spring in parallel with two Maxwell arms (a spring in series with a dashpot) shown in **Figure 2.1C**. Each viscoelastic Maxwell arm consists of a purely elastic spring in series with a Newtonian fluid dashpot that renders the Maxwell arm to deform continuously under any stress. Due to the purely elastic spring arm that prevents continuous deformation under any stress, the SLS model is a solid model overall and is appropriate for modeling the viscoelasticity of solid soft tissues like the ovarian tissue studied in this work. The constitutive equation for teach of the three arms are given in the Appendix where the constitutive equation for this 2nd order SLS model overall is derived as follows:

$$\sigma + \left(\frac{\mu_1}{E_1} + \frac{\mu_2}{E_2}\right)\frac{d\sigma}{dt} + \frac{\mu_1\mu_2}{E_1E_2}\frac{d^2\sigma}{dt^2} = E_e\varepsilon + \left(\mu_1 + \mu_2 + \frac{E_e\mu_1}{E_1} + \frac{E_e\mu_2}{E_2}\right)\frac{d\varepsilon}{dt} + \frac{\mu_1\mu_2E_2 - {\mu_2}^2E_1 + \mu_1\mu_2E_e}{E_1E_2}\frac{d^2\varepsilon}{dt^2} \quad \textbf{(Eq. 2.1)}$$

where σ is stress that is a function of time (t); E_1 and E_2 are the modulus of the spring in the first and second Maxwell arms, respectively; μ_1 and μ_2 are the viscosity of the dashpots of the first and second Maxwell arms, respectively; E_e is the intrinsic elastic modulus of the material; and ε is the strain experienced by the tissue. More information

on the expressions for the total stress, total strain, and stresses on the purely elastic solid arm and the two Maxwell arms of the second-order SLS model can be found in the Appendix (**Eqs. A1-A5**). In the case of stress relaxation for which ε is held constant as ε_0 and $d\varepsilon/dt$ is 0, this equation becomes as follows:

$$\sigma + \left(\frac{\mu_1}{E_1} + \frac{\mu_2}{E_2}\right)\frac{d\sigma}{dt} + \frac{\mu_1\mu_2}{E_1E_2}\frac{d^2\sigma}{dt^2} = E_e\varepsilon_0 \qquad \textbf{(Eq. 2.2)}$$

With the initial condition of $\sigma_0 = E_e\varepsilon_0 + \sigma_{1,0} + \sigma_{2,0}$, where $\sigma_0, \sigma_{1,0}, \sigma_{2,0},$ are the total stress, stress on the first Maxwell arm, and stress on the second Maxwell arm at time zero, respectively, the solution to the differential **Eq. 2.2** is as follows:

$$\sigma = E_e\varepsilon_0 + \sigma_{1,0}e^{-t/\tau_1} + \sigma_{2,0}e^{-t/\tau_2} \qquad \textbf{(Eq. 2.3)}$$

where τ_1 $(= \mu_1/E_1)$ and τ_2 $(= \mu_2/E_2)$ are the relaxation constants of the first and second Maxwell arms, respectively. The time-dependent equivalent modulus (i.e., σ/ε_0) accounting for both the elastic and viscoelastic effect is indicated as E_{eq} and is shown in the following equation:

$$E_{eq} = E_e + \frac{\sigma_{1,0}}{\varepsilon_0}e^{-t/\tau_1} + \frac{\sigma_{2,0}}{\varepsilon_0}e^{-t/\tau_2} \qquad \textbf{(Eq. 2.4)}$$

The equivalent modulus at time 0 ($E_{eq,0}$) was evaluated using **Eq. 2.4** by setting *t* as 0. The relaxation data from the AFM indentation measurements were fit with **Eq. 2.3** by the nonlinear least squares fitting method in MATLAB. This model was used to extract material properties—E_e, τ_1, τ_2— from the cortex and medulla of ovarian tissue, together with $\sigma_{1,0}$ and $\sigma_{2,0}$ (**Table 2.2**), which were further used to calculate $E_{eq,0}$ using **Eq. 2.4** by setting time as 0.

Table 2.2 Parameters from viscoelastic modeling of ovarian tissue behavior. Model parameters extracted from fitting second order SLS model to stress relaxation data collected in cortex and medulla of reproductively younger and older cat ovarian tissues.

Age	Region	E_e (kPa)	$\sigma_{1,0}$ (Pa)	$\sigma_{2,0}$ (Pa)	τ_1 (s)	τ_2 (s)
Younger	**Cortex**	1.3 ± 0.6	12.7 ± 3.9	13.5 ± 4.2	1.1 ± 0.2	17.9 ± 5.9
	Medulla	0.6 ± 0.3	8.5 ± 3.7	12.1 ± 3.9	1.1 ± 0.3	19.9 ± 6.2
Older	**Cortex**	1.9 ± 0.9	13.5 ± 1.9	16.9 ± 8.5	1.1 ± 0.2	19.7 ± 5.0
	Medulla	0.7 ± 0.3	8.6 ± 3.1	9.6 ± 4.9	1.1 ± 0.3	37.7 ± 16.9

Further derivation and detail of the expressions for $\sigma_{1,0}$ and $\sigma_{2,0}$ together with $E_{eq,0}$ in terms of τ_1, τ_2, and E_e are given in the Supplemental Method 2 (Eqs. S6-S14), which shows that $\frac{\sigma_{1,0}}{\varepsilon_0} \neq E_1$; $\frac{\sigma_{2,0}}{\varepsilon_0} \neq E_2$; $E_{eq,0} \neq E_e + E_1 + E_2$; and that $E_{eq,0}$ is dependent on not only the intrinsic elastic modulus (E_e) but also all the viscoelastic properties (i.e., τ_1 and τ_2). Furthermore, per **Eq. 2.3**, **Eqs S4-S5** and **Eqs. S11-S14**, the E_1 always goes together with μ_1 as τ_1 and E_2 always goes together with μ_2 as τ_2 in the solution (or equation) for the time-dependent stress. This indicates that E_1 and E_2 only affect the stress relaxation rates, and they have no impact on the intrinsic elastic property that is independent of time. The latter is also clear from **Eq. 2.3**, by setting the time to infinity. Therefore, in the SLS model, there is a clear demarcation of the elastic and viscoelastic contributions through the purely elastic solid arm (E_e) and the two viscoelastic Maxwell arms (τ_1 and τ_2), respectively. This allows the identification of the possible number of different viscoelastic kinetics (Maxwell arms) by fitting the model with a various number of viscoelastic orders (i.e., viscoelastic kinetics or Maxwell arms) to experimental data. For example, two different viscoelastic kinetics (Maxwell arms) are identified in this study for ovarian tissue because the second-order SLS model can give

a good fit to the experimental data while the first-order SLS model cannot. The model parameters from 3 stress relaxation measurements at one 100 x 100 μm^2 mapping site were averaged to give one set of model parameters for each mapping site (Fig. 1A). Within each 100 x 100 μm^2 mapping site, three separate tests were performed at least 30 μm apart from each other. Each mapping site was 100-200 μm apart from each other, more than 10 times of the size of the probe used to test the tissue. Between each relaxation measurement, the tissue was allowed to recover for approximately 3 min.

2.4.5 Ovary fixation and staining

Ovaries for ECM and hematoxylin & eosin (H&E) analyses were fixed in ethanol-formalin-glacial acetic acid (70%, 10%, 5% v/v, respectively) overnight at 4 °C. Following fixation, ovaries were rinsed with 70% ethanol three times and stored in 70% ethanol at 4 °C. Within two weeks, the fixed samples were processed using an automated tissue processer (Leica ASP300 S), which includes dehydration, clearing, and infiltration of paraffin wax to preserve tissue structure per standard processing protocols. Then, samples were embedded into paraffin wax block, cut into 5 μm thick sections, and mounted on slides with tissue mounting medium (CC/mount, Sigma, St. Louis, MO, USA) for staining and analysis. Randomly selected slides were stained for H&E to examine tissue architecture and imaged with a Zeiss (Oberkochen, Germany) LSM 710 microscope.

2.4.6 Hyaluronic acid quantification

A hyaluronic acid binding protein (HABP) assay was performed on randomly selected slides from the ovary to examine HA distribution in the ovary according to

published protocols [119]. In brief, slides were deparaffinized and rehydrated in a graded alcohol series. Endogenous avidin and biotin were first blocked with an avidin/biotin blocking kit (Vector Laboratories, Burlingame, CA, USA), followed by blocking in 10% normal goat serum at room temperature to prevent nonspecific binding. Negative control sections were incubated with hyaluronidase (10 mg/mL, Sigma) for 1 h at 37 °C for degrading HA, to serve as a specificity control for background fluorescence. Experimental and negative control sections were incubated with biotinylated HABP diluted in 10% normal goat serum (1:100, MilliporeSigma, Burlington, MA, USA). The fluorescence signal was then amplified first by an Avidin-Biotin Complex reagent (VECTASTAIN ABC-HRP Kit, Vector Laboratories) and then by tyramide signal amplification (TSA, 1:400, Akoya Biosciences, Marlborough, MA, USA). Cell nuclei were visualized using 4',6-diamidino-2-phenylindole (DAPI, 1:1000). Slides were washed with 1x PBS and covered with tissue mounting medium (CC/mount, Sigma) and cover glass for fluorescence imaging. Epifluorescence images of HABP-strained ovary sections were captured using a Zeiss LSM 710 fluorescence microscope across a transverse line section of the ovary, similar to what was done in AFM mechanical testing. Three separate lines across the center of the ovary were measured for each ovary. The position on the line scan was normalized to the width of the ovary, to allow for comparison between samples since the size of the ovary varied based on animal. The fluorescence intensity profile normalized to the maximum fluorescence intensity of the transverse line of the ovary was quantified using the NIH (Bethesda, MD, USA) ImageJ (version 1.52q).

2.4.7 Collagen type I quantification

For immunostaining of collagen type I in ovarian tissue, randomly selected paraffin slides were deparaffinized and rehydrated in a graded alcohol series. Slides were blocked with 5% bovine serum albumin (BSA) to prevent nonspecific binding. Negative control slides were incubated in a collagenase solution (5 mg/mL) to degrade collagen in the sample. Slides were incubated with primary collagen type I antibody (COL-1, 1:400, Novus Biologicals, Centennial, CO, USA) overnight at 4 °C, then with a secondary antibody (goat anti-mouse Alexa Fluor 568) for 1 h at room temperature. Cell nuclei were visualized using DAPI. Images were taken and analyzed for COL-1 distribution in the same way as that for HA described above.

2.4.8 Statistical analysis

All graphing and statistical analyses were performed using GraphPad Prism 8 (GraphPad Software, San Diego, CA, USA). Data are reported as the mean ± standard deviation of the mean from at least three different animals. Student's two-tailed *t*-tests assuming equal variance were performed with no outliers excluded for comparison between groups. Unpaired tests were used for groups from different ovaries. Paired tests were used for comparison of values from cortex and medulla of the same cat ovary. The differences were considered statistically significant when the *p* value was less than 0.05 (*$p < 0.05$, **$p < 0.01$).

Acknowledgments

This work was partially supported by the National Science Foundation Graduate Research Fellowship Program (NSF GRFP) under Grant No. DGE 1840340 and by

National Institutes of Health (NIH) (R01EB023632 and R01AI172086). Any opinions, findings, and conclusions or recommendations expressed in this work are those of the author(s) and do not necessarily reflect the views of the NSF or NIH. The authors would like to thank the Spay Spa and Neuter Nook (Davidsonville, MD, USA) for graciously supplying cat ovaries from routine spay procedures.

Chapter 3 : Sand-mediated ice seeding enhances slow-freezing cryopreservation of human induced pluripotent stem cells and mouse preantral ovarian follicles*

3.1 Introduction

hiPSCs, with their capacity of differentiating into all the three germ layers [120], have tremendous value for both research to understand human diseases and clinical application to treat the diseases [121, 122]. For example, they have been explored for tissue engineering, disease modeling, and personalized medicine, which requires the ready availability of a large number of cells (up to billions) [121, 123-125]. Therefore, effective long-term cryopreservation or banking of hiPSCs to maintain high viability, function, and pluripotency of the cells for their wide distribution and future use is necessary for the eventual success of the emerging stem cell-based medicine [73-76]. Conventional hiPSC cryopreservation uses a slow-freezing method in the presence of 10% dimethyl sulfoxide (DMSO) as the cryoprotectant (CPA) and 10% fetal bovine serum (FBS) or serum replacement. DMSO is effective at protecting the cells from injury during cryopreservation but is highly toxic to cells and tissues at body temperature [77-80]. Furthermore, DMSO has been found to induce differentiation in more than 25 human stem cell lines [82] and cause changes in the cellular processes and epigenetic landscape of cardiac cells [83]. The use of fetal bovine serum (FBS) for cryopreservation poses the risk of spontaneous differentiation and introduction of possible xenogeneic pathogens into the hiPSC sample, which may cause adverse effect

* Partially reprinted (adapted) from: Jiang, B.*, Li, W.*, Stewart, S.*, Ou, W., Liu, B., Comizzoli, P., He, X. Sand-mediated ice seeding enables serum-free low-cryoprotectant cryopreservation of human induced pluripotent stem cells. Bioactive Materials 2021 6(12): 4377-4388.

to patients transplanted with the hiPSCs or their derivatives [84, 85]. These risks underscore the need for better hiPSC cryopreservation protocols.

Additionally, the demand of fertility preservation for medical and personal reasons has dramatically increased in recent years [86]. Mature oocyte and embryo cryopreservation are currently the most widely explored techniques for fertility preservation [50]. This method requires at least one cycle of controlled hormonal ovarian stimulation to collect the mature oocytes for either immediate banking or to produce embryos [51], which is not suitable for prepubertal patients, patients with hormone-responsive diseases, or patients who cannot delay disease treatment to undergo hormonal stimulation [53]. Embryo freezing not only faces potential legal, moral, ethical, and religious concerns [55], but does not allow for reproductive autonomy for the patient—they must rely on a sperm source, either from a partner or donor, to preserve their fertility [10]. Ovarian tissue cryopreservation is a promising option for pre-pubertal cancer patients and post-pubertal cancer patients who cannot undergo controlled ovarian stimulation [59]. However, for some patients, this approach carries the risk of re-introducing malignant cells that could have infiltrated the ovarian tissue prior to cryopreservation back into patients and causing cancer recurrence [61-63]. To address these challenges, isolation and cryopreservation of ovarian follicles, which have their own basement membrane to exclude the invasion of possible malignant cells, has been explored. Although results of cryopreserving isolated ovarian follicles using slow-freezing protocols have shown encouraging success [70, 126], the method still faces technical challenges that need to be addressed. For example, many

slow-freezing methods require the use of expensive programmable-rate freezers and manual ice-seeding in the sample at high subzero temperatures (above -10 °C).

During slow-freezing of cells in aqueous samples, ice nucleates and grows in the extracellular space first [127-129]. However, uncontrolled spontaneous ice nucleation is a stochastic event that often occurs at temperatures below -10 °C [130], which may be detrimental and often lethal to cells [131-134]. This is because the lower the subzero temperature when ice nucleation occurs, the more ice embryos (tiny aggregates of crystalline water molecules that spontaneously form) can be nucleated (and the finer ice crystals can be formed, due to the same amount of water available for ice embryos to grow in a given space) [130, 134]. At a low subzero temperature like -10 °C or below, the fine ice crystals formed outside cells may easily piece through the cell membrane to cause physical damage and induce the formation of fine ice crystals of intracellular water that is also deeply supercooled with high tendency of forming ice [131-134]. Intracellular ice formation (IIF) has been well-recognized to be a lethal event to cells in general [131-134]. In addition, the sudden/rapid ice formation at low subzero temperatures can cause a rapid increase in the local osmolality of the extracellular solution around the growing ice crystals, which may induce osmotic shock-associated damage to cells [134].

In contrast, controlled ice nucleation at a high subzero temperature enables the nucleation of reduced number of ice embryos that gradually grow into large ice crystals outside cells with further cooling, which may allow enough time for intracellular water to gradually diffuse out of cells in response to the gradual freezing of extracellular water to minimize both IIF and osmotic shock [131-134]. This is crucial for

cryopreserving stress-sensitive cells like embryos although the degree of its impact on the outcome of cryopreservation may be cell-type dependent [72, 134].

A number of methods have been used to control ice nucleation in samples during cryopreservation to improve the outcome [72, 135]. Early studies manually "seed" ice by introducing ice crystal into an undercooled sample [136]. Later, to reduce the risk for sample contamination, precooled probes, metal rods, or forceps have been used to create cold spots from the outside wall of the cell container (e.g., cryovial), thereby providing localized deep supercooling (usually below -20 °C) to induce ice nucleation in a sample that is above -10 °C overall [134, 137]. However, manual ice seeding is difficult to standardize and lengthy because it often requires multiple trials to induce ice formation. To address these issues, ice nucleators including the bacterium *Pseudomonas syringae* [138-141], crystalline cholesterol [142], and silver iodide [143, 144], have been added to the samples for inducing ice formation or seeding ice above -10 °C. However, these ice nucleators can be difficult to make in compliance with the current good manufacturing practice (cGMP) and/or are not biocompatible, and therefore are not suitable for cryopreserving clinical grade stem cells [72].

Inspired by the phenomenon in nature that ice is usually observed next to the bank of rivers, lakes, and ponds at high subzero temperatures in the winter, we discovered that sand particles immobilized in a plastic surface can initiate ice nucleation consistently above -10 °C in pure water. Based on this discovery, we further developed a simple and cost-effective method by utilizing sand to seed ice for cryopreservation of both cells (hiPSCs) and microtissues (ovarian follicles). This enables serum-free cryopreservation of hiPSCs with high viability (90%), pluripotency,

and function at a much-reduced cryoprotectant concentration (5%). We also show that mouse ovarian follicles cryopreserved using sand to nucleate ice at high subzero temperatures show higher immediate viability than samples without controlled nucleation and grow similarly to freshly isolated follicles for 9 days of in vitro culture. Sand particles can be easily immobilized on the inner plastic surface of the cryovials for holding cells to prevent them from entering the cell sample, and they can be conveniently separated from cells because sand has much higher density than cells. These together with the non-toxic nature of sand may make the sand-mediated ice seeding method very attractive for enhanced cryopreservation of hiPSCs, preantral ovarian follicles, and possibly many other types of cells for widespread research and clinical applications.

3.2 Results

3.2.1 Fabrication and characterization of sand-PDMS film

As illustrated in **Figure 3.1A**, sand-PDMS films were prepared for sticking on the inside wall in cryovials to seed ice and enhance the outcome of cryopreservation. The raw sands after cleaning (with water) and drying were gently sifted onto and partially embedded in a thin layer of uncured PDMS on top of a fully cured PDMS film using a mesh strainer with openings of 200 μm. After baking at 75 °C for 30 min to crosslink the uncured PDMS, the resultant sand-PDMS films are cut into small pieces (3 mm x 5 mm) and each piece is stuck via its smooth surface onto the inner wall of a cryovial for cryopreservation. The sand-PDMS film is soft and can be easily deformed onto the shape of the inner wall of cryovial for attaching to the wall via its smooth

surface without any sand. No sands are observed to detach from the film when using the cryovial attached with the sand-PDMS film for cryopreservation studies, probably because the sands are partially embedded in the top PDMS layer to prevent them from detaching.

The sands are heterogeneous in size in nature (**Fig. 3.1B**, before sifting). After sifting with a 200 μm mesh strainer, the size of the resultant sand particles partially embedded in the PDMS film is significantly more homogenous than that before sifting and their sharp morphology is appreciable in the high-magnification image (**Fig. 3.1B**). Scanning electron microscopy (SEM) imaging of the sand-PDMS film shows that the sand protrudes out of the surface of the film, which is not seen on the plain PDMS surface (**Fig. 3.1C**). This is further confirmed by the energy dispersive X-ray spectroscopy (EDXS) data showing the higher occurrence of Silicon (Si) in the sand-PDMS film than the pure PDMS film (**Fig. 3.1D-E**), because the natural sand is made of silicon dioxide. This exposed sand may serve to nucleate/seed ice in the cryopreservation solution outside cells during cooling, similarly to that observed near river/lake/pond bank in nature.

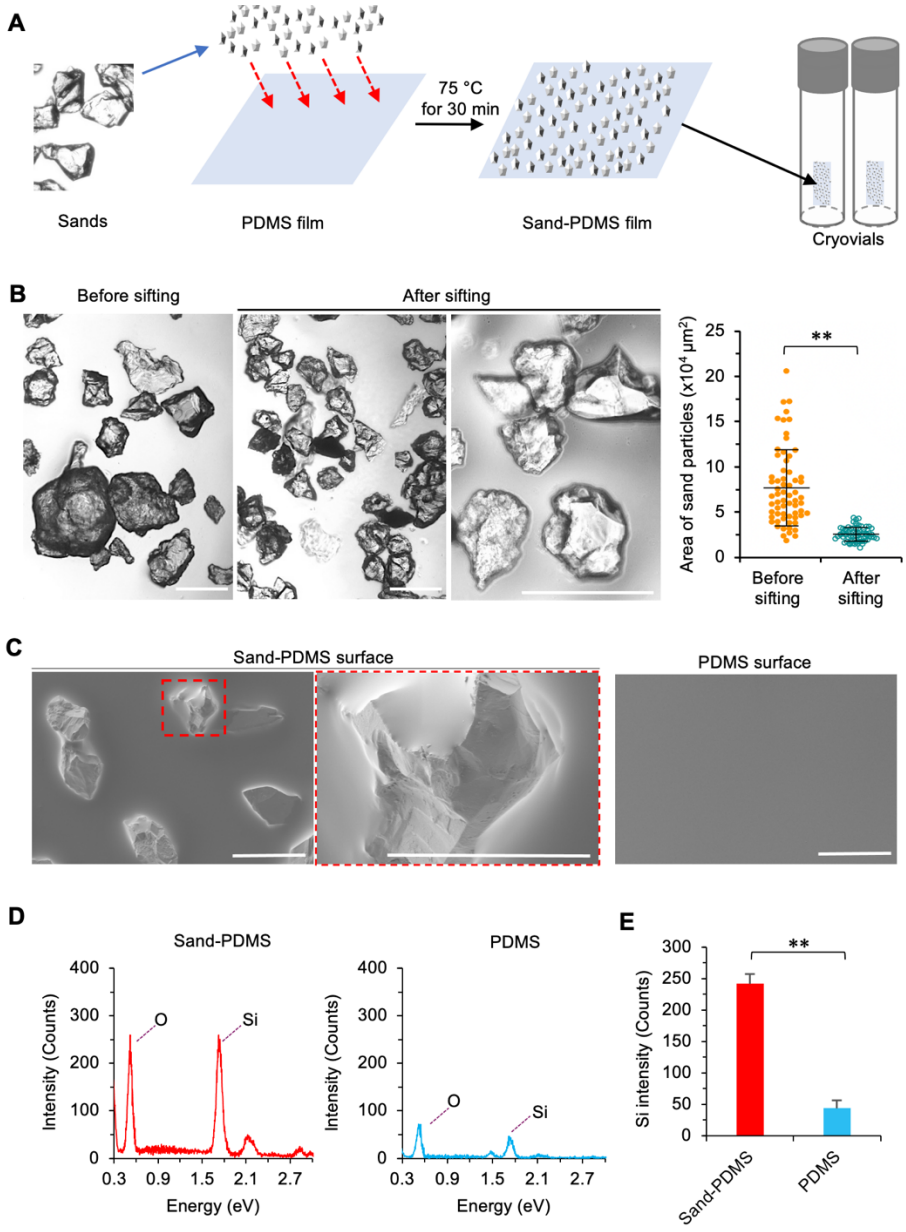

Figure 3.1 Preparation and characterization of sand-PDMS film. **A**, A schematic illustration of the procedure for preparing the sand-PDMS film: The sand was first rinsed overnight with water, autoclaved, dried, and then sifted onto a thin and uncured PDMS layer over a fully cured PDMS film through a mesh strainer with 200 μm openings. The PDMS film embedded with sand was baked at 75 °C for 30 min to form the sand-PDMS film. The sand-PDMS film was cut into small pieces and each piece was stuck/attached onto the inner wall of a cryovial via its smooth face. **B**, Morphology and size distribution of sands before and after sifting them through the mesh strainer. Also shown is a high-magnification view of the sifted sands where the sharp morphology of the sands is more appreciable. The size distribution was quantified based on the area of sand particles on the films. Data collected by Jiang, B. **C**, Scanning electron microscopy (SEM) image, showing the presence and morphology of sands partially embedded in the PDMS film. Data collected by Ou, W. **D**, Energy dispersive X-ray spectroscopy (EDXS) quantification of the elemental composition of the sand-PDMS and pure

PDMS films. The surface of the sand-PDMS film contains an increased amount of silicon (Si) and oxygen (O) than the pure PDMS surface. Data collected by Ou, W. **E**, Quantification of Si counts for the sand-PDMS and pure PDMS films using EDXS. Data collected by Ou W. Scale bars: 200 μm **, $p < 0.01$ (n = 3 independent runs).

3.2.2 Ice-seeding with sand-PDMS film

The effect of sand on the ice-seeding temperature of water is investigated by measuring the change in temperature over time during cooling. Ice-seeding in the sample can be detected by a sudden temperature rise (**Fig. 3.2A**), due to the release of latent heat of fusion as a result of ice nucleation and growth. Therefore, the temperature at which the sudden increase occurs is taken as the ice-seeding temperature. As shown **in Figure 3.2B**, the ice-seeding temperature of water without any film (control) is -15.9 ± 1.6 °C. The addition of a pure PDMS film containing no sand in the cryovial causes no significant change in the ice-seeding temperature (-14.9 ± 2.0 °C). Importantly, when the sand-PDMS film is added into the cryovial, the ice-seeding temperature increases significantly to -7.8 ± 1.6 °C.

This capability of sands in seeding ice at the high subzero temperature is confirmed by cryomicroscopy studies to cool cryopreservation solution (mTeSR medium containing 5% DMSO) at -1 °C/min, as shown in **Figure 3.2C** and **Movie 3.1**. Initially, there is no evident ice formation at -9.2 °C in the cryopreservation solution (**Fig. 3.2C**, 0 s) since the solution around or away from the sand is transparent (the slightly darker appearance near the sand is probably due to the shadowing effect of the sand). After 0.5 s, the solution next to the sand becomes darkened (indicated by the white arrow) compared to the solution away from the sand, indicating the sand induces ice formation in the solution. Growth of ice into the solution away from the sand can

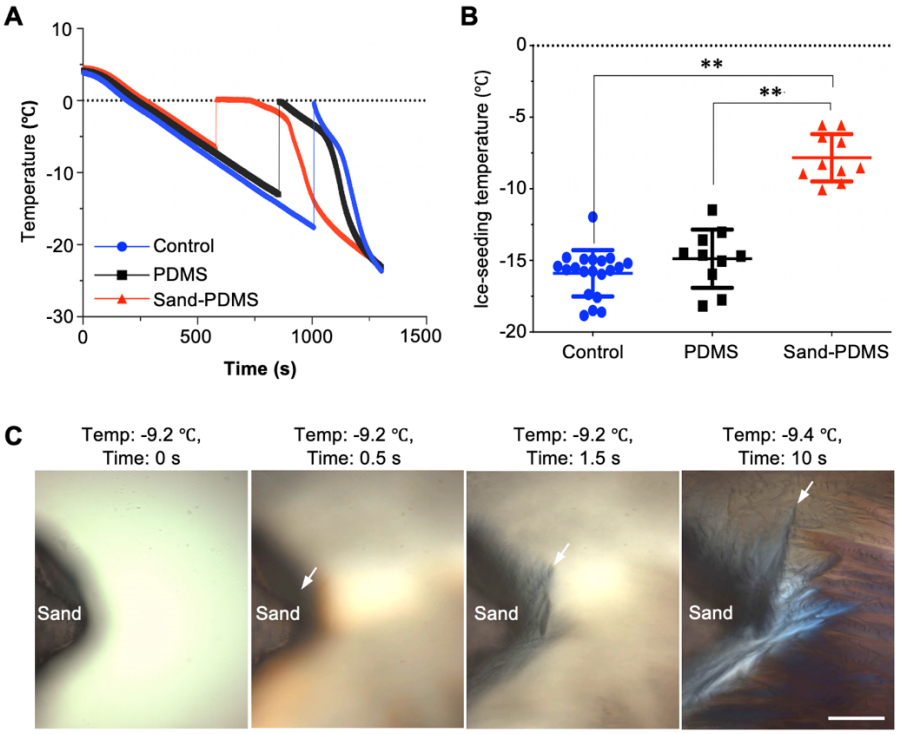

Figure 3.2 Sand enables ice seeding at high subzero temperature. **A**, Representative thermal histories in water containing no film (Control), pure PDMS film (PDMS), and sand-PDMS film (Sand-PDMS) during cooling. A sudden increase in temperature indicates ice seeding (which releases latent heat) in the sample. **B**, Quantitative data of the ice-seeding temperature in water under the aforementioned three conditions. **, $p < 0.01$ ($n = 10$ (for sand-PDMS film and pure PDMS film) or 20 (for Control), independent runs). **C**, Cryomicroscopy images at different times showing ice nucleation and growth around the sand particle during cooling the cell cryopreservation solution at subzero temperatures. Movie taken by Li, W., and analyzed by Stewart, S. Scale bar: 100 μm.

be seen at 1.5 and 10 s (one of the ice growth fronts is indicated by a white arrow in the image for each of the two times), during which the temperature decreases from -9.2 to -9.4 °C. This capability of sands in seeding ice in cryopreservation solution at a high subzero temperature may be useful for improving the outcome of cell and microtissue cryopreservation, which is tested using hiPSCs and preantral ovarian follicles.

The effect of sand on the ice nucleation temperature of the cryopreservation solution (10% DMSO + 0.1 M sucrose + 10% FBS in L15 medium) for follicle cryopreservation was investigated by measuring the change in temperature over time

during cooling. **Figure 3.3A** shows a representative thermal history of the cryopreservation solution without any film (control) and with a sand-PDMS film during cooling, with **Figure 3.3B** showing the quantitative results for the ice seeding temperature of the solution in both conditions. In the follicle cryopreservation solution, ice nucleates at an average temperature of -17.0 ± 2.2 °C with some trials showing ice nucleation as low as -20 °C in the absence of a sand-PDMS film, which can be deadly to cells. When the sand-PDMS film is added to the cryopreservation solution, the ice-seeding temperature shows a statistically significant increase to -13.9 ± 1.6 °C. The ice nucleation temperatures reported here are lower than those reported for sand in pure water in **Figure 3.2B**. This is most likely due to the presence of CPA in the cryopreservation solution tested: penetrating CPAs, like DMSO, can suppress the freezing point of solutions due to colligative properties (adding CPAs reduces the chemical potential of extracellular water) [145] and interference with the hydrogen bonding network of water molecules [146, 147].

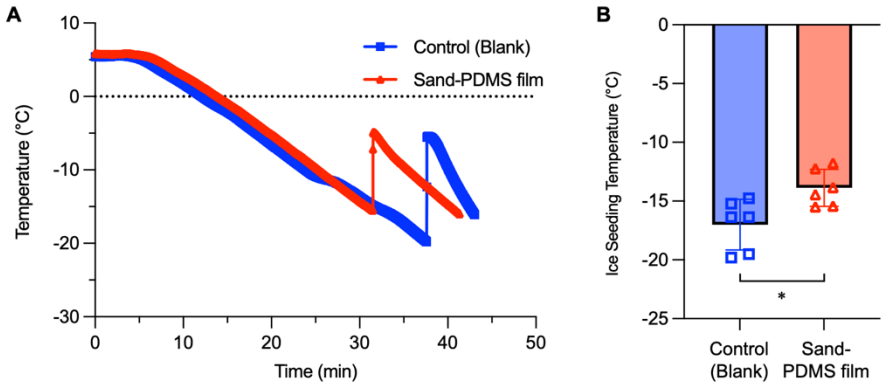

Figure 3.3 High subzero ice seeding temperature is enabled by the sand-PDMS film. A, Representative thermal histories of follicle cryopreservation solution during slow-cooling of samples with no film (Control (Blank)) and Sand-PDMS film (Sand-PDMS film). The ice seeding temperature is indicated by a sudden increase in temperature due to the release of latent heat in the sample. **B**, Quantitative data of the ice-seeding temperature in follicle cryopreservation solution under the aforementioned two conditions (n=6 independent runs). * $p < 0.05$.

To further understand the role that the characteristics of sand play in inducing ice nucleation, specifically surface roughness/sharpness and surface composition (silicon dioxide) that determines the surface properties including hydrophobicity. This is done by investigating the effect on ice seeding temperature of plastic shard-PDMS film and glass bead-PDMS film. The glass beads are made of silicon dioxide (as with sands) with a smooth surface (**Fig. 3.4A**), which is studied to understand the effect of surface roughness/sharpness on ice seeding. The plastic shards have sharp edge as with sands (**Fig. 3.4A**) but a different composition from sands, which is examined to understand the effect of composition that determines the surface property including hydrophobicity (sand is more hydrophilic than the plastic shards) on ice seeding. The glass bead-PDMS film can improve the ice seeding temperature significantly to -12.3 ± 1.8 °C from -15.9 ± 1.6 °C for water without anything for ice seeding (**Fig. 3.4B-C**). However, it is significantly lower than the ice seeding temperature (-7.8 ± 1.6 °C) for the sand-PDMS film. This indicates both the silicon dioxide material and surface roughness/sharpness are important for ice seeding. The ice seeding temperature for the plastic shard-PDMS film is -14.2 ± 1.1 °C (**Fig. 3.4B-C**), which is also significantly higher than that for control and significantly lower than that (-7.8 ± 1.6 °C) for sand-PDMS film. This further confirms the surface composition (that determines the surface property including hydrophobicity) is important for ice seeding. Collectively, these data indicate that both the surface composition (silicon dioxide) and roughness/sharpness render sands the excellent ice seeding capability. In addition, the ice seeding temperature for plastic shard-PDMS film is not significantly different from that (-14.9 ± 2.0 °C) of pure PDMS film while the ice seeding temperature for glass

bead-PDMS film is significantly higher than that of pure PDMS film, suggesting that the surface roughness/sharpness may be secondary to the surface composition (although both are important and might work synergistically) in determining the ice seeding temperature.

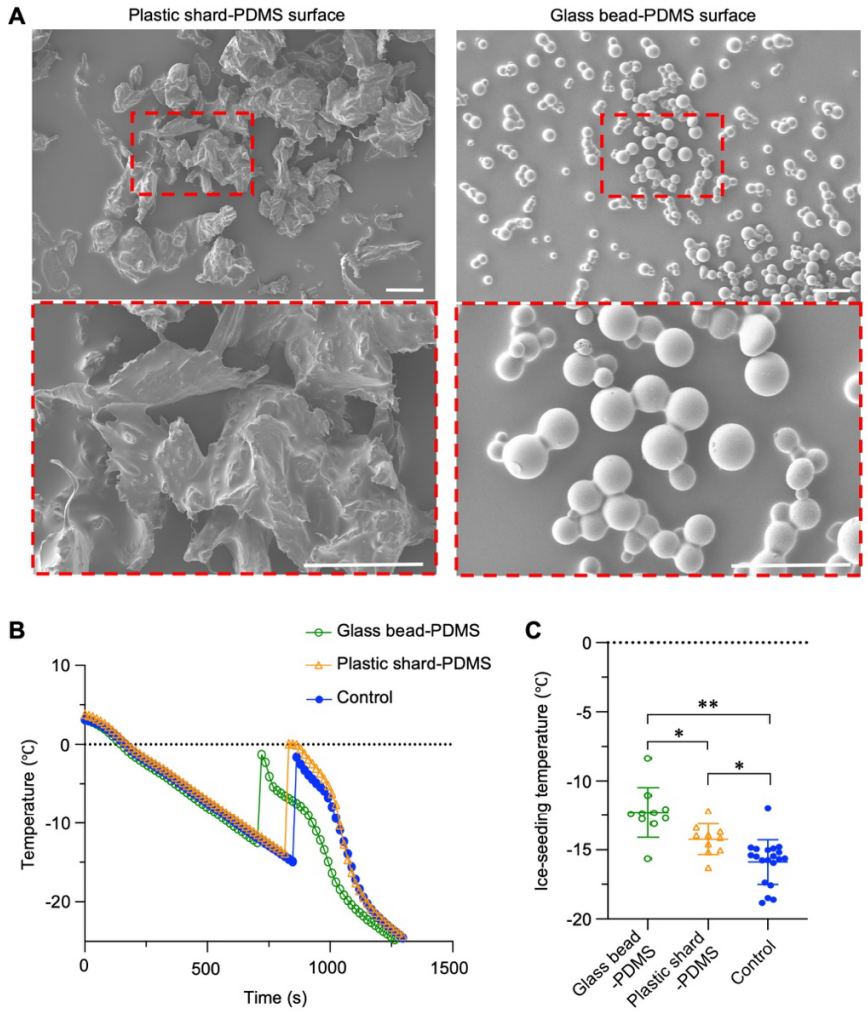

Figure 3.4 Ice nucleation/seeding with glass beads and plastic shards. (A) Scanning electron microscopy (SEM) image showing the presence and morphology of plastic shards and glass beads partially embedded in the PDMS film. The detailed morphology of the plastic shards and glass beads are more appreciable in the high-magnification views of the red dashed line-boxed areas. Scale bars: 200 μm. Images taken by Ou, W. (B) Representative thermal histories in water containing no film (Control), plastic shard-PDMS film, and glass bead-PDMS film during cooling. A sudden increase in temperature indicates ice seeding (which releases latent heat) in the sample. (C) Quantitative data of the ice-seeding temperature in water under the aforementioned three conditions. *, $p < 0.05$, **, $p < 0.01$ ($n = 10$ (for plastic shard-PDMS film and glass bead-PDMS film) or 20 (for control), independent runs).

3.2.3 Sand-mediated ice-seeding enhances immediate viability of cryopreserved ovarian follicles

The effect of this increased ice-seeding temperature mediated by the sand-PDMS film was explored for cryopreservation of preantral ovarian follicles by slow-freezing. Secondary ovarian follicles (size 100 – 150 μm) were cryopreserved in follicle cryopreservation solution with or without the addition of a sand-PDMS film on the wall of the cryovial and stored in LN2 for 1-4 weeks. After thawing, the immediate viability was assessed via live/dead staining, with representative images shown in **Figure 3.5A**, where live cells are stained green and dead cells are stained red. Fresh follicles (isolated and not cryopreserved) were also stained as a positive control. Morphologically normal and healthy secondary follicles isolated from ovarian tissue show a central, round oocyte surrounded by multiple layers of follicular cells. Freshly isolated follicles show this typical morphology, with the intact oocyte visible in the center of the round follicle surrounded by layers of supporting cells. Most of the cells in the fresh follicles stain green, indicating the fresh follicles are highly viable. There are some dead cells in the isolated follicles, most likely due to the isolation process causing some membrane damage to parts of the follicles. Many follicles cryopreserved without the sand-PDMS film also display healthy morphology and live/green staining, but cryodamage to the follicles is evident via the increase of red staining in the follicles, especially seen in the four follicles with bright and extensive red staining in **Figure 3.5A**, compared to the fresh control, indicating more dead/damaged cells. There are also more follicles in this group than the fresh follicles that show damaged follicle morphology, as represented in the blue dashed inset, where the oocyte is not clearly

visible, and the follicle does not appear healthy and round. Follicles cryopreserved using the sand-PDMS film more closely resemble the fresh follicles, with more whole follicles staining green and fewer dead cells; only two of the follicles in the representative image show bright red staining.

Figure 3.5B shows the quantification of this live/dead staining. Follicles with a live cell area (green only, no red staining) above 70% of the total follicle area were considered viable. Cryopreservation without the sand-PDMS film results in a significant decrease in viability (58.6 ± 16.4%) compared to both the freshly isolated control (84.1 ± 5.6%) and cryopreservation using the sand-PDMS film (77.3 ± 10.8%). There is no significant difference between the immediate viability of the freshly isolated control and the sand-PDMS film groups. These data of the immediate viability show a modest effect of the controlled ice nucleation on immediate cell viability via the sand-PDMS film.

3.2.4 Sand-mediated ice-seeding enhances in vitro growth of cryopreserved ovarian follicles

To further evaluate follicle quality beyond immediate viability, which, based on the live/dead staining assay, mainly reflects the cell membrane integrity measured by PI and esterase activity measured by the calcein-AM dye, cryopreserved follicles were cultured *in vitro* to measure follicle growth (an indicator of long-term viability) over time. Follicles cryopreserved with or without the sand-PDMS film were encapsulated in 0.25% alginate beads after thawing for 3D culture and the change in diameter was measured over 9 days of culture to quantify growth. Freshly isolated follicles were also cultured in the same way as a control. **Figure 3.6** shows

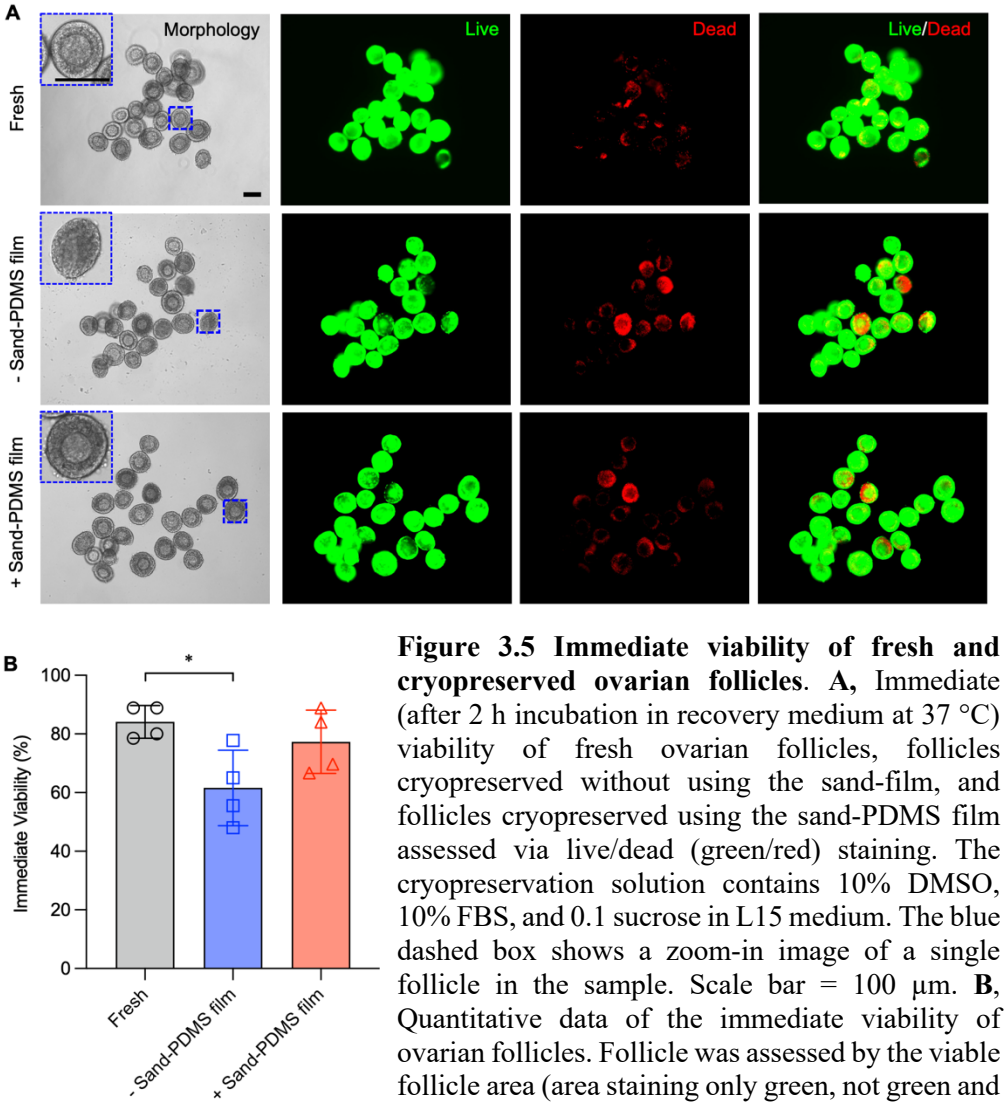

Figure 3.5 Immediate viability of fresh and cryopreserved ovarian follicles. **A,** Immediate (after 2 h incubation in recovery medium at 37 °C) viability of fresh ovarian follicles, follicles cryopreserved without using the sand-film, and follicles cryopreserved using the sand-PDMS film assessed via live/dead (green/red) staining. The cryopreservation solution contains 10% DMSO, 10% FBS, and 0.1 sucrose in L15 medium. The blue dashed box shows a zoom-in image of a single follicle in the sample. Scale bar = 100 µm. **B**, Quantitative data of the immediate viability of ovarian follicles. Follicle was assessed by the viable follicle area (area staining only green, not green and red). Follicles with a viable area of more than 70% are considered viable, and immediate viability is calculated as the number of follicles with a viable area of more than 70% over the total number of follicles in each independent run (n=4). * $p < 0.05$. One-way ANOVA followed by a Tukey *post hoc* correction was used for statistical analysis.

representative images of the follicles from the three culture groups- (1) freshly isolated follicles (Fresh), (2) follicles cryopreserved without the sand-PDMS film (- Sand-PDMS film), and (3) follicles cryopreserved with the sand-PDMS film (+ Sand-PDMS film)- on every other day of culture when diameter measurements were made. Most of the fresh follicles maintain the round morphology and intact oocyte through Day 9 in

culture and grow in size, indicating a healthy, properly functioning follicles. Most of the follicles cryopreserved without the sand-PDMS film show signs of damage on Day 1 of culture, with irregular morphology and a darkened oocyte. During culture, the follicles undergo atresia and shrink in size, and their darkened oocytes become barely visible in 9 days. Most of the follicles cryopreserved with the sand-PDMS film show round morphology similar to the fresh control on Day 1, with the oocyte clearly visible in the center of the follicle and normal surrounding layers of granulosa cells. The follicles maintain the round morphology during culture and grow in size similar to the fresh control on day 9.

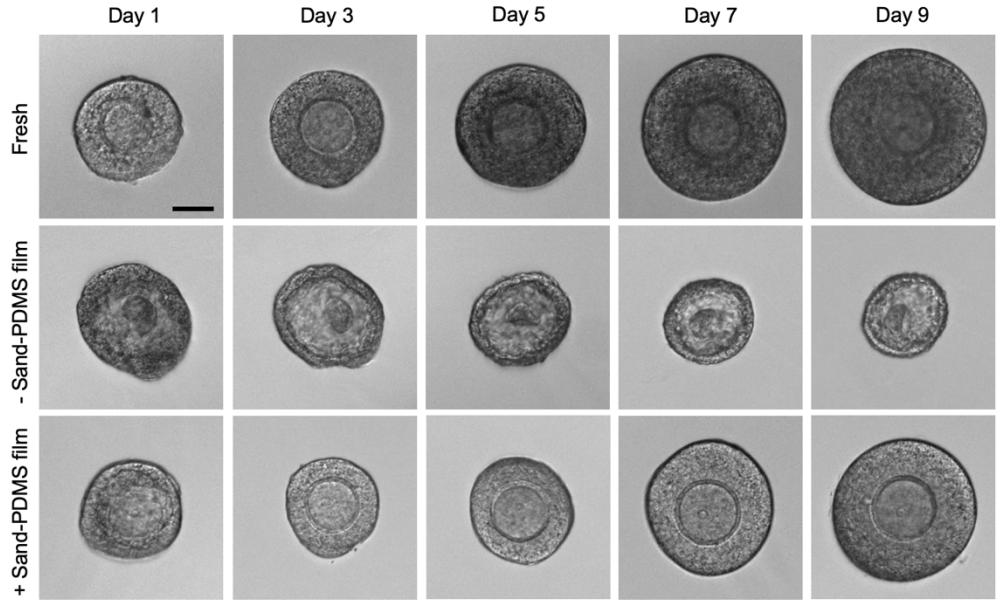

Figure 3.6 Representative morphology of fresh and cryopreserved ovarian follicles during in vitro culture. Follicles cryopreserved with or without the sand-PDMS film were thawed and encapsulated in 0.25% alginate for 9 days of in vitro culture. Fresh follicles were encapsulated on the same day of isolation as a control. Images of the follicle were taken every other day of culture, starting on day 1. Scale bar = 50 μm.

To quantify the growth of the follicles during culture, the diameter of the follicle on every other day of culture was measured and normalized to the original diameter on day 1 (D1) of culture. Follicle growth was thereby quantified by the ratio D/D1, where

D is the diameter of the follicle over time. A D/D1 ratio greater than 1 indicates that the follicle is growing, while a D/D1 ratio less than 1 indicates that a follicle is not growing and dying during the nine days of culture. In the fresh follicle group, the majority (52/60) of the follicles grow up to 2 times the original size by day 9 (**Fig. 3.7A**). Few follicles have a D/D1 less than 1 by day 9. For the follicles cryopreserved without the sand-PDMS film, most (58/70) of the follicles show a D/D1 less than 1 (**Fig. 3.7B**), indicating most of the follicles are damaged by the cryopreservation process and do not survive in long term. Few follicles are able to survive and grow in culture, as indicated by the scant number of curves above the D/D1 value of 1. For the follicles cryopreserved using the sand-PDMS film, the majority (40/71) show D/D1 values over 1 during culture (**Fig. 3.7C**), with some follicles showing a D/D1 ratio of up to 2 on day 9 similar to the fresh controls. However, there are a noticeable number of follicles that are damaged by the cryopreservation process and fail to grow in culture, as evidenced by the D/D1 values of less than 1 during the culture period.

This diameter ratio was used to quantify the number of surviving follicles in each condition during in vitro culture to evaluate follicle long-term survival. Follicles with a D/D1 ratio greater than 1 on day 9, which indicates that they can grow during culture, are considered viable. The survival is quantified as the number of viable follicles out of the total number of follicles cultured for each experimental group. Follicles cryopreserved with the sand-PDMS film have a similar survival rate compared to the fresh control, with no statistically significant difference (58.4 ± 22.5% versus 85.4 ± 12.8%, **Fig. 3.7D**). However, without the sand-PDMS film present during the cryopreservation process, the long-term follicle survival drops to 13.8 ± 17.9%. Out of

the 4 trials for the follicles cryopreserved without the sand-PDMS film, 2 trials did not have any surviving follicles after nine days of culture, while the other two trials had a survival of 20-40% on day 9. This may be due to the uncontrolled stochastic ice nucleation during the cryopreservation process; some trials may have had much lower temperatures of ice nucleation, resulting in increased damage to the follicles, while the other trials may have had ice nucleate at higher subzero temperatures. Because the sand-PDMS film is able to consistently nucleate ice at high subzero temperatures, there are no trials where the follicles cryopreserved with the sand-PDMS film are all damaged/dead. Although the difference in the long-term viability between the fresh follicles and follicles cryopreserved with the sand-PDMS film is not statistically significant, the follicles cryopreserved using the sand-PDMS film have a lower average long-term survival and a higher standard deviation. This indicates that there is still some damage to the follicle sample during the cryopreservation process, which could motivate further improvement of the cryopreservation solution composition and/or CPA concentration to protect the cells during the freezing/thawing process.

Comparing the growth curve of surviving follicles in the fresh and sand-PDMS film groups (**Fig. 3.7E**), follicles in both groups are able to grow up to 1.5 times of their original diameter on average by day 9. There is no significant difference between the growth (D/D1 ratio) of surviving follicles from the freshly isolated group and +sand-PDMS film groups on any day of in vitro culture, indicating that cryopreservation using the sand-PDMS film to nucleate ice does not cause lasting damage to the surviving ovarian follicles.

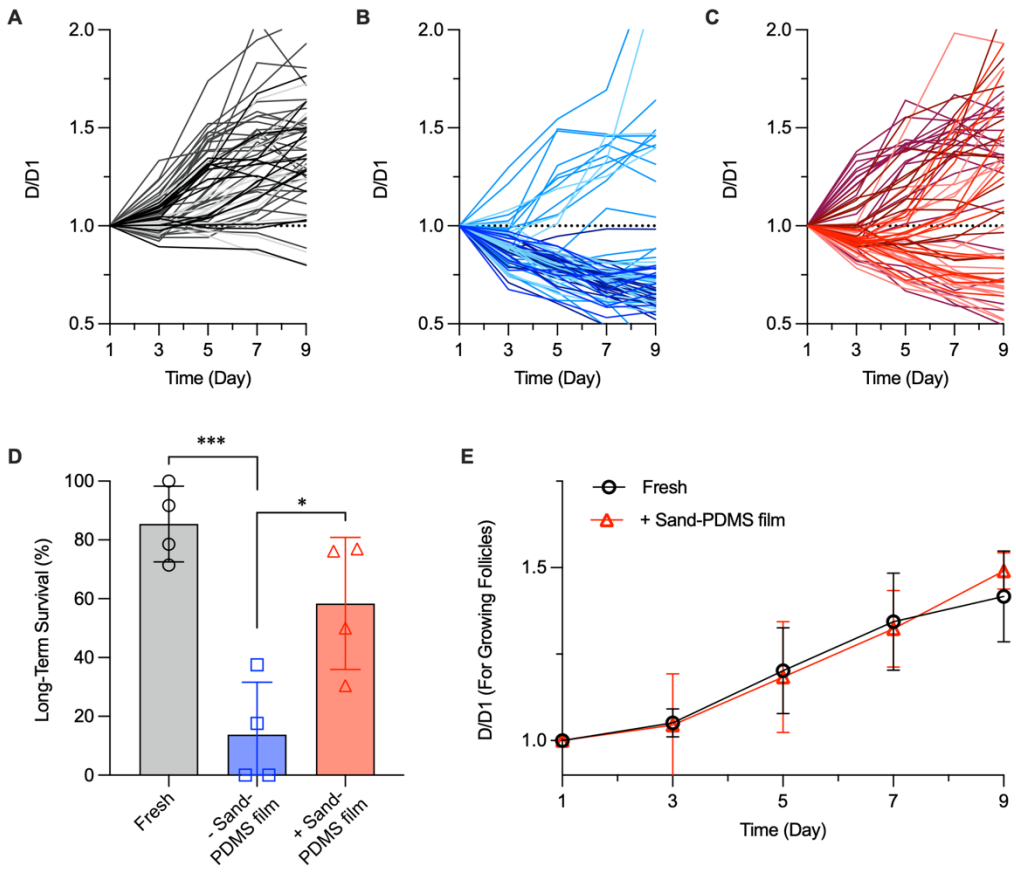

Figure 3.7 Growth and long-term survival of fresh and cryopreserved ovarian follicles during in vitro culture. Growth curves of **A**, freshly isolated follicles, **B**, follicles cryopreserved without the sand-film, and **C**, follicles cryopreserved using the sand-film during 9 days of in vitro culture (n=4 independent runs). Each curve represents the growth curve of one individual follicle. Each independent run is represented by a different shade of the experimental group's color. The growth of each follicle is evaluated by the diameter of the follicle (D) over time normalized to the diameter of the follicle on day 1 (D1). A D/D1 ratio over 1 means the follicle is growing in diameter, while a D/D1 ratio less than one signifies that a follicle is shrinking and dying during the 9 days of culture. **D**, Survival of the ovarian follicles after 9 days of culture. The survival is calculated as the percentage of the number of follicles with a D/D1 greater than 1 on day 9 out of the total number of follicles in culture (n=4 independent runs). One-way ANOVA followed by a Tukey *post hoc* correction was used for statistical analysis. **E**, Mean growth curves of freshly isolated follicles and follicles cryopreserved using the sand-film during 9 days of in vitro culture (n=4 independent runs). * $p < 0.05$, ** $p < 0.01$, *** $p < 0.001$. Two-way ANOVA with Sidak's post-test and correction was used for statistical analysis.

3.2.3 Enhanced cryopreservation of hiPSCs with sand-mediated ice seeding

To demonstrate the benefit of sand-mediated ice seeding for hiPSC cryopreservation, hiPSCs are cryopreserved by slow-freezing under various conditions

with or without the sand-mediated (by default) ice seeding: conventional method (10% DMSO and 10% FBS with no ice seeding), ice seeding alone, no cryoprotectant and no ice-seeding, 5% DMSO and no ice seeding, 2% DMSO and ice seeding, and 5% DMSO and ice seeding. **Figure 3.8A** shows typical live/dead (green/red) images of the hiPSCs cryopreserved under the various conditions and cultured for 2 h at 37 °C after thawing, and the corresponding quantitative data of cell viability are shown in **Figure 3.8B**. Without the use of any cryoprotectant, the sand-mediated ice seeding alone is insufficient to protect the cells from injury during the cryopreservation procedure, as indicated by the low cell viability under this condition (5.6 ± 2.1%) that is only slightly higher than that for the condition with no cryoprotectant and no ice-seeding (1.3 ± 0.6%). The use of 2% DMSO together with the sand-mediated ice seeding could improve the hiPSC viability to 37.3 ± 3.1%, showing the importance of using cryoprotectant to reduce cryoinjury to the cells. The cell viability is further improved albeit still modest for both the condition of 5% DMSO with no ice seeding condition (52.6 ± 3.5%) and the conventional method using 10% DMSO and 10% FBS (51.7 ± 4.0%). This demonstrates 5-10% DMSO could only protect up to ~50% hiPSCs from cryoinjury during cryopreservation and increasing DMSO from 5% to 10% does not significantly enhance the hiPSC viability in the absence of ice seeding. Importantly, high viability (90.3 ± 2.5%) of the hiPSCs after cryopreservation can be achieved by combining the sand-mediated ice seeding with 5% DMSO. This viability is significantly higher than that of the other control groups.

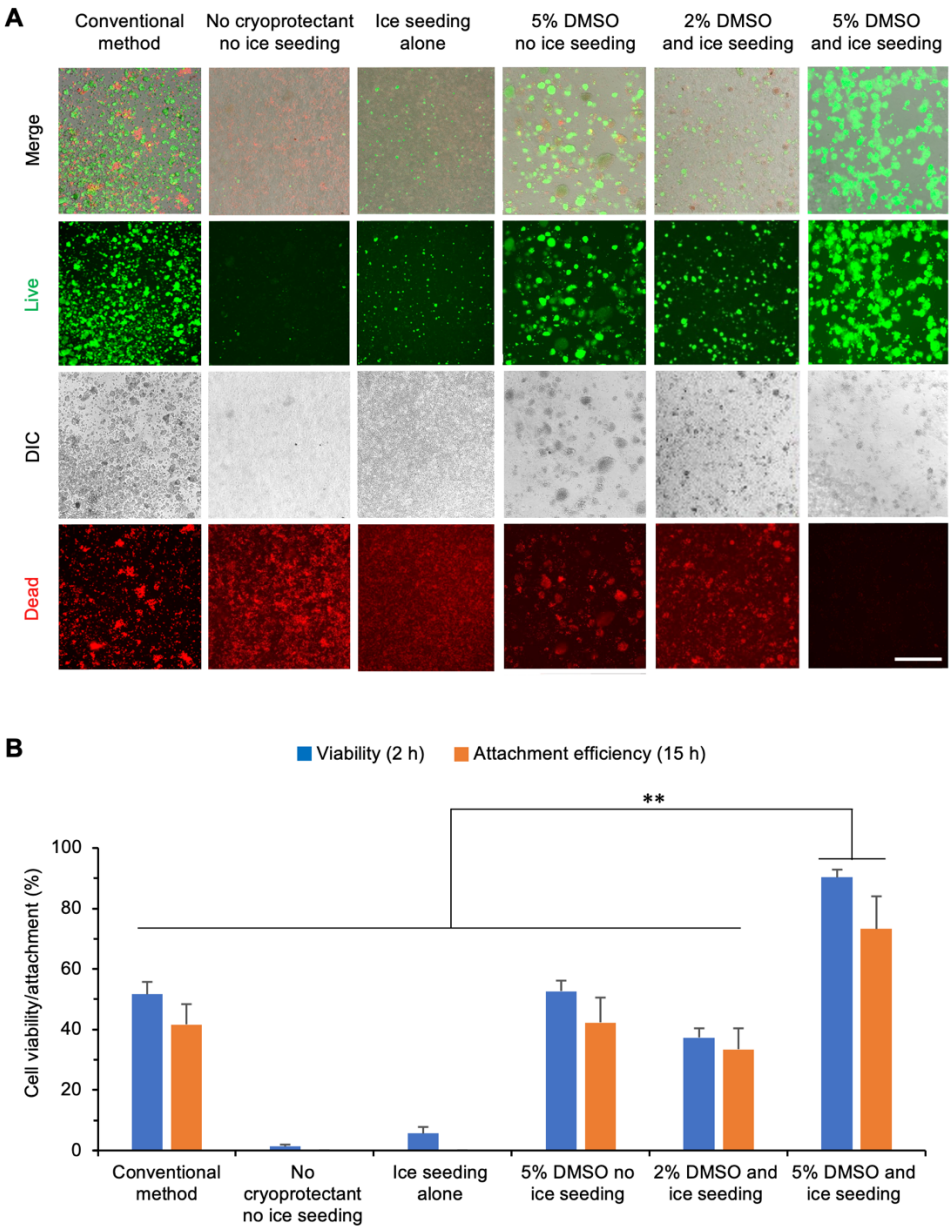

Figure 3.8 The immediate and long-term viability of hiPSCs after cryopreservation under various conditions. **A**, Immediate (after 2 h incubation at 37 °C) viability of hiPSCs assessed by live/dead (green/red) staining after cryopreservation with different methods: conventional method (10% DMSO+10% serum with no ice seeding), sand-mediated ice seeding alone, no cryoprotectant and no ice seeding, 5% DMSO with no ice seeding, 2% DMSO with ice seeding, and 5% DMSO with ice seeding. Scale bar: 500 μm. **B**, Quantitative data of the hiPSC immediate viability and attachment efficiency (i.e., long-term viability) after the various cryopreservation conditions. For quantifying the attachment efficiency, the cryopreserved cells were thawed and cultured for 15 h, and the number of attached cells was counted by hemacytometer. The attachment efficiency is calculated as the percentage of cells counted after cryopreservation out of the number of cells initially cryopreserved. **, $p < 0.01$ ($n = 3$ independent runs) for the comparison of both immediate viability and attachment efficiency. Data collected and analyzed by Jiang, B., and Li, W.

Because the aforementioned immediate (2 h) cell viability judged by the live/dead (green/red) staining assay is mainly a reflection of the cell membrane integrity, we further evaluate the cell viability (i.e., attachment efficiency) by determining the percentage of cells that can attach after culturing for 15 h post-thawing (**Fig. 3.8B)**. Overall, the hiPSC attachment efficiency is slightly lower than the cell viability assessed based on membrane integrity for all the conditions, suggesting some cells with good membrane integrity judged by the live/dead assay may not be able to attach and survive in long term. Furthermore, the hiPSC attachment efficiency follows the same trend as the immediate cell viability for the various conditions, and it is significantly and greatly higher for the condition of 5% DMSO and ice seeding than all the other conditions. Taken together, both the immediate (2 h) cell viability and long-term (15 h) cell viability (i.e., attachment efficiency) data show that 5% DMSO is critical but further increasing DMSO may not be sufficient to protect hiPSCs from cryoinjury during cryopreservation, which can be resolved by combining 5% DMSO with the sand-mediated ice seeding to significantly enhance the outcome of hiPSC cryopreservation.

3.2.4 High pluripotency and normal cell cycle of cryopreserved hiPSCs

The hiPSCs cryopreserved (cryo) using 5% DMSO and the sand-mediated ice seeding show typical colony morphology similar to that of fresh (control) hiPSCs under 2D monolayer culture (**Fig. 3.9A**). Furthermore, the cryopreserved hiPSCs are highly positive for pluripotency protein markers OCT-4 and SSEA-4, similar to that of the control group of fresh hiPSCs (**Fig. 3.9**). Flow cytometry analyses are used to quantitatively evaluate the expression of pluripotency markers OCT-4 and SSEA-4. As

shown in **Figure 3.9B-C**, the cryopreserved hiPSCs highly express the two protein markers OCT-4 (96.7 ± 2.3%) and SSEA-4 (96.1 ± 1.6%), similar to the control fresh hiPSCs (97.2 ± 1.4% positive on OCT-4 and 98.0 ± 1.0% positive on SSEA-4) with no statistically significant difference. Moreover, the distribution of cryopreserved hiPSCs in the G1, S, and G2/M phases of cell cycle is similar to that of the control fresh cells (**Fig. 3.9D-E**) with no statistically significant difference. Hence, the cryopreserved hiPSCs have similar proliferation capacity as the control fresh cells. In other words, these data show that the cryopreservation procedure with sand-mediated ice seeding and 5% DMSO has no evident impact on the pluripotency/stemness/self-renewal and the proliferation capacity of the hiPSCs.

4.2.5 Intact capacity of differentiation of the cryopreserved hiPSCs

To ascertain their functional survival, the cryopreserved hiPSCs are further assessed for their capacity of guided neural and cardiac differentiation *in vitro* and spontaneous teratoma formation *in vivo*. After 10 days of neural differentiation, the cryopreserved hiPSCs lose their typical colony morphology and neurites are observable to extend out of the differentiated cells (**Fig. 3.10A**), similar to the fresh control cells (**Fig. A2.1A**). Furthermore, the resultant cells are positive for neural specific marker TUJ-1: 95.9 ± 1.5% of the cryopreserved hiPSCs post neural differentiation are positive for TUJ-1, similar to that (94.7 ± 2.5%) of the fresh control hiPSCs (**Fig. A2.1B**). These data demonstrate the cryopreserved hiPSCs maintain their capacity of neural

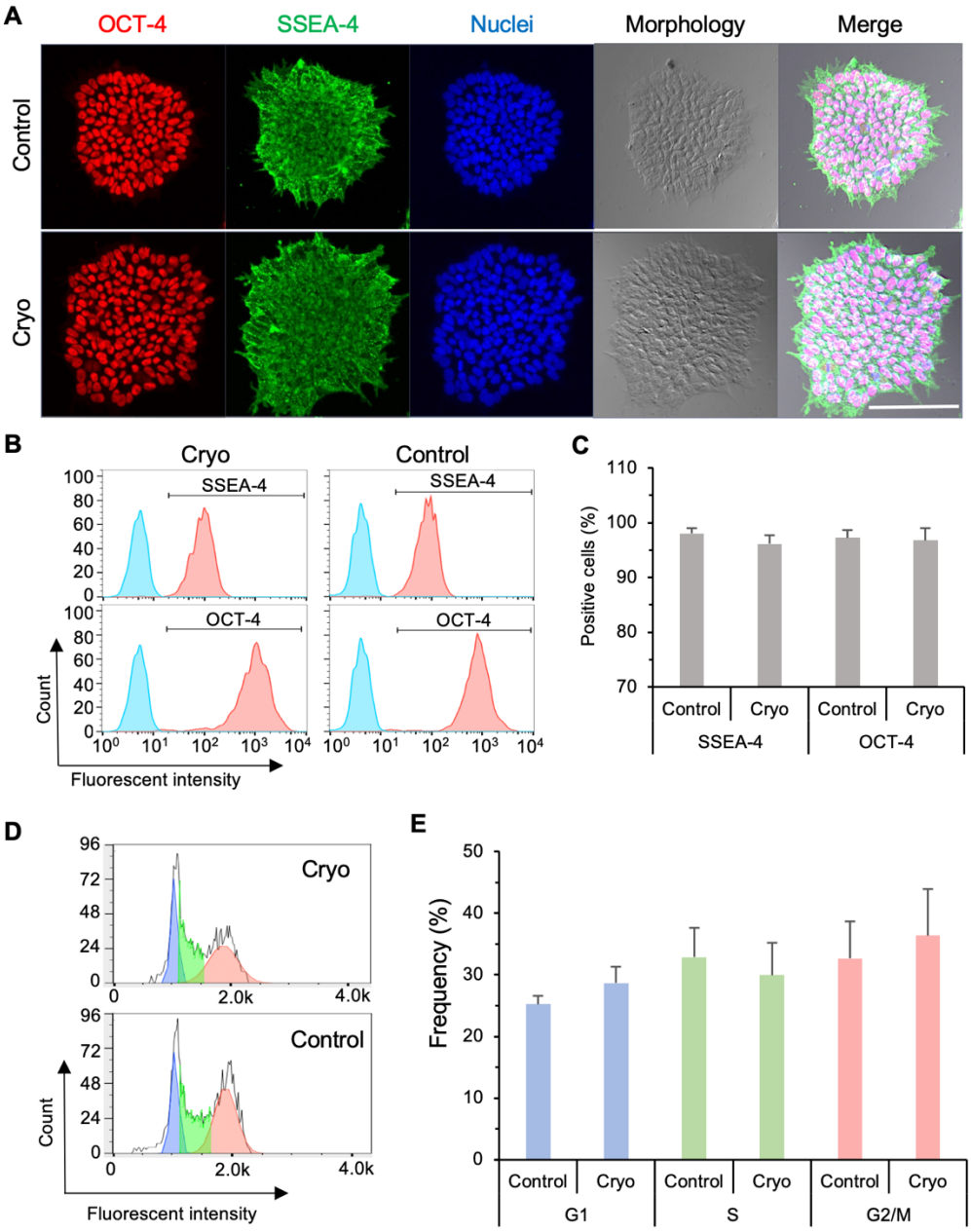

Figure 3.9 Cryopreservation with sand-mediated ice seeding and 5% DMSO does not significantly affect the hiPSC pluripotency and cell cycle. A, Images of cryopreserved (Cryo) hiPSCs showing typical colony morphology and high expression of pluripotency protein markers OCT-4 and SSEA-4, similar to fresh (Control) hiPSCs with no cryopreservation. Scale bar: 100 μm. **B–C**, Representative peaks (**B**) and quantitative data (**C**, $n = 3$ independent runs) form flow cytometry analyses, showing the cryopreserved hiPSCs highly express pluripotency protein markers SSEA-4 and OCT-4 similar to the fresh control hiPSCs with no statistically significant difference. The light blue peaks are isotype controls. **D–E**, Representative peaks (**D**) and quantitative data (**E**, $n = 3$ independent runs) from flow cytometry analyses, showing no statistically significant difference in the cell cycle distribution between the cryopreserved and fresh control hiPSCs. Data collected by Jiang, B.

differentiation. The capability of cardiac differentiation of the cryopreserved hiPSCs is also evidenced by the spontaneously beating areas observable in 10 days after initiation of the differentiation (**Movie 3.2**), similar to the areas seen in the fresh control cells (**Movie 3.3**). The percentage of cells on day 10 positive for the cardiac specific marker cTnT is not significantly different between the cryo (87.9 ± 2.6%) and fresh control (85.6 ± 4.8%) groups (**Fig. 3.10B**). The cardiac muscle-like striated pattern can be seen on both the cTnT-stained fluorescence images and the non-fluorescence images showing the cell morphology of both cryopreserved (**Fig. 3.10B**) and fresh control (**Fig. A2.1C**) hiPSCs-derived cardiomyocytes.

Lastly, the cryopreserved hiPSCs maintain the capability of teratoma formation *in vivo*. The teratomas (**Fig. 3.10C**) grown from the cryopreserved hiPSCs show typical tissue structure of the three germ layers [148, 149] (**Fig. 3.10C**): the neural epithelium of ectoderm with hypernucelated neuroectodermal structures, cartilage of mesoderm showing the nidus of cartilage with surrounding condensed mesenchymal cells, and gut epithelium of endoderm with subnuclear vacuoles and tube-like structure. Similar tissue structures are observable in the teratomas of the fresh control group (**Fig. A2.1D**). All these data on neural and cardiac differentiation in vitro and teratoma formation in vivo for the cryopreserved hiPSCs is similar to the that for the fresh hiPSCs with no cryopreservation, showing cryopreservation with 5% DMSO and the sand-mediated ice-seeding have no evident impact on the differentiation capacity of the hiPSCs.

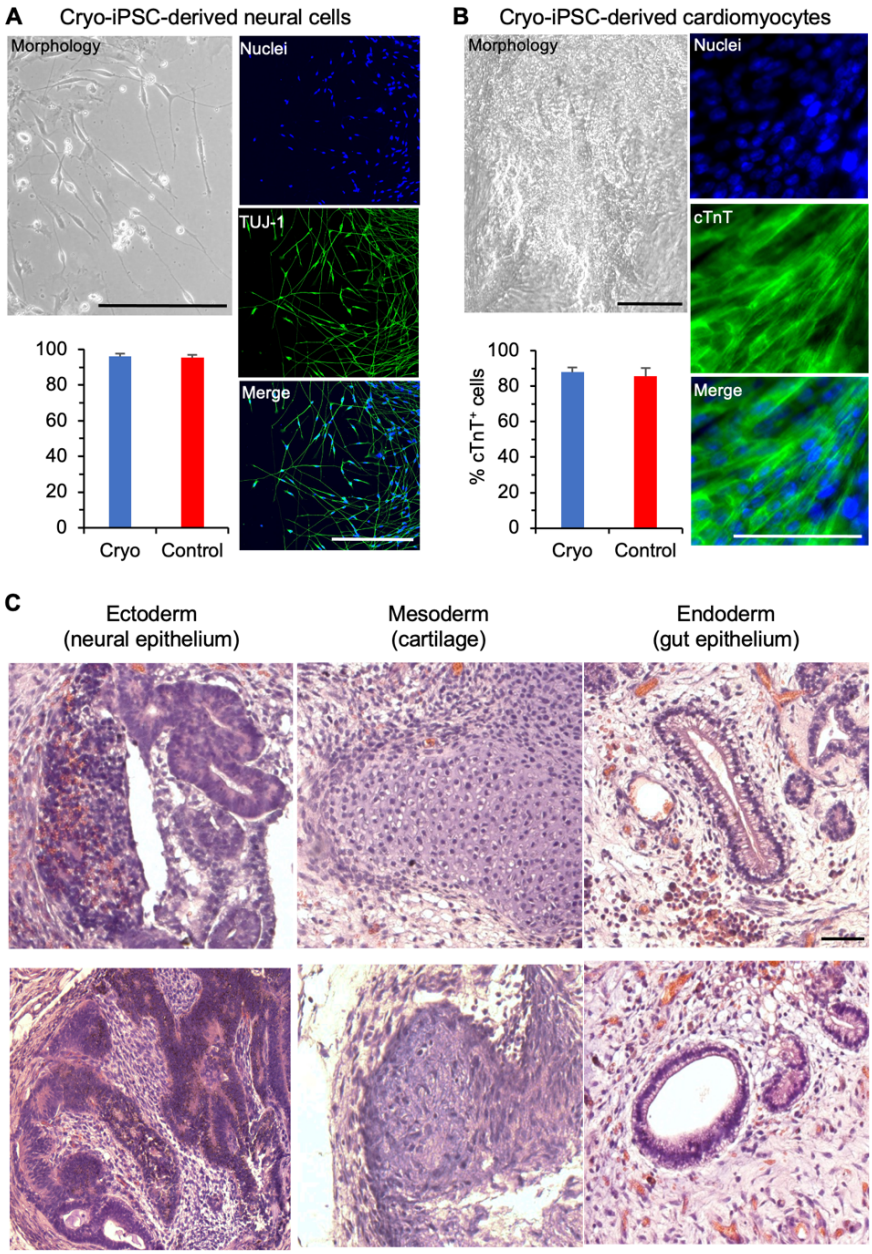

Figure 3.10 Cryopreservation with sand-mediated ice seeding and 5% DMSO does not significantly affect the differentiation capacity of the hiPSCs. **A**, The cryopreserved hiPSCs can efficiently differentiate into cells with typical neural cell morphology (neurites extending out of the cell body) and high expression of the neural specific marker TUJ-1. Cell nuclei are made visible by DAPI staining. **B**, The cryopreserved hiPSCs can efficiently differentiate into cells that highly express the cardiac specific markers cTnT. Cell nuclei are made visible by DAPI staining. **C**, The teratomas grown from the cryopreserved hiPSCs contain tissues from all the three germ layers including ectoderm (neural epithelium with hypernucelated neuroectodermal structures), mesoderm (the nidus of cartilage with surrounding condensed mesenchymal cells), and endoderm (gut epithelium with subnuclear vacuoles and tube-like structure). Scale bars: 100 μm. Data collected by Jiang, B.

3.3 Discussion

The cryopreservation of ovarian tissue is an essential technology for preserving a patient's fertility. While it is more common to cryopreserve sections of cortical tissue from the ovary and later transplant the cortical fragments [150], cryopreserving isolated preantral ovarian follicles offers distinct advantages over tissue. Because preantral ovarian follicles are small (typically less than 150 μm in diameter), the issue of CPA perfusion that causes impairment to larger tissues is mitigated [151]. Transplantation of cryopreserved ovarian tissue has also been shown to result in extensive follicle loss due to ischemia-reperfusion issues [66], which could be resolved by either grafting individual follicles in an artificial ovary environment [152, 153] or culturing and maturing follicles in vitro for in vitro fertilization [90]. In cases where malignant cells may be present in the vascularized ovarian tissue due to some types of cancer, cryopreservation of isolated follicles avoids the risk of re-introducing these malignant cells back into the patient during transplantation [154], as the follicles have their own basal membrane which prevents them from coming into contact and being infected with the malignant cells [155].

Current cryopreservation of ovarian tissue/follicles is done by one of two methods: vitrification or slow-freezing [156]. While vitrification is widely studied for oocytes [157] and has shown success for preantral ovarian follicle cryopreservation [158, 159], it typically requires a high concentration of toxic CPA to achieve ice-free cooling of the sample. Slow-freezing is more convenient and has been used to successfully cryopreserve preantral ovarian follicles with high survival/viability (~70%) [64, 70]. However, the slow-freezing protocol used in these studies required a

programmable-rate freezer to hold the sample at a high subzero temperature (above -10 °C) so that ice could be manually seeded in the sample by touching the cryovial with forceps (or presumably another metal tool) prechilled in LN2. Controlling the temperature of ice nucleation is critical for ovarian tissue samples [72, 160, 161]. Follicles cryopreserved here using sand-mediated ice nucleation at high subzero temperatures showed comparable immediate viability (77.3 ± 10.8 %) and long-term survival (58.4 ± 22.5 %) to these studies without the added cost of the programmable-rate freezer and the manual hassle of ice-seeding using similar concentration of CPA. The sand-PDMS film is simple and easy to add to the cryovial wall, allowing the use of a highly affordable device (Mr. Frosty^{TM}) for cooling in this cryopreservation procedure.

The difference in viability/survival of the tested conditions between the immediate viability experiment (2 h post-thaw) and the in vitro culture experiment (up to 9 days post-thaw) shows that immediate viability via live/dead staining is not sufficient for assessing the quality of cryopreserved follicles. Although the trends for both assessments are the same, with the fresh follicles and follicles cryopreserved with the sand-PDMS film outperforming the follicles cryopreserved without the sand-PDMS film, the values for the follicles cryopreserved without the sand-PDMS film are drastically different. Based on the live/dead staining quantification, a little over half (58.1 ± 16.4%) of the follicles cryopreserved without sand are viable, whereas only 13.8 ± 17.9% are able to survive and grow in culture. On the day of thawing, there is not a drastic difference in the morphology of follicles cryopreserved with or without the sand-PDMS film, as most appear round and intact with similar levels of

live and dead staining. However, the morphologies of the two groups greatly differ on day 1 of culture, as most of the follicles cryopreserved without the sand-PDMS film show clear evidence of cryodamage.

Human iPSCs can be derived from the somatic cells like skin fibroblasts and blood cells of a specific person (patient or healthy donor) and have the capability of self-renewal and differentiation into somatic cells of all three germ-layers [162]. This eliminates the ethical concern of embryonic stem cells. However, culturing hiPSCs at 37 °C is costly and their pluripotency and differentiation capability may decrease gradually over time during culture. Therefore, the quality of hiPSCs may be greatly compromised over long-term culture at 37 °C. As a result, efficient and convenient cryopreservation of hiPSCs to bank them in a state of "suspended animation" for their use at a desired future time is an enabling technology of the burgeoning hiPSC-based personalized medicine. However, the use of high concentrations of DMSO and serum in contemporary hiPSC cryopreservation protocols poses risks for the clinical use of the cryopreserved hiPSCs.

Current cryopreservation of hiPSCs utilizes two methods: vitrification and slow-freezing [163]. Although there is a higher survival for hiPSCs using vitrification than slow-freezing [164], vitrification requires high cooling rates achieved by specialized protocols/devices and/or high concentration of toxic CPA, making it difficult to scale-up for high-volume cell banking [165]. Slow-freezing is more convenient and widely used for cryopreservation of hiPSCs, with survival/recovery rates of ~50% [165-167]. This is similar to our control group (conventional method) shown in **Figure 3.8**. Cryopreservation of hiPSCs is notably more difficult than

cryopreservation of human adult stem cells (e.g., tissue-derived stem cells). Adult stem cells can be cryopreserved as single cells by traditional slow-freezing protocols with post-thaw viability up to 90% [168, 169]. However, hiPSCs are more sensitive to stresses during cell cryopreservation, as hiPSCs grow in colonies with cell-cell and cell-matrix interactions and may undergo anoikis-induced apoptosis when dissociated into single cells. Therefore, hiPSCs are usually cryopreserved as small clumps supplemented with RI and serum to enhance their survival [170].

It is worth noting that we did not remove DMSO from the sample immediately after thawing the sample. This avoids centrifuging and rinsing the hiPSCs that just suffer the stresses during thawing and may be susceptible to the stresses associated with centrifugation and washing for removing DMSO immediately after thawing. However, the 250 µL of cryopreserved sample with hiPSCs was transferred into 2 mL of medium immediately thawing and the 5% DMSO was diluted to 0.56%. Moreover, the DMSO-containing medium was replaced with DMSO-free medium after only 2 h of incubation at 37 °C for the cells to recover. This low DMSO concentration and short incubation time should be safe for cells, as shown by the high viability of the cells cryopreserved using 5% DMSO with sand-mediated ice seeding (**Fig. 3.8**). This is not surprising because most of chemicals used for hiPSC maintenance are dissolved in DMSO with a final concentration up to 0.6% in the maintenance medium for the hiPSCs [171, 172].

In this study, we used a natural and cost-effective material, sand, to seed/nucleate ice at high subzero temperature during cooling hiPSCs and preantral ovarian follicles for cryopreservation with good outcome and reproducibility. The sands used in this study did not require any material or surface modification in order to

achieve ice nucleation, making them convenient and cost-effective to use. Additionally, the amount of sand embedded onto the PDMS film was sufficient to achieve consistent ice nucleation at high subzero temperatures, as evidenced by the small standard deviation and consistent ice-seeding temperature measured in **Figure 3.2**. This allows serum-free cryopreservation of hiPSCs with high viability and quality at a much reduced (half) DMSO concentration, as well as cryopreservation of ovarian follicles with high viability and growth capacity. The ice-seeding temperature of the cryopreservation solution containing the sand-PDMS film is significantly higher than that of the cryopreservation solution containing a pure PDMS film with no sand, which indicates that the sand plays an important role in seeding ice in the sample during cryopreservation. This is consistent with the literature that quartz along with a few other minerals can seed ice in the atmosphere [173-175], because sands consist mainly of crystalline silica (silicon dioxide) that is also the material in quartz.

Our studies show that controlled ice nucleation catalyzed by the sands greatly improves hiPSC survival post cryopreservation, from 52.6 ± 3.5% (5% DMSO, no ice seeding) to 90.3 ± 2.5% (5% DMSO, with ice seeding). This increase in survival is similar to other studies regarding the impact of controlled ice nucleation on cell survival using a slow-freezing protocol [72]. Other types of cells susceptible to freezing-induced stresses show a 15-40% increase in survival post-cryopreservation with ice nucleation versus without [72].

Of note, various methods have been explored to improve cryopreservation outcome including microencapsulation of cells in alginate hydrogel [131, 176], nano-warming with magnetic nanoparticles [177-180], supplement of nontoxic CPAs like

sugars into the cryopreservation medium [181-184], and intracellular delivery of the sugar using cold-responsive nanoparticles [169]. Techniques for intracellular delivery of a widely studied sugar, trehalose, into mammalian cells for cell banking are reviewed in **Appendix 3**. All these methods may be combined with our sand-mediated ice-seeding, which has the potential to further reduce or even eliminate the DMSO needed for cryopreservation of the hiPSCs and ovarian follicles with high functional survival. Lastly, the method developed may be applied to cryopreserve the iPSCs and ovarian follicles of non-human endangered species with high functional survival, which is valuable for animal species conservation [185].

3.4 Conclusions

We developed a novel method which uses sand as the ice-seeding material for cryopreservation of ovarian follicles and hiPSCs, The cryopreserved ovarian follicles show high immediate viability and can grow during in vitro culture. The cryopreserved hiPSCs can attach well and maintain high pluripotency and differentiation capacity in vitro and in vivo. This method is simple to use, cost effective, and can be applied to cells and microtissues. The sand mediated ice-seeding method has the potential to be widely used for cryopreservation of ovarian follicles, hiPSCs, and potentially many other types of human cells and tissues. Using sand as an ice nucleator can eliminate the need for costly programmable-rate freezers and highly user-dependent manual ice seeding, making slow-freezing an attractive and reliable method for preserving both ovarian follicles as an alternative for preserving fertility and hiPSCs to facilitate cell-based medicine.

3.5 Materials and Methods

3.5.1 hiPSC Cell Culture

The DF19-9-11T.H and IMR90-1 hiPSC lines were purchased from WiCell (Madison, WI, USA). The cells were cultured in StemFlex medium (ThermoFisher, Gaithersburg, MD, USA) on Matrigel (Corning, NY, USA)-coated plates in a 37 °C 5% CO_2 incubator. The cells were passaged at a ratio between 1:4 and 1:5 twice a week. Versene (Gibco, Gaithersburg, MD, USA) which contains 0.48 nM ethylenediaminetetraacetic acid (EDTA) in phosphate buffered saline (PBS) was used to detach the cells at 37 °C for 2 min for passaging or further uses.

3.5.2 Isolation of ovarian follicles

Ovaries were obtained from 3 to 8-week-old C57BL/6 mice (The Jackson Laboratory, Bar Harbor, ME, USA). All animal procedures and studies were approved by the Institutional Animal Care and Use Committee (IACUC) at the University of Maryland, College Park, MD. Preantral secondary follicles (100 – 150 μm in diameter) were isolated from ovaries using a cell dissociation sieve (Sigma-Aldrich) that was first proposed for follicle isolation from domestic cat ovaries [186] and has more recently been shown to yield similar results to mechanical isolation via syringes for mouse follicle isolation [187]. Briefly, ovaries were placed on the metal mesh of the cell dissociation sieve and gently ground using the accompanying glass pestle over top follicle dissection medium (L15 supplemented with 1% penicillin/streptomycin and 1% FBS) on a heated stage (37 °C). Size 60 mesh (Sigma-Aldrich) was used for the procedure (wire diameter: 0.254 mm; opening size:

380 μm). This procedure takes less than 10 minutes to homogenize the tissue and release preantral ovarian follicles. Follicles were manually selected under a stereomicroscope and transferred to fresh, pre-warmed follicle dissection medium for washing. Follicles were then transferred to recovery media ($\boldsymbol{\alpha}$MEM supplemented with 1% penicillin/streptomycin and 10% FBS) and allowed to recover in a 37 °C incubator for 2 h before further experiments.

3.5.3 Fabrication of sand-PDMS film for cryopreservation

Sands were purchased from Walmart (Landover Hills, MD, USA) and were rinsed under running tap water overnight in a 100-mL beaker (with agitation by a glass stir bar for 10 min at the beginning). The sand was then washed twice with 50 mL of deionized water. Afterwards, the sand samples were autoclaved at 121 °C for 30 min and baked in a 75 °C oven for 6 h to dry. Polydimethylsiloxane (PDMS, Dow SYLGARD 184 Silicone Encapsulant, Dow, Midland, MI, USA) prepolymer was mixed with its curing agent at a weight ratio of 10: 0.5 (prepolymer: curing agent). The mixture (1 mL) was poured onto a microscope glass slide (75 × 26 × 1 mm) and air bubbles were removed under vacuum for 20 min. Afterwards, the PDMS was cured by baking in a 75 °C oven for 2 h. Uncured PDMS mixture (50 μL) was then evenly spread with the aid of a pipette tip on top of the cured PDMS on the glass slide to form a sticky fluid layer. Afterwards, the dry sands were sifted through a mesh strainer (opening size: 200 μm) at ~5 cm above to drop and partially embed the sands in the uncured PDMS sticky fluid layer. The slide with PDMS and sand was further baked in the oven at 75 °C for 30 min. The cured sand-PDMS film was gently peeled off from the slide with the help of a blade and then cut into pieces of 3 mm × 5 mm (width x length). Finally,

each of the sand-PDMS pieces was attached to the inside wall of a cryovial and the sand-PDMS piece containing cryovials were autoclaved at 121 °C for 30 min before their use to hold hiPSC sample for cryopreservation.

For making the plastic shard-PDMS film, plastic shards were scratched off a polystyrene cell culture plate (ThermoFisher) using a single edge razor blade onto the uncured PDMS sticky layer (with all other steps being the same as that for making the sand-PDMS film). Glass beads of 40–70 μm in size were purchased from Microspheres-Nanopheres (C-PGL-07, Microspheres-Nanospheres, NY, USA). The glass beads were partially embedded in the PDMS film following the same procedure for making sand-PDMS film.

3.5.4 Surface characterization of the sand-PDMS film

For the scanning electron microscopy (SEM) imaging, the sand-PDMS films were cut into small pieces of 1 cm^2 and attached on the SEM sample holder. The samples were sputter-coated with gold using a Cressington (Watford, UK) 108 sputter coater for 2 min at 15 mA. Afterwards, the samples were imaged with a Hitachi (Tokyo, Japan) SU-70 FEG scanning electron microscope at 5.0 kV. Energy dispersive x-ray spectroscopy (EDXS, Hitachi SU-70 FEG SEM, Tokyo, Japan) was used for elemental analysis of the surface of the plain PDMS and sand-PDMS films. The plain PDMS film was prepared in the same way as that for preparing the sand-PDMS films except that no sand was plated.

For quantifying the size of sand particles before and after sifting, brightfield microscopy images of sand particles partially embedded in the PDMS film without and with sifting through the mesh strainer were analyzed using Image J (version 1.47) to

measure the area of sand particles on the film. Images from 10 random areas of the film containing a total of 65 sand particles were analyzed for both conditions (i.e., without and with sifting through the mesh strainer).

3.5.5 Measurement of ice-seeding temperature

To measure the ice-seeding temperature, a piece of sand-PDMS film was attached to the inside wall of a 2-mL glass vial, followed by adding 500 μl of deionized water. The ice-seeding temperatures of water in the same glass vials containing either a PDMS-film without sand or no film at all were studied as controls. A K-type thermocouple (Omega, Norwalk, CT, USA, 0.05 inch in diameter) was then placed in water in the glass vial. The vials were placed onto the shelf of a SP Virtis AdVantage Pro benchtop lyophilizer (SP, Warminster, PA, USA) and cooled to 4 °C. Then the sample was cooled to −25 °C with a 25-min ramp time. The thermocouple was connected to a Keysight Technologies (Santa Rosa, CA, USA) 34970A Data Acquisition/Data Logger Switch Unit to record the temperature over time. The temperature at the time when there was a sudden increase in temperature due to the latent heat release associated with ice formation during the cooling process, was recorded as the ice-seeding temperature. Ice-seeding temperatures of the plastic shard- and glass bead-PDMS films were measured in the same way.

3.5.6 Cryomicroscopy study of sand-mediated ice formation

Cryomicroscopy was conducted using a Linkam FDCS196 (Tadworth, UK) freeze-drying stage mounted on a Zeiss (Oberkochen, Germany) A1 Axio Scope, for which a drop (200 μL) of the cryopreservation solution made of the mTeSR medium

(STEMCELL Technologies, Vancouver, Canada) supplemented with 5% DMSO, and sands were added in the sample holder at room temperature. The sample holder with the sands immersed in the solution was then loaded into the freeze-drying stage for controlled cooling at 1 °C min^{-1} to −20 °C. Real-time images were captured with a FLIR (Wilsonville, OR, USA) Grasshopper 3 color camera every 0.5 s.

3.5.7 Cryopreservation of hiPSCs and ovarian follicles

The cryopreservation of hiPSCs was performed using a slow-freezing procedure with a Mr. Frosty™ Freezing Container filled with isopropyl alcohol (Sigma Aldrich), which has a cooling rate of approximately −1 °C min^{-1} [81, 188]. The hiPSCs at 80% confluence were detached using Versene and suspended in pre-cooled cryopreservation solution. For the conventional method, the cryopreservation solution was made up of 10% FBS and 10% DMSO in the mTeSR medium. For the experimental cryopreservation solution, it contained 0–5% DMSO in the mTeSR medium with no FBS. All cryopreservation solutions and the Mr. Frosty™ Freezing Container were pre-cooled at 4 °C for 30 min before use. The concentration of hiPSCs for cryopreservation was 1×10^7 cells mL^{-1} and each cryovial was loaded with 250 µL of the cell suspension. Experimental conditions with sand-mediated ice seeding had one sand-PDMS film attached to the inside wall of the cryovial, with the sand surface being exposed to the cell suspension. The cryovials were loaded in the Mr. Frosty™ Freezing Container and stored in a −80 °C refrigerator overnight. Then, the cryovials with hiPSCs were transferred into the LN2 for long-term storage (2–5 weeks).

Preantral ovarian follicles were cryopreserved using the same slow-freezing procedure with a Mr. Frosty™ Freezing container. Isolated follicles were transferred

into pre-cooled (4 °C) cryopreservation solution and allowed to equilibrate for 30 min on ice. Then, follicles (approximately 10-20 per experimental group) were transferred into 1 mL of fresh pre-cooled cryopreservation solution in a cryovial either with (n=159) or without (n=157) a sand-PDMS film. The cryovials were placed into the Mr. Frosty™ and stored in a -80 °C refrigerator overnight. Then, the cryovials were transferred into LN2 for long term storage (1-4 weeks). Freshly isolated follicles were examined as a positive control (n=121).

To thaw the frozen samples with hiPSCs, 2 mL of mTeSR medium with 10 μM ROCK inhibitor (RI, Y-27632, Sigma Aldrich) was added to each well (Matrigel coated) of a 6-well plate and pre-warmed in the incubator at 37 °C for at least 20 min. The cryovial was removed from the LN2 tank and rapidly warmed in a 37 °C water bath for ~30 s. The cell suspension in the cryovial was then transferred into the pre-warmed medium in the 6-well plate for further incubation and studies. DMSO was not removed immediately after thawing to avoid centrifuging and washing the hiPSCs. The cells were cultured in the 6-well plate with medium containing a final DMSO concentration of 0.56% (250 μL cell suspension containing 5% DMSO diluted in 2 mL medium). After 2 h, the DMSO-containing medium was replaced with pre-warmed DMSO-free medium.

To thaw the ovarian follicles, the cryovials containing follicles were removed from LN2 storage and warmed by plunging into a 37 °C water bath with gentle shaking until the sample was completely thawed. The cryopreservation solution was diluted in a stepwise matter to minimize cell damage and preserve cell function [70]: Follicles were transferred into a 35 mm Petri dish with 3 mL of L15 medium

supplemented with: (1) 1 M DMSO + 0.1 M sucrose + 10% FBS for 10 minutes; (2) 0.5 M DMSO + 0.1 sucrose + 10% FBS for 10 minutes, (3) 0.1 M sucrose + 10% FBS for 10 minutes; (4) 10% FBS for 5 minutes. Follicles were then transferred into recovery media (αMEM + 1% penicillin/streptomycin + 1% FBS) and incubated at 37 °C with 5% CO_2 for 2 h before further use.

3.5.8 Live/dead assay and cell attachment efficiency

To quantify their viability, the hiPSCs and ovarian follicles after thawing were cultured for 2 h and then stained with calcein AM and propidium iodide (PI) to visualize live (green with no red stain) and dead (red stain) cells, respectively, according to the instructions of the manufacturer (ThermoFisher). The two dyes were added into 1 mL of DMEM/F12 (1 μM for calcein AM and 1 μg mL^{-1} for PI) for incubating with the cells for 5 min and 15 min at 37 °C for hiPSCs and follicles, respectively. Afterwards, green and red fluorescence images of the samples were taken using a Zeiss (Oberkochen, Germany) LSM710 microscope to count the live and dead cells. hiPSC cell viability is calculated as the percentage of live cells out of the total (i.e., live and dead) cells. For ovarian follicle immediate viability, the green (live) and dead (red) areas were measured as a percentage of the total area of the follicle taken from the morphology image. The viable area of the follicle was calculated as the red area percentage subtracted from 100%, unless the green area was less than this value, then the green area percentage was used as the viable area value. In other words, the viable follicle area was the follicle area that had esterase activity measured by the calcein AM and no damage measured by the PI. Immediate cell

viability is calculated as the percentage of follicles with a viable follicle area (green stain only, not overlapping with red stain) greater than 70% of the total follicle area.

To quantify the cell attachment efficiency for studying the capability of the hiPSCs in attaching on culture dish, the mTeSR medium containing ROCK inhibitor was replaced with fresh mTeSR without ROCK inhibitor after 2 h of post-thawing incubation. After 15 h of culture, the hiPSCs were detached and the cell number was counted. The cell attachment efficiency was calculated as the percentage of the cell number post-cryopreservation and 15 h of culture out of the cell number used for cryopreservation in the cryovial.

3.5.9 Teratoma assay for hiPSCs

For the teratoma assay, hiPSCs at a confluence of 80% were detached and suspended at 3×10^7 cells mL−1 in 1 mL of 1x PBS and then mixed with 500 μL of Matrigel (Corning). The cell suspension was kept on ice and then injected subcutaneously (s.c.) into the dorsal rear flank of non-obese diabetic/severe combined immunodeficiency mice (NOD.CB17-scid, Charles River, Frederick, MD, USA). Each mouse was injected with 250 μL of the cell suspension and 5 mice (age: 5 weeks) were used for each experimental group. After 5 weeks, the mice were sacrificed and teratomas (n = 5 for each group) were collected. The samples were fixed in 4% paraformaldehyde (PFA) in 1 x PBS for 2 days. Afterwards, the samples were trimmed and embedded in paraffin for sectioning into slices of 5 μm in thickness. The slices were than stained with hematoxylin and eosin (H&E) and imaged with a Zeiss LSM710 microscope. All animal studies were approved by the Institutional Animal Care and Use Committee (IACUC) at the University of Maryland, College Park, MD.

3.5.10 Neural and cardiac differentiation of hiPSCs

Neural differentiation was carried out by following previously reported studies [189-191]. Briefly, the hiPSCs were detached and suspended in mTeSR medium at 1×10^6 cells mL^{-1}. The samples were passed through a 70 μm cell strainer (Gibco). The resultant hiPSC samples were cultured in mTeSR with 10 μM ROCK inhibitor (Y-27632) for 2 days. Afterwards, the medium was replaced with a neural differentiation medium and the cells were further cultured for 10 days with medium being changed every other day. The neural differentiation medium was a mixture of DMEM/F12 and neural basal medium (Gibco) (1:1 in volume) supplemented with 1x N2 (Gibco), 1x B27 (Gibco), 1% minimum essential medium non-essential amino acids (MEM NEAA, Gibco), and 1% l-glutamine (Invitrogen, Carlsbad, CA, USA). Lastly, the cells on day 10 post-initiation of neural differentiation were fixed with 4% PFA for further immunostaining and analysis.

Cardiac differentiation was conducted also by following previous studies [192, 193]. The basal medium used for cardiac differentiation was a mixture of DMEM/F12 and α-MEM (ThermoFisher) (1:1 in volume) supplemented with 2% Knockout Serum Replacement (KOSR, Gibco), 1 mM l-glutamine, 1% MEM NEAA, and 0.1 mM β-mercaptoethanol (Sigma Aldrich). For cardiac differentiation, hiPSCs were grown in 6-well plate coated with Matrigel. At 80% confluency, the hiPSCs were cultured with the mesoderm induction medium for 2 days. Then, the medium was replaced with the cardiac induction medium for the following 8 days. Medium change was performed every other day. The mesoderm induction medium was made by supplementing 5 μM CHIR99021 (ThermoFisher) and 2 μM GSK inhibitor 6-bromoindirubin-3′-oxime

(BIO, ThermoFisher) in the basal medium. The cardiac induction medium was made by supplementing 10 μM KY02111 (ThermoFisher) and 10 μM XAV939 (ThermoFisher in the basal medium. Spontaneous beating areas in the sample were recorded using a Zeiss LSM710 microscope. The cells on day 10 post cardiac differentiation were fixed with 4% PFA for further immunostaining and analysis.

3.5.11 Flow cytometry analysis of protein marker expression of hiPSCs

For flow cytometry studies of protein marker expression, cells were dissociated into single cells by incubating them with 0.25% trypsin (Gibco) for 5 min at 37 °C and washed with 1x PBS twice. The dissociated cells were fixed with 75% ethanol at 4 °C overnight. Then, the cells were permeabilized with 0.05% Triton X-100 for 3 min and rinsed with 1x PBS twice. The cell number was adjusted to 1×10^6 cells per tube in 700 μL of 1x PBS for each protein marker. The cells were incubated with primary antibodies including: OCT-4 (1:500 dilution, Cell Signaling Technologies), SSEA-4 (1:500 dilution, Cell Signaling Technologies), TUJ-1 (1:500; R&D Systems, Minneapolis, MN, USA), or cTnT (1:500 dilution, Cell Signaling Technologies) at 4 °C overnight. Afterwards, the samples were rinsed with 1x PBS thrice before incubation with secondary antibodies (goat anti-mouse IgG FITC and goat anti-rabbit IgG PE, Invitrogen) at 1:1000 dilution for 1 h at RT. The samples were then washed with 1x PBS twice before analysis using a BD FACSCelesta (Franklin Lakes, NJ, USA) flow cytometer. The cells incubated with secondary antibody but no primary antibodies were processed and washed in the same way for analysis to serve as the negative/isotype control. The resultant data was analyzed with the BD Flowjo software (v10).

3.5.12 Cell cycle analysis of hiPSCs

For cell cycle analysis, the cells fixed as aforementioned for protein marker expression studies were treated with RNase from bovine pancreas (1 μg mL^{-1}, ThermoFisher) for 5 min at RT. Then, the cells were stained with PI (1 μg mL^{-1}, ThermoFisher) for 5 min at RT and rinsed with 1x PBS twice. Afterwards, the cell concentration was adjusted to 1×10^6 cells per tube in 700 μL of 1x PBS for analysis using a BD FACSCelesta flow cytometer. The resultant data was analyzed with the built-in cell cycle analysis function of the BD Flowjo software (v10).

3.5.13 In vitro culture of ovarian follicles

For in vitro culture of follicles, they were encapsulated in 0.25% alginate (w/v) beads using a pipette droplet method as previously reported [194, 195]. The 0.25% alginate solution was composed of PRONOVA UP MVG sodium alginate (NovaMatrix, Sandvika, Norway) dissolved in a 25 mM D-mannitol and 10 mM HEPES solution, and sterile-filtered through a 0.22 μm filter. Follicles were first transferred via pipette into a ~50 μL alginate solution droplet for washing. Then, follicles were transferred via pipette to a fresh ~50 μL alginate solution droplet. A small volume pipette (10 μL) was used to form 5 μL alginate droplets containing one follicle each. The pipette was used to take up ~2.5 μL alginate, then the follicle, then the rest of the ~2.5 μL alginate so that the follicle was close to the center of the bead. This 5 μL alginate droplet containing one follicle was ejected into a crosslinking solution consisting of 50 mM $CaCl_2$ and 140 mM NaCl [194]. The alginate beads were crosslinked in the crosslinking solution for 2 minutes and then transferred to recovery medium for washing. Then, the follicle-laden alginate beads were transferred to a 96-

well plate, with each well containing one follicle-laden alginate bead and 150 μL of follicle culture media was added to each well. Follicle culture medium consisted of αMEM supplemented with 1X insulin transferrin selenium (ITS) solution (Sigma-Aldrich), 1% L-glutamine, 1% penicillin/streptomycin, 10% FBS, and 100 mIU/mL follicle stimulating hormone (FSH, Sigma-Aldrich). Follicles were cultured at 37 °C with 5% CO_2 for 9 days. The day of alginate encapsulation was considered day 1 Every other day, 75 μL of the follicle culture medium was manually replaced with fresh media.

Using a Zeiss LSM710 microscope, follicles were imaged on days 1, 3, 5, 7, and 9. Follicle diameters were measured using ImageJ (1.52q, US National Institutes of Health, Bethesda, MD). To account for varying follicle shapes (e.g., spheroidal) two measurements were averaged to give the reported follicle diameter, with one measurement at the widest length of the follicle and the other perpendicular to it across the follicle. Growth was assessed by the change in the follicle diameter, D/D1, which is the follicle diameter over the initial follicle diameter on day 1. Follicles with a D/D1 greater than 1 on Day 9 were characterized as growing, surviving follicles for quantifying long-term survival. A D/D1 less than 1 signaled that a follicle that was dying, degenerating, and shrinking.

3.5.14 Statistical analysis

All graphing and statistical analyses were performed using Prism 8 (GraphPad Software, San Diego, CA, USA). Data are reported as the mean ± standard deviation from at least three independent runs. If not specifically mentioned in the figure caption, Student's two-tailed unpaired *t*-tests assuming equal variance were performed with no

outliers excluded for comparison between groups. For comparisons between multiple follicle groups with one independent variable, a one-way analysis of variance (ANOVA) followed by a Tukey *post hoc* correction was performed. For comparison between multiple follicles groups with two independent variables, two-way ANOVA with Sidak's post-test and correction was used. The differences were considered statistically significant when the p value was less than 0.05 (* $p < 0.05$, ** $p < 0.01$, *** $p < 0.001$)

Acknowledgments

This work was partially supported by the National Science Foundation under grant CBET-1831019, the National Science Foundation Graduate Research Fellowship Program (NSF GRFP) under Grant No. DGE 1840340, and by National Institutes of Health (NIH) under grant No. R01EB023632.

Chapter 4 : Conclusions

In this dissertation, we developed multiscale technologies to engineer and cryopreserve ovarian follicles and hiPSCs for the advancement of fertility preservation/restoration and endocrine dysfunction treatments. To gain a deeper understanding of the micromechanical environment of the ovary to establish design criteria for ovarian tissue engineering models, we investigate the mechanical properties and ECM distribution of ovarian tissue from reproductively younger and older domestic cats. We reveal spatial heterogeneities in both elastic and viscoelastic properties, and link these to distribution of HA in the tissue. Using stress relaxation testing via AFM indentation and viscoelastic modeling, we are able to distinguish between elastic and viscoelastic components of material behavior, allowing us to characterize the true elastic modulus of the tissue. We also leverage a natural biomaterial, sand, to create a cryopreservation protocol for enhancing the long-term storage of ovarian follicles and hiPSCs. The ice-nucleating capability of the sand improves cryopreservation outcomes for the cells and microtissues, and shows great promise for combining with other cryopreservation technologies for the reduction/elimination of organic solvent-based CPAs. These findings can inform future ovarian tissue engineering models and cryopreservation strategies for treating ovarian dysregulation and its negative effects.

Chapter 5 : Future Research Directions

5.1 Impact of viscoelasticity on follicle growth and development

Chapter 2 investigated the micromechanical properties of ovarian tissue obtained from the domestic cat, with special focus on how mechanical properties may differ between the cortex and medulla regions. This work showed differences in apparent elastic modulus between the cortex and medulla for all reproductive ages tested, but more importantly showed differences in viscoelasticity, a much more biologically relevant material property, between the cortex and medulla for only reproductively mature cats.

Previous work has shown that modulus heterogeneity greatly impacts follicle culture [34], but no study has been done regarding the impact of the heterogeneity of the viscoelastic property on follicle development. Mounting evidence has underscored the need for biomaterials design that mimics not only the elastic modulus of the native tissue environment, but also the dynamic, time-dependent behavior of the tissue [41]. The mechanical property data, both the elastic and viscoelastic, properties can be further used as design criteria to create biomimetic culture conditions and study the effect of viscoelasticity on follicle growth and development. The mechanical characterization insights provided in **Chapter 2** strongly suggest that in vitro systems for ovarian follicle culture must consider the viscoelastic properties, especially viscoelastic heterogeneity, in the system design.

Core-shell microcapsules can be fabricated to mimic the medulla and cortex, respectively, to encapsulate preantral follicles for 3D in vitro culture [34]. Based on the

information presented in **Chapter 2**, the core could contain collagen type I, and the shell could be comprised of collagen type I and hyaluronic acid, following the distribution of ECM across the medulla and cortex. Alginate, an excellent biomaterial for follicle encapsulation and culture [194, 196-198], could also be incorporated in the core and/or shell composition to tune the viscoelastic properties [110], to match with the values found in **Chapter 2**. The elastic and viscoelastic properties of the core and shell hydrogel materials can easily be tested using the AFM workflow developed in **Chapter 2** to mimic the micromechanical differences between the cortex and medulla.

5.2 Combining cryopreservation technologies with the sand-PDMS film

A sand-PDMS film was used to enhance cryopreservation of preantral ovarian follicles and hiPSCs by nucleating ice at high subzero temperatures in **Chapter 3**. For hiPSCs, this technology halved the necessary amount of DMSO for cryoprotection and eliminated the need for serum in the cryopreservation solution. For ovarian follicles, this technology greatly increased viability and post-thaw growth, but still used 10% DMSO and serum in the cryopreservation solution. For maximum clinical effectiveness and translatability of this technology, ideally organic solvent CPAs like DMSO would be removed totally from the cryopreservation solution to avoid the need for washing and losing the precious cells and the risk of long-term alteration of the cells by the potentially toxic agent [77, 199].

To enhance cryopreservation outcomes and eliminate toxic CPAs, this technology can be easily combined with other cryopreservation technologies. Microencapsulation of cells in alginate has been shown to improve cryopreservation outcomes, enabling low-CPA cryopreservation of cells [200]. Alginate encapsulation

of hiPSCs and ovarian follicles before freezing with the sand-PDMS film could prove the right combination to further reduce or possibly eliminate the DMSO used in the cryopreservation solution.

Additionally, nontoxic CPAs, like trehalose, can be investigated to replace DMSO. Previously, microinjection of trehalose into oocytes protected them from freeze-associates stresses during slow-cooling down to -60 °C [201]. Trehalose delivered intracellularly via cold-responsive nanoparticles protected human adipose stem cells (hADSCs) during slow-freezing cryopreservation just as well as 10% DMSO did [169], demonstrating that trehalose can be used as the sole cryoprotectant for stem cells and perform just as well as DMSO. Cold-responsive nanoparticle-mediated delivery of trehalose into preantral follicles and hiPSCs could be combined with the sand-PDMS film technique to further enhance cryopreservation outcomes.

Publications, and Conference Presentations, and Book Chapters

Peer-reviewed Journal Publications:

- **Stewart, S.,** Ou, W., Aranda-Espinoza H., Rahaman S., He, X. Micromechanical characterizations and viscoelastic modeling reveal elastic and viscoelastic heterogeneities in ovarian tissue and the significant viscoelastic contribution to the apparent elastic modulus determined by AFM indentation. *Acta Biomaterialia.* 2023
- Jiang, B*., Li, W.*, **Stewart, S**.*, Ou, W., Liu, B., Comizzoli, P., and He, X. Sand-mediated ice seeding enables serum-free low-cryoprotectant cryopreservation of human induced pluripotent stem cells. ***Bioactive Materials.*** 2021. *denotes equal contribution
- **Stewart, S.,** Arminan, A., He, X. Perspective: Nanoparticle-mediated delivery of cryoprotectants for cryopreservation. *CryoLetters.* 2020.
- **Stewart, S.,** and He, X. Intracellular Delivery of Trehalose for Cell Banking. *Langmuir*. 2018.
- Lee, P.C., **Stewart, S.,** Amelkina, O., Sylvester, H., He, X., Comizzoli, P. Trehalose delivered by cold-responsive nanoparticles improves tolerance of cumulus-oocyte complexes to microwave drying. *Journal of Assisted Reproduction and Genetics*. 2023.
- Ou, W., **Stewart, S.,** White, A., Kwizera, E., Xu, J., Fang, Y., Shamul, J.. Xie, C., Nurudeen, S., Tirada, N., Lu, X., Tkaczuk, K., He, X. In-situ cryo-immune engineering of tumor microenvironment with cold-responsive nanotechnology for cancer immunotherapy. *Nature Communications*. 2023.

- Levy, D., Jeyaram A., Born, L., Chang, K., Abadchi, S., Hsu, A., Solomon, T., Aranda, A., **Stewart, S.,** He, X., Harmon, J., Jay, S. Impact of storage conditions and duration on function of native and cargo-loaded mesenchymal stromal cell extracellular vesicles. *Cytotherapy.* 2022.
- Jiang, B., White, A., Ou, W., Van Belleghem, S., **Stewart, S**., Shamul, J.G., Rahaman, S.O., Fisher, J.P., and He, X. Noncovalent reversible binding-enabled facile fabrication of leak-free PDMS microfluidic devices without plasma treatment for convenient cell loading and retrieval. *Bioactive Materials.* 2022.
- Kwizera, E.A., Ou, W., Lee, S., **Stewart, S**., Shamul, J.G., Xu, J., Tait, N., Tkaczuk, K., He, X. Greatly enhanced CTC culture enabled by capturing CTC heterogeneity using a PEGylated PDMS-titanium-gold electromicrofluidic device with glutathione-controlled gentle cell release. *ACS Nano.* 2022.
- Xu, J., Liu, Y., Sheng, L., Ou, W., White, A., **Stewart, S.,** Tkaczuk, K., Ellis, L., Wan, J., Lu, X., He, X. Metaformin bicarbonate-mediated efficient RNAi for precise targeting of TP53 deficiency in colon and rectal cancers. *Nano Today.* 2022.
- Kwizera, EA, **Stewart, S.,** Mahmud, MM, He, X. Magnetic Nanoparticle-Mediated Heating for Biomedical Applications. *Journal of Heat Transfer*. 2022.
- Jiang, B., Ou, W., Shamul, J.G., Chen, H., Van Belleghem, S., **Stewart, S.,** Liu, Z., Fisher, J.P., and He, X. Rock inhibitor may compromise human

induced pluripotent stem cells for cardiac differentiation in 3D. *Bioactive Materials.* 2021.

- Wang, H., Liang, Y., Yin, Y., Zhang, J., Su, W., White, A.M., Jiang, B., Zhang, Y., **Stewart, S.,** Lu, X., and He, X. Carbon nano-onion-mediated dual targeting of P-selectin and P-glycoprotein to overcome cancer drug resistance. *Nature Communications.* 2021.
- Wang, H., Agarwal, P., Jiang, B., **Stewart, S**., Liu, X., Liang, Y., Hancioglu, B., Webb, A., Fisher, J.P., Liu, Z., Lu, X., Tkaczuk, K.H.R., He, X. Bioinspired one cell culture isolates highly tumorigenic and metastatic cancer stem cells capable of multilineage differentiation. *Advanced Science.* 2020.
- White, A., Shamul, J., Xu, J., **Stewart, S.,** Bromberg, J., He, X. Engineering strategies to improve islet transplantation for type 1 diabetes therapy. *ACS Biomaterials Science and Engineering*. 2019.
- Zhang, Y., Wang, H., **Stewart, S.,** Jiang, B., Ou, W., Zao, G., He, X. A Cold-Responsive Nanoparticle Enables Intracellular Delivery and Rapid Release of Trehalose for Organic Solvent-Free Cryopreservation. *Nano Letters.* 2019.
- Xu J., Liu Y., Li Y., Wang H., **Stewart S.**, Agarwal P., Zhang Y., Liu S, Zhao G., Wan J., Lu X., He X. Precise Targeting of POLR2A as a Therapeutic Strategy for Human Triple Negative Breast Cancer. *Nature Nanotechnology*. 2019.

Conference Presentations:

- **Stewart, S.,** Ou, W., He, X., Micromechanical Characterization with AFM Indentation and Viscoelastic Modeling Reveals both Elastic and Viscoelastic Heterogeneities in Ovarian Tissue. Society for Biomaterials 2023 Annual Meeting. San Diego, CA. Oral.

  *Awarded Student Travel Achievement Recognition (STAR)
- **Stewart, S.,** Jiang, B., Li, W., Ou, W., He, X. Sand-Mediated Ice Seeding Enables Serum-Free Low Cryoprotectant Cryopreservation of Human iPSCs. Biomedical Engineering Society 2021 Annual Meeting. Orlando, FL. Oral.
- **Stewart, S.,** Zhang, Y., Wang, H., Jiang, B., He, X. A Cold-Responsive Nanoparticle Enables Intracellular Delivery and Rapid Release of Trehalose for Fast Freezing of Stem Cells. CRYO2019. San Diego, CA. Oral.

  *Awarded Student Travel Award
- **Stewart, S.,** Zhang, Y., Wang, H., Jiang, B., He, X. A Cold-Responsive Nanoparticle Enables Intracellular Delivery and Rapid Release of Trehalose for Fast Freezing of Stem Cells. Summer Biomechanics, Bioengineering, and Biotransport Conference. Seven Springs, PA. 2019. Oral.

  *Awarded 1st Place in Student Paper Competition

Book Chapters:

- Li, W., **Stewart, S.,** Zhou, X., Liu, B., He, X. Technologies for Oocyte Cryopreservation. In *Emerging Technologies in Biophysical Sciences: A World Scientific Reference: Volume 2: Emerging Technologies for Fertility*,

Editors: Dermirci, U., El Assal, R., Ashagar, W: Singapore: World Scientific Publishers/Imperial College Press, pp.179-200, 2023

Chapter 6 Appendices

Appendix 1: Micromechanical characterizations and viscoelastic modeling reveal elastic and viscoelastic heterogeneities in ovarian tissue and the significant viscoelastic contribution to the apparent elastic modulus determined by AFM indentation.

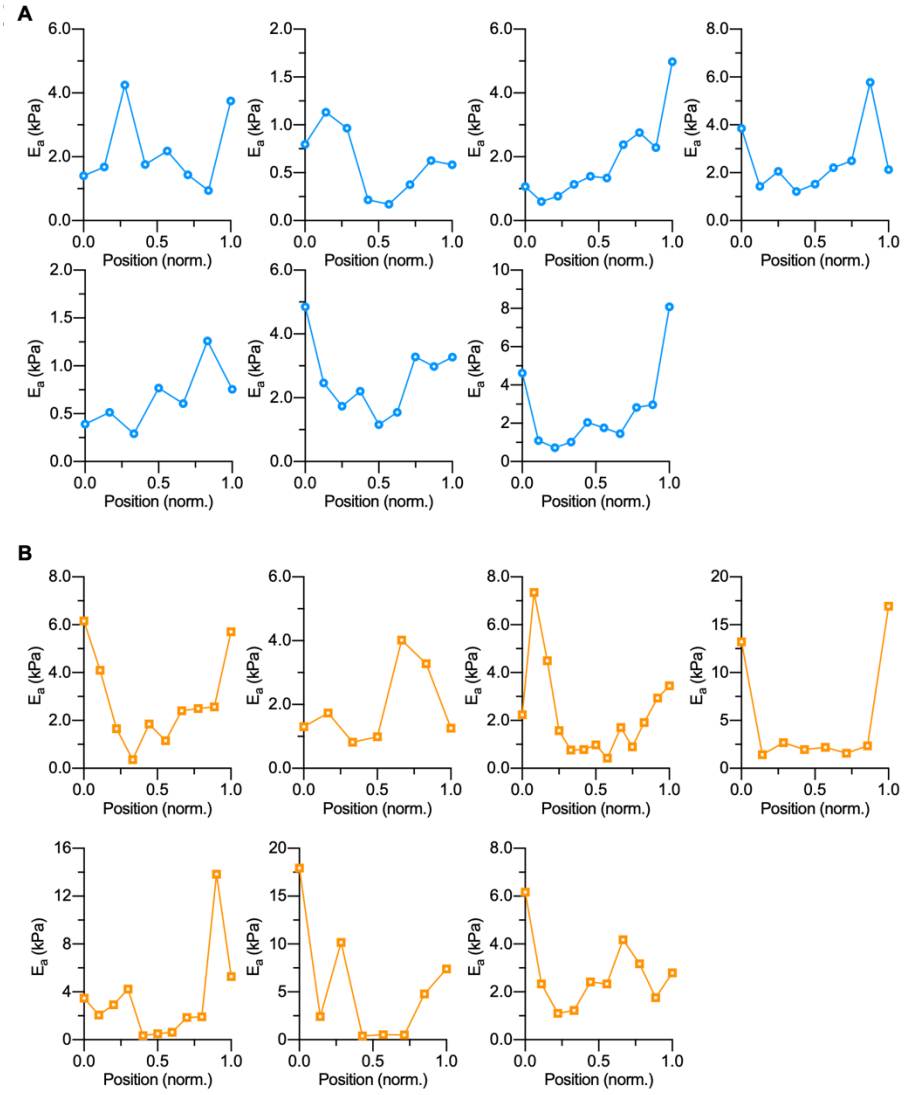

Figure A1.1 Apparent modulus line-scan profiles of reproductively younger and older cat ovaries. Each line-scan profile represents an ovary from **A**, reproductively younger (<6 months, blue) or **B**, reproductively older (>6 months, orange) cat. Markers indicate mean apparent modulus values from one mapping site on the tissue, averaged from three separate 30 µm x 30 µm indentation maps taken at the 100 x 100 μm^2 spatial window of the mapping site. Mapping sites were spaced 100 – 500 µm apart by manual stage adjustment. Position is

normalized to the maximum width of the ovary, which varied because the size of the ovary varied between animals.

Derivation of the constitutive equation of the second-order SLS model

For the second-order SLS model, the total stress, σ , and total strain, ε, across all the three arms (i.e., the purely elastic solid spring arm in parallel with two viscoelastic Maxwell arms) can be expressed as:

$$\sigma = \sigma_e + \sigma_1 + \sigma_2 \quad \textbf{(Eq. A1.1)}$$

$$\varepsilon = \varepsilon_e = \varepsilon_1 = \varepsilon_2 \quad \textbf{(Eq. A1.2)}$$

where σ_e and ε_e are the stress and strain of the purely elastic solid spring arm, $\sigma_1$and ε_1 are the stress and strain of the first Maxwell arm, and σ_2 and ε_2 are the stress and strain of the second Maxwell arm. It is worth noting that **Eq. A1.1** is based on the assumption that the model system is linear (i.e., no synergistic or antagonistic interactions between the three arms), which is what the word "linear" in the name of the SLS model means. The constitutive equation of the purely elastic solid spring arm is given by:

$$\sigma_e = E_e \varepsilon_e \quad \textbf{(Eq. A3)}$$

where E_e is the modulus of the purely elastic solid spring arm. The constitutive equations of the first and second viscoelastic Maxwell arms are:

$$\sigma_1 = \mu_1 \frac{d\varepsilon_1}{dt} - \frac{\mu_1}{E_1}\frac{d\sigma_1}{dt} \quad \textbf{(Eq. A4)}$$

$$\sigma_2 = \mu_2 \frac{d\varepsilon_2}{dt} - \frac{\mu_2}{E_2}\frac{d\sigma_2}{dt} \quad \textbf{(Eq. A5)}$$

where E_1 and E_2 are the moduli of the solid springs in the first and second Maxwell arms, respectively, and μ_1 and μ_2 are the viscosities of the fluid dashpots in the first and second Maxwell arms, respectively. **Eqs. A1.4** and **A1.5** show that the solid springs

with moduli of E_1 and E_2 in the two Maxwell arms may affect the stresses on the two Maxwell arms through the change in stress with time (i.e., $\frac{d\sigma_1}{dt}$ and $\frac{d\sigma_2}{dt}$) instead of their strains (i.e., ε_1 and ε_2), indicating that E_1 and E_2 in the two viscoelastic Maxwell arms do not contribute to the intrinsic elastic modulus of the second-order SLS model system that is not dependent on time or amount and is solely represented by E_e. The constitutive equation of the second-order SLS model, given as **Eq. 2.1** in the main text, can be found by combining **Eqs. A1.1-A1.5** to find the expression for the total stress and strain as a function of time without the stresses and strains on the three arms. The constitutive equation of the first-order SLS model given in **Figure A1.2** can be derived similarly.

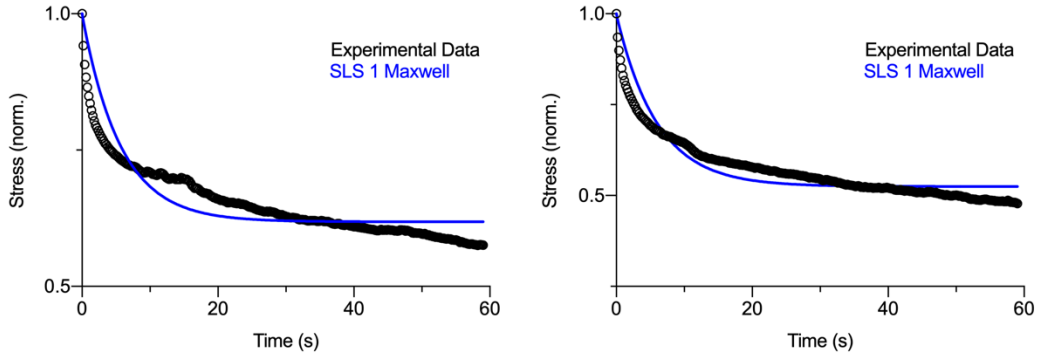

Figure A1.2 Viscoelastic model fitting with the first order standard linear solid (SLS) model. A, Diagram of the first order standard linear solid (SLS) model used for fitting experimental data. The model is composed of a purely elastic solid spring (E_e) arm in parallel with one viscoelastic Maxwell arm (a solid spring in series with a fluid dashpot). The solid spring in the Maxwell arm has an elastic modulus (E_1) and the fluid dashpot has a viscosity (μ_1). The stress and strain are indicated as σ and ε, respectively. **B-C**, Stress relaxation response of cat ovarian cortex (**B**) and, medulla (**C**). Stress is normalized to the maximum stress experienced at time 0. Experimental data (black) shown with model fitting results using the first order SLS model (blue). The first order SLS model shows poor fitting to the experimental data.

Determination of the constants in the general solution to the second-order SLS model for stress relaxation

To find the two constants $\sigma_{1,0}$ and $\sigma_{2,0}$ in the general solution to the second-order SLS model for stress relaxation given in **Eq. 2.3** in the main text, the following initial conditions can be used:

$$t = 0, \sigma = \sigma_0 \quad \textbf{(Eq. A1.6)}$$

$$t = 0, \frac{d\sigma}{dt} = \left.\frac{d\sigma}{dt}\right|_0 \neq 0 \quad \textbf{(Eq. A1.7)}$$

where both σ_0 and $\left.\frac{d\sigma}{dt}\right|_0$ are nonzero constants for the stress and the slope of stress versus time at time 0, respectively. The stress relaxation data shown in **Fig. 2.5A-B** show that $\left.\frac{d\sigma}{dt}\right|_0$ is nonzero and quite high. Applying the initial condition given by **Eq. A1.6** to **Eq. 2.3** in the main text gives the following:

$$\sigma_0 = E_e\varepsilon_0 + \sigma_{1,0} + \sigma_{2,0} \quad \textbf{(Eq. A1.8)}$$

To apply the initial condition given by **Eq. A1.7**, the first derivative with respect to time can be taken on both sides of **Eq. 2.3** in the main text. This gives the following equation:

$$\frac{d\sigma}{dt} = \sigma_{1,0}\left(-\frac{1}{\tau_1}\right)e^{-t/\tau_1} + \sigma_{2,0}\left(-\frac{1}{\tau_2}\right)e^{-t/\tau_2} \quad \textbf{(Eq. A1.9)}$$

Applying the initial condition given by **Eq. A1.7** to **Eq. A1.9**, the following equation can be obtained:

$$\left.\frac{d\sigma}{dt}\right|_0 = -\frac{\sigma_{1,0}}{\tau_1} - \frac{\sigma_{2,0}}{\tau_2} \quad \textbf{(Eq. A1.10)}$$

With **Eqs. A1.8** and **A1.10**, the two constants, $\sigma_{1,0}$ and $\sigma_{2,0}$, can be found as follows:

$$\sigma_{1,0} = \frac{\sigma_0 + \tau_2 \frac{d\sigma}{dt}\Big|_0 - E_e \varepsilon_0}{1 - \frac{\tau_2}{\tau_1}} \quad \textbf{(Eq. A1.11)}$$

$$\sigma_{2,0} = -\tau_2 \frac{d\sigma}{dt}\Big|_0 - \left(\frac{\sigma_0 + \tau_2 \frac{d\sigma}{dt}\Big|_0 - E_e \varepsilon_0}{1 - \frac{\tau_2}{\tau_1}}\right)\left(\frac{\tau_2}{\tau_1}\right) \quad \textbf{(Eq. A1.12)}$$

According to **Eq. 2.4** in the main text, the equivalent modulus at time zero ($E_{eq,0}$) is as follows:

$$E_{eq,0} = E_e + \frac{\sigma_{1,0}}{\varepsilon_0} + \frac{\sigma_{2,0}}{\varepsilon_0} \quad \textbf{(Eq. A1.13)}$$

Replacing $\sigma_{1,0}$ and $\sigma_{2,0}$, with **Eqs. A1.11** and **A1.12**, respectively, the final equation for $E_{eq,0}$ is as follows:

$$E_{eq,0} = E_e + \left(\frac{\sigma_0 + \tau_2 \frac{d\sigma}{dt}\Big|_0 - E_e \varepsilon_0}{1 - \frac{\tau_2}{\tau_1}}\right)\Big/\varepsilon_0 + \left[-\tau_2 \frac{d\sigma}{dt}\Big|_0 - \left(\frac{\sigma_0 + \tau_2 \frac{d\sigma}{dt}\Big|_0 - E_e \varepsilon_0}{1 - \frac{\tau_2}{\tau_1}}\right)\left(\frac{\tau_2}{\tau_1}\right)\right]\Big/\varepsilon_0 \quad \textbf{(Eq. A1.14)}$$

According to **Eqs. A1.13-14**, $\frac{\sigma_{1,0}}{\varepsilon_0} \neq E_1$; $\frac{\sigma_{2,0}}{\varepsilon_0} \neq E_2$; and the equivalent modulus at time 0 is dependent on not only the intrinsic elastic modulus, but also all the viscoelastic properties (i.e., τ_1 and τ_2). Furthermore, per **Eq. 2.3** in the main text and **Eqs. A1.11-14**, the E_1 always goes together with μ_1 as τ_1 and E_2 always goes together with μ_2 as τ_2 in the solution (or equation) for the time-dependent stress. This indicates E_1 and E_2 only affect the stress relaxation rates, and they have no impact on the intrinsic elastic property that is independent of time. The latter is also clear from **Eq. 2.3** in the main text, by setting the time to infinity. Therefore, in the SLS model, there is a clear demarcation of the elastic and viscoelastic contributions through the purely elastic solid arm (E_e) and the viscoelastic arms (τ_1 and τ_2), respectively. This allows the identification of the possible number of different viscoelastic kinetics (Maxwell arms)

by fitting the model with various number of viscoelastic orders (i.e., viscoelastic kinetics or Maxwell arms). For example, two different viscoelastic kinetics (Maxwell arms) are identified in this study for ovarian tissue because the second-order SLS model can give a good fit to the experimental data while the first-order SLS model cannot (**See Fig. A1.2**).

Appendix 2: Sand-mediated ice-seeding enhances cryopreservation of human induced pluripotent stem cells and mouse preantral ovarian follicles

Movie Captions:

Movie 3.1: Sand-mediated ice seeding at high subzero temperature visualized with cryomicroscopy

Movie 3.2: Cardiac differentiation of the cryopreserved hiPSCs

Movie 3.3: Cardiac differentiation of the fresh control hiPSCs

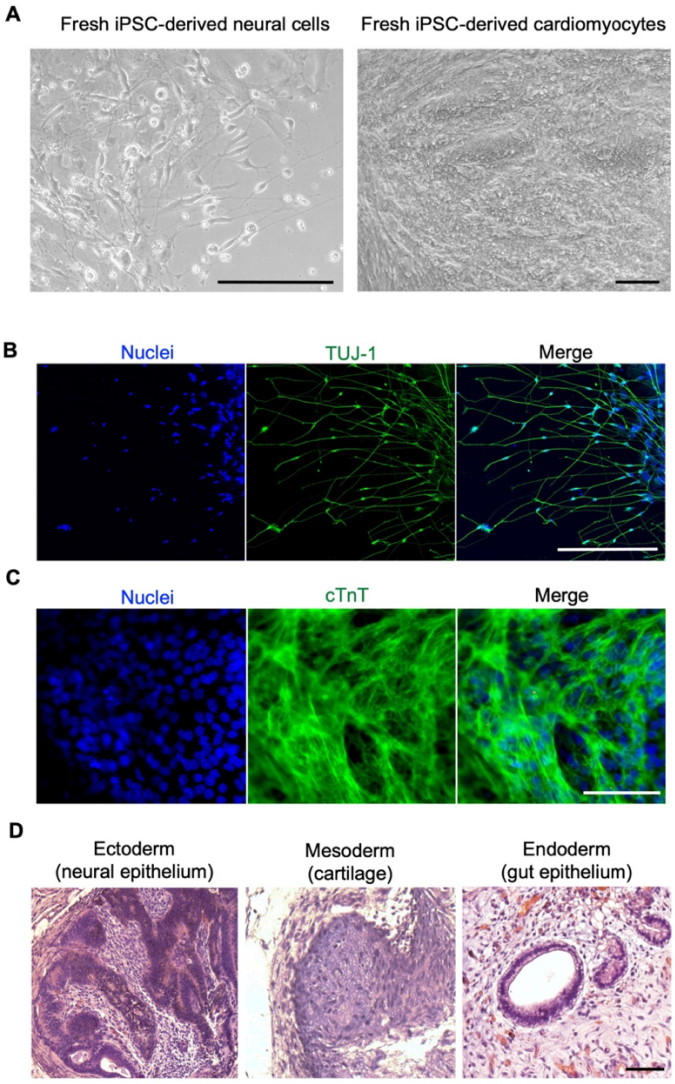

Figure A2.1 Differentiation capacity of fresh control hiPSCs. **A**, The fresh hiPSCs can differentiate into cells with typical neural cell morphology (neurites extending out of the cell body) after neural differentiation (left) and cells with typical morphology of cardiomyocytes (striated pattern). **B**, The fresh control hiPSCs after neural differentiation show high expression of the neural specific protein marker TUJ-1. Cell nuclei are made visible by DAPI staining. **C**, The fresh control hiPSCs after cardiac differentiation highly express cardiac specific protein markers cTnT. Cell nuclei are made visible by DAPI staining. **D**, The teratomas grown from fresh hiPSCs contain tissues from all the three different germ layers including ectoderm (neural epithelium with hypernucelated neuroectodermal structures), mesoderm (the nidus of cartilage with surrounding condensed mesenchymal cells), and endoderm (gut epithelium with subnuclear vacuoles and tube -like structure). Scale bars: 100 μm.

Appendix 3: Intracellular Delivery of Trehalose for Cell Banking[*]

Introduction

As cell-based medicine continues to grow and advance, so does the need for effective and safe methods for long-term storage or banking of living cells [202]. Currently, the most widely used method for banking cells is cryopreservation, using very low temperatures to halt any metabolic and damaging activities. Typical cryopreservation requires the use of cell-membrane penetrating cryoprotective agents or cryoprotectants (CPAs) to keep the cells safe from injury during the cooling and warming processes. Common penetrating CPAs include dimethyl sulfoxide (DMSO) and glycerol. However, these agents can be toxic at 37 °C (body temperature), requiring rigorous and careful removal from the cells before they can be used therapeutically [77]. These washing steps not only add additional time and labor but may also cause the loss of some of the precious cells: approximately 10% of total number with each wash. Therefore, there is a need for nontoxic agents capable of achieving comparable viability of cells post-cryopreservation without the need for washing.

Trehalose, a disaccharide (342 Da) of glucose, has been found to enable organisms in nature to withstand extreme environmental conditions. High concentrations of the small molecule have been found in yeast and extremophiles that allow them to survive extreme cold and drought [203]. This sugar is hypothesized to facilitate survival through two capabilities during dehydration: (1) forming hydrogen bonds with and/or promoting hydration of biomacromolecules, acting as water to allow

[*] Reprinted (adapted) with permission from: Stewart, S., He, X. Intracellular Delivery of Trehalose for Cell Banking. Langmuir 35(23) (2018) 7414-7422. Copyright 2018 American Chemical Society.

cellular components to retain functional conformation and (2) suspend metabolic activity by forming a glassy matrix with extremely low molecular mobility [204].

Studies have shown promise using trehalose as an extracellular protective agent in the media of cells for cryopreservation but failed to match the performance of DMSO. Crowe noted that successful cryopreservation requires trehalose to be present on both sides of the membrane, however, trehalose is naturally impermeable to the mammalian cell membrane [203, 205]. Here we review the different strategies that have been explored to load trehalose into mammalian cells for effective cryopreservation, desiccation, and lyopreservation, as summarized in **Table A3.1**.

Table A3.1. Summary of methods for delivery of trehalose into mammalian cells and their corresponding advantages and disadvantages.

Method	**Advantages**	**Disadvantages**
Phospholipid-Phase Transition *via* thermal, osmotic, or electric stress[183, 206-216]	Control of trehalose loading by manipulating concentration gradient Increasing membrane permeability	Non-specific membrane permeability Cytotoxicity and membrane stability concerns due to thermal, osmotic, and electric shock to cells
Fluid-Phase Endocytosis[217-219]	Taking advantage of the natural cell drinking process	Long incubation time Loading only small amounts of trehalose
Gene expression[220, 221]	Endogenous expression of trehalose	Adenoviral vector cytotoxicity Requiring genetic modification of cells

Engineered pores and channels[222-227]	Reversible based on external stimuli Controllable influx of trehalose by manipulating concentration gradient	Non-specific membrane permeability Use of exogenous, bacterial derived-protein Overstimulation of ATP receptors linked to apoptosis, necrosis, neoplasia
TRET1 Transporter[228, 229]	Selective transport of trehalose across membrane	Requiring genetic modification of cells
Microinjection[201, 230-232]	Direct insertion of controlled amount of trehalose into large cells such as oocytes and early embryos	Not practical for small somatic cells or large number of cells
Polymers and peptides[233-237]	Loading high amounts of intracellular trehalose Increasing membrane permeability	Non-specific membrane permeability Long incubation time Cytotoxicity concerns
Liposomes[238-240]	Biocompatible with cell membrane	Loading only small amounts of trehalose Poor stability
Nanoparticles[81, 241]	Specific transport of high amounts of trehalose Utilizing endocytosis that is the natural process of cell eating No modification to cells	Long (up to 1 day) incubation time
Ultrasound[242]		Affects cell morphology

	Increased membrane permeability	Non-specific membrane permeability
Engineered trehalose[243]	Trehalose-derivative becomes permeable to cells Natural machinery can digest derivative into trehalose	Possible build-up of trehalose-derivative due to limiting esterases

Phospholipid Phase Transition

One of the first approaches developed to achieve an intracellular concentration of trehalose in mammalian cells was to increase the permeability of the cell membrane through induction of a phospholipid phase transition [206]. Thermal, osmotic, and electrical stress have been studied as induction methods to elevate membrane permeability and allow the transport of trehalose into the cells.

Thermal Stress Induced

Concentrated efforts to introduce trehalose into the cytoplasm of mammalian cells began with the efforts of Beattie *et al.* to cryopreserve pancreatic islets [206]. The group took advantage of the lipid phase transition of the islet cell membrane, cooling the cells before freezing in a solution with high-concentration of trehalose. As the islet cells pass through the thermotropic lipid phase transition, their membranes experience elevated permeability to allow an influx of trehalose diffusing down its concentration gradient from the surrounding environment. Trehalose entered the cells increasingly as an inverse function of temperature. After cryopreservation, islets show good post-thaw

viability and function just as well as freshly transplanted islets post-implantation in a rat model.

Thermal shock has also been investigated as a means for trehalose entry by several groups. Human foreskin fibroblasts, both adherent and in suspension, were incubated on ice for 5 minutes along with 50 mM trehalose solution [207]. Internalization or binding of trehalose to the cell membrane was shown, but the method was associated with high levels of cytotoxicity. Hyperthermic temperatures have been explored to load suspended primary rat hepatocytes with trehalose, with cell suspension incubated on ice for 10-15 minutes, supplied with poration solution containing medium and trehalose, and then placed alternately in 0 °C (ice) and 39 °C (water) every 10 minutes for up to 2 hours [208]. Hepatocytes showed a significant amount of trehalose in the cytoplasm (~0.13 M), high viability (83%), and normal morphology and function.

Studies have also shown that freezing can promote cellular uptake of trehalose and have a beneficial impact on cryopreservation [183, 209-211]. In a study on cryopreservation of red blood cells (RBCs) with trehalose, post-thaw survival was found to increase with increasing intracellular trehalose. The sugar likely passes through the membrane during a membrane phase transition during cooling [211]. Wolkers *et al.* suggested a freezing-induced membrane phase transition in the study of cryopreservation of human platelets using solely trehalose as the CPA served to allow the entry of trehalose into the cells [183]. The Wolkers group further studied this behavior in fibroblasts, showing that trehalose was taken up by the cells during freezing and thawing with a loading efficiency of close to 50% and this loading conferred

cryosurvival during a narrow range of cooling rates [209]. The research group then studied the uptake of trehalose by fibroblasts and how it affected their survival after freeze-drying [210]. Although no viable cells were recovered after freeze-drying trehalose-laden fibroblasts, they did observe that the sugar molecule reduces damage caused to DNA.

Osmotic Stress Induced

Satpathy *et al.* combined both phospholipid phase transition of RBC membranes during both cooling and osmotic imbalance to load up to 40 mM of trehalose into RBC cytoplasms [212]. They first attempted to load RBCs with trehalose *via* incubation in isotonic solution at 37 °C but found that intracellular trehalose concentration greatly increased after incubation in extracellular solution with a trehalose concentration well above the isotonic condition. The loading conditions were found to be both time and temperature dependent, and incubation time of 7 hours was sufficient to reach 40 mM intracellular trehalose. This exposure to hypertonic solution resulted in a morphology change of RBCs compared to freshly isolated RBCs; trehalose-loaded RBCs were not of equal size and abnormally shaped.

Zhou *et al.* sought to improve loading of trehalose into RBCs *via* manipulation of the difference in osmotic pressure and concentration between the inside and outside of the cells [213]. To increase osmotic pressure inside, RBCs were dehydrated in hypertonic glucose. Then after, to allow trehalose to enter the cells, RBCs were incubated in hypotonic trehalose solutions. Trehalose uptake by the cells increased with increasing osmotic pressure difference, with intracellular trehalose concentration reaching 43.2 mM when the osmotic pressure difference was 1369.8 mOsm. Although

this method allowed for successful trehalose uptake, hematology study showed that dehydrated RBCs had a 13.7% MCH, or mean cell hemoglobin, compared to fresh RBCS. This means that some hemoglobin molecules escaped the RBCs during the loading process. These modifications, as well as the small amounts of trehalose introduced from high levels of osmotic stress, may make this strategy ill-suited for RBC cryopreservation.

Osmotic manipulation has been studied to load trehalose into cell types other than RBCs; Reuss *et al.* explored the use of osmotically caused volume changes in human T-lymphocytes to load sugars, including trehalose, into the cytoplasm [214]. They took advantage of the cell's ability to regulate its volume, through a process known as regulatory volume decrease (RVD), where initial cell swelling induces activation of membrane channels that allow the influx/efflux of water and ions. These volume sensitive channels can also be leveraged to introduce small molecules into the cell cytoplasm, leading the group to explore how exposure to hypotonic solutions could allow for sugar uptake by the cells. They found when cells were exposed to 200 mOsm media, the membrane permeability to carbohydrates remained poor. However, when the osmolality was decreased to 100 mOsm, the membrane permeability dramatically increased, but only to monomeric carbohydrates. Trehalose influx, therefore, was very poor, and the cells did not reach high intracellular trehalose concentrations. This method could be used to introduce other sugars, like inositol and sorbitol, into the cytoplasm.

Electrical Stress Induced

Electropermeabilization, also known as electroporation or electroinjection, has been used to elevate membrane permeability and introduce foreign molecules into cell cytoplasm that are otherwise impermeable [244]. Through the application of a short, external electrical field pulse, the cell membrane can be transiently and reversibly increased. Cell viability could be enhanced by manipulating pulse parameters, like field strength, duration, and number of pulses.

Shirakashi *et al.* loaded mouse myeloma cells with trehalose *via* electropermeabilization with applications for cryo- and lyopreservation [215]. With mild field-pulse conditions, membrane permeability was indeed elevated, and cells could be safely loaded with up to 100 mM trehalose when incubated in a trehalose-laden medium. Studies showed that higher amounts of trehalose could be loaded into the cells *via* higher field strength and pulses. However, this came at the expense of cell viability, which showed a sharp decrease when the field strength increased to 3.5 kV/cm. This method has the advantage of loading speed—only 10-15 minutes of post-pulse incubation was necessary to load trehalose into the cells. However, as with other methods that target membrane permeability, the resulting trans-membrane molecule transport is not restricted to trehalose. Cell membranes may become osmotically fragile afterwards, which would affect the cellular responses during freezing and thawing.

Later, Dovgan *et al.* explored the use of electroporation to load trehalose into human-adipose derived stem cells (hADSCs) and how it affected cryosurvival [216]. Cells were electroporated in buffer containing either 250 or 400 mM trehalose. They evaluated molecule uptake by studying the uptake of propidium iodide (PI), fluorescence molecule with a molecular weight similar to trehalose. Similar to results

of Shirakashi *et al.*, they found that PI uptake increased with increasing electric field. The uptake of PI reached a plateau at 2 kV/cm and increasing the electric field further only decreased cell recovery post-electroporation. Cells cryopreserved after electroporation at 1.5 kV/cm and incubation in 250 or 400 mM trehalose showed 83 or 78% post-thaw recovery, respectively. The hADSCs cryopreserved *via* the conventional DMSO method (10% DMSO in 90% fetal bovine serum), showed a post-thaw recovery of 91%. Although this value was not statistically significantly different from that obtained from the trehalose-laden cells, this method comes with cytotoxicity concerns from the electric field that rival those found with DMSO. This study did not measure intracellular concentration of trehalose, so the amount of trehalose able to be loaded into the cells *via* this method and its cryoprotective effect on hADSCs is unknown.

Fluid-Phase Endocytosis

One way that cells can probe and monitor the environment around them is through a non-specific "cellular drinking" method known as fluid-phase endocytosis. This mechanism is not prompted by specific binding of membrane receptors and involves the cell intaking some of its environment and internalizing it with a vesicle pinched off from the plasma membrane. This cellular process has been taken advantage of to load trehalose into mammalian cells, by simply incubating cells in the presence of a high extracellular concentration of trehalose.

Wolkers *et al.* studied the loading of trehalose into human platelets *via* fluid-phase endocytosis and subsequent effect on survival after lyophilization [217]. When

incubated in a high extracellular trehalose concentration at 37 °C, human platelets were able to internalize trehalose, measured using the anthrone reaction. Intracellular trehalose concentration increased with the length of incubation, with a loading efficiency reaching almost 60% after 4 hours of incubation. Maximum intracellular concentration reached 15 mM, which allowed high recovery rates of platelets post-lyophilization, reaching up to 88%. However, a good portion of these recovered cells, at the highest rate, were partially lysed or balloon-shaped. Researchers found that lyophilization parameters (prehydration of lyophilizate over water vapor) and initial platelet concentration had large effects on platelet recovery. Platelets loaded with trehalose, lyophilized, and rehydrated showed a thrombin response almost identical to fresh platelets. This study showed that low amounts of intracellular trehalose may be able to confer protection during lyophilization. Oliver *et al.* investigated loading human mesenchymal stem cells (MSCs) with trehalose *via* fluid-phase endocytosis and saw that the cells were able to uptake the sugar molecule, dependent on temperature, incubation time, and extracellular trehalose concentration, loading approximately 20-30 mM trehalose into the cytoplasm [218]. They did not further assess cryo- or lyopreservation of the trehalose-laden cells.

Zhang *et al.* furthered Oliver *et al.*'s work, loading MSCs with trehalose *via* fluid-phase endocytosis and adding PVP40 as an additional protectant for lyophilization [219]. The intracellular trehalose concentration reached roughly 14 mM after 24 hours of incubation in 100 mM extracellular trehalose solution. The cells were then lyophilized, and recovery rates were examined 12 hours after rehydration and plating. The highest recovery rate achieved was almost 70%. However, the MSCs

recovered from lyophilization had significantly impaired abilities to adhere and proliferate and all died within one week. These preliminary studies suggest that lower amounts of intracellular trehalose may be suited for lyophilization but did not confer sufficient lyoprotection in these cases for healthy, proliferating cells post-rehydration. This loading method requires long incubation times that result in very low intracellular trehalose concentrations, seeming more time-consuming to offer a small payoff compared to other methods. This approach would most likely not be best suited to reach intracellular trehalose concentrations that would help offer cryoprotection to many mammalian cells.

Gene Expression

Some groups have taken a genetic engineering approach to achieving high concentrations of intracellular trehalose by enabling mammalian cells to endogenously synthesize trehalose. This was achieved by transfecting them with genes found in anhydrobiotic organisms. In *Escherichia coli*, trehalose synthesis is controlled by the *otsA/B* locus. This genetic sequence encodes *otsA* (trehalose 6-phosphate synthase), which catalyzes the synthesis of trehalose-6-phosphate, and *otsB* (trehalose 6-phosphate phosphatase), which catalyzes the formation of trehalose [245]. The referenced trehalose synthesis pathway can be seen in **Figure A3.1**. To achieve trehalose expression in mammalian cells, Guo *et al.* transfected human primary foreskin fibroblasts with an adenoviral vector expressing *otsA* and *otsB* [220]. Results from their study showed trehalose expression increased with increasing adenoviral vector multiplicity of infection (MOI), reaching 1-1.5 nmol trehalose per 10^6 cells.

However, as the MOI increased, cell viability decreased due to toxicity from the adenoviral infection. After transfection with different MOI's, the group explored the effect of trehalose expression on desiccation tolerance and found cells with a MOI of 200 could maintain 60% viability post rehydration after 24 hours. Viability dropped as the length of time increased, and no cells were viable past 5 days of desiccation.

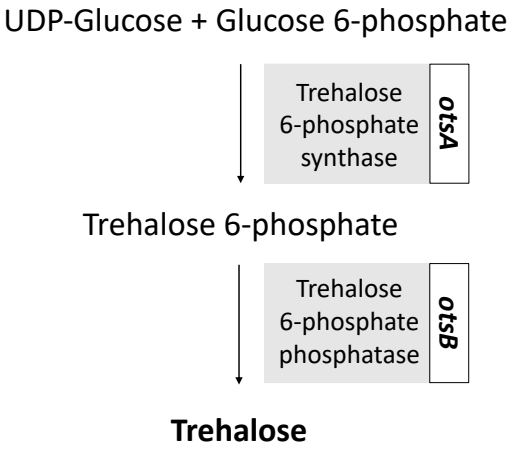

Figure A3.1. Metabolic pathway for synthesis of trehalose. UDPG, Uridine diphosphate. Guo *et al.* [220] refer to trehalose 6-phosphate synthase and phosphatase as *otsA* and *otsB*, respectively.

Garcia de Castro *et al.* transfected a mouse fibroblastoid cell line ($LMTK^-$) with heat-shock inducible *otsA* and *otsB* genes amplified from *E. coli* [221]. Intracellular trehalose increased steadily in $LMTK^-$s after heat shock, reaching a maximum of approximately 80 mM. Trehalose concentration rapidly declined after 30 hours post heat shock, attributed to the limited period that the synthesis genes are active after heat shock. Transfected cells showed improved osmotolerance when subjected to hypotonic conditions, but could not survive desiccation despite containing a much higher amount of intracellular trehalose than the fibroblasts studied by Guo *et al.*

Although both groups successfully engineered mammalian cells to express trehalose endogenously, this approach to achieving an intracellular trehalose concentration does not translate well to cryo- and lyopreservation of cells. Editing the genome of cells intended for clinical or therapeutic applications may cause issues with cell function and raise safety concerns with stem cell regulatory agencies, further hindering or halting use of the preserved cells to treat diseases. The concentration of intracellular trehalose achieved in these studies also would most likely not be high enough to provide for sufficient cell protection from freezing damage during cryopreservation.

Engineered Pores and Channels

Trehalose has also been introduced into mammalian cytoplasm by creating pores and channels in the cell membrane. Toner *et al.* took advantage of a cell membrane porating agent derived from *Staphyloccus aureus*, a genetically engineered endotoxin called α-hemolysin, to generate pores in the lipid bilayers of both fibroblasts and keratinocytes to allow for trehalose influx [222, 223]. These membrane pores, known as H5, allowed reversible elevated membrane permeability—they were able to be switched on or off by the removal or addition of small concentrations of Zn^{2+}, preventing cell lysis from too much solute influx. This method generated intracellular trehalose concentrations of up to 0.5 M within one hour of exposure to extracellular trehalose solution of the same molarity [224]. Loading low concentration (0.2 M) of trehalose into fibroblasts and keratinocytes *via* the H5 technology allowed for cryopreservation with trehalose as the sole CPA. Long-term post-thaw survivals were

80% for fibroblasts and 70% for keratinocytes [223]. Buchanan *et al.* expanded upon this work with H5 technology to use intra- and extracellular trehalose as the sole CPA for a human hematopoietic cell line (acting as a surrogate for stem cells). They found that colony-forming units generated from trehalose-frozen cells were not significantly different from those generated from DMSO-frozen cells [225]. Although H5 allowed for cell membrane permeabilization and cryopreservation, the exogenous, bacteria-derived pore protein would need to be removed before the cells could be used for any cell-based therapy or clinical application, as it could generate an undesired immune response. This may limit the clinical translation of the technology.

Several groups have investigated the activation a transmembrane cell receptor, P2X7 (synonymous with P2Z), in order to form non-selective pores in the plasma membrane that allow the influx of small molecules, namely trehalose [226, 227]. P2X7 is a purinergic receptor channel, opening in the presence of extracellular ATP and closing upon addition of magnesium [226]. P2X7 is best known for its expression on antigen-presenting immune cells, but has ubiquitous distribution in almost all tissues and organs of the body, allowing for poration of a great number of cell types [246]. Buchanan *et al.* activated the P2Z receptor to achieve 200 mM trehalose in hematopoietic progenitor cells and attempted cryopreservation [226]. Trehalose-preserved cells generated 90% of colonies produced by the untreated control cells, compared to DMSO-preserved cells that generated only 70% of colonies produced by the untreated control. Elliot *et al.* explored the use of the P2X7 channel to safely achieve up to 50 mM intracellular trehalose concentration in mouse macrophages [227]. Cells were subsequently desiccated over a range of moisture contents and

showed better next-day survival than control cells. While this strategy is advantageous in that it leverages native cell machinery to load trehalose, increasing poration times showed large decreases in cell survival, and maximizing intracellular trehalose concentration meant sacrificing cell viability. Both nonselective membrane openings, H5 and P2Z/P2X7, could allow not only the influx of trehalose but simultaneously the influx and efflux of undesired molecules. Concerns have also been raised due to evidence that stimulation of the P2X7 receptor could lead to apoptosis, necrosis, or neoplasia [247, 248].

TRET1 Transporter

Organisms that use trehalose to survive extreme conditions possess the necessary machinery to transport the small molecule across their cell membranes. *Polypedilum vanderplanki* larvae are anhydrobiotic rock pool dwellers that survive desiccation and rehydration. During environmental stresses, approximately 20% of their dry mass is accumulated as trehalose [249-251]. Based on these observations, researchers isolated a gene from these organisms that encodes a facilitated trehalose transporter, known as TRET1 [252]. When expressed in mouse oocytes, TRET1 allowed the cells the specific, bidirectional, and high-capacity transport of trehalose across the plasma membrane. Chakraborty *et al.* used TRET1 to load trehalose into Chinese hamster ovary (CHO) cells and saw great improvement in desiccation tolerance compared to control CHO cells [228]. Uchida *et al.* further studied CHO-TRET1 cells in the context of cryopreservation and found that their post-thaw viabilities were much improved compared to CHO cells transfected with an empty

vector [229]. This use of TRET1 enables achievement of high intracellular trehalose concentration, specific transport of solely trehalose without influx or efflux of other small molecules, control over intracellular concentration by changing the gradient created by extracellular trehalose, and ease of transgenesis into cells due to its single gene product nature. However, genetically modifying cells for improved cryo- and lyopreservation might not translate well into clinical applications for cell-based therapies.

Microinjection

The most direct approach studied for loading of trehalose into mammalian cells is to microinject the small molecule directly into the cytoplasm of each individual cell. Eroglu *et al.* successfully delivered trehalose into discarded human oocytes and froze them in the presence of extracellular trehalose [201]. Subsequent study of the trehalose-laden oocytes revealed good survival after cryopreservation. Because of the large size of oocytes (~100 μm in diameter) and typical small sample quantity (only tens to hundreds), these cells are great candidates the for microinjection approach and the delivery was successful [230-232]. However, this approach has limitations for applications to other types of eukaryotic mammalian cells, which are typically much smaller (less than 20 μm in diameter) and in much greater quantity (over millions).

Polymers and peptides

Synthetic polymers have been investigated as facilitators of trehalose into cytoplasm by interacting with the cell membrane and temporarily increasing

permeability[233-237]. Amphipathic polymers with weakly ionizable carboxyl acid side groups and hydrophobic side chains have garnered interest because of their high affinity for lipid membranes and ability to elevate membrane permeability by mimicking viral peptides as well as promote endosomal escape [253, 254]. The most popular biopolymer investigated for trehalose-loading has been PP50, composed of biodegradable poly(L-lysine iso-phthalamide) (PLP) grafted with L-phenylalanine [255]. PP50 has been greatly explored as a method for loading trehalose into RBCs for desiccation tolerance and cryosurvival [233, 235, 256]. This method allowed for a cytoplasmic trehalose concentration of 123 mM in erythrocytes that, along with the presence of extracellular trehalose, resulted in a 20% increase in post-thaw viability compared to erythrocytes without cytoplasmic trehalose [233]. Elevated membrane permeability was able to be reversed by washing in PBS. Longer incubation times increased intracellular trehalose concentration, however, they also increased the incidence of hemolysis. Although this method increased erythrocyte post-thaw survival to roughly 80%, membrane permeabilization was not specific to solely trehalose and could allow for both the influx and efflux of other small molecules. The hemolysis observed in reaction to PP50 was undesirable, and the biopolymer would need to be removed from the cells before any clinical application, necessitating a tedious washing procedure.

Sharp *et al.* and Mercado *et al.* extended the use of PP50 for trehalose loading from red blood to a nucleated cell line derived from human osteosarcoma (SAOS-2)[234, 236]. PP50 was able to safely and effectively load trehalose into the nucleated human cell line. Cells cryopreserved with a combination of PP50 and an extracellular trehalose concentration showed improved post-thaw survival compared to cells preincubated in

trehalose without the polymer [236]. However, cells preserved in the standard cryopreservation protocol, DMSO, showed significantly higher post-thaw viability than PP50-cryopreserved cells (80% *versus* 60%) [234].

Wei *et al.* explored the use of a cell penetrating peptide (CPP) to deliver trehalose into mouse embryonic fibroblasts [237]. They designed a new CPP based on molecular dynamics simulations, with conformations shown in **Figure A3.2**, and the resulting sequence contained many amino acids that allowed the coupling of trehalose through non-covalent bonding. This cargo-coupling allowed specific transport of trehalose into the cell, different from the non-specific membrane permeability induced by PP50. This peptide enabled the delivery of trehalose into the cytoplasm, up to a concentration of 20 mM after 2 hours of incubation. The novel CPP did not exhibit significant toxicity to mammalian cells even at high concentrations. The intracellular trehalose concentration achieved here would probably not sufficient for effective cryopreservation of mammalian cells. Cell types more stress-sensitive than fibroblasts may also not react well to the possibly cytotoxic CPP.

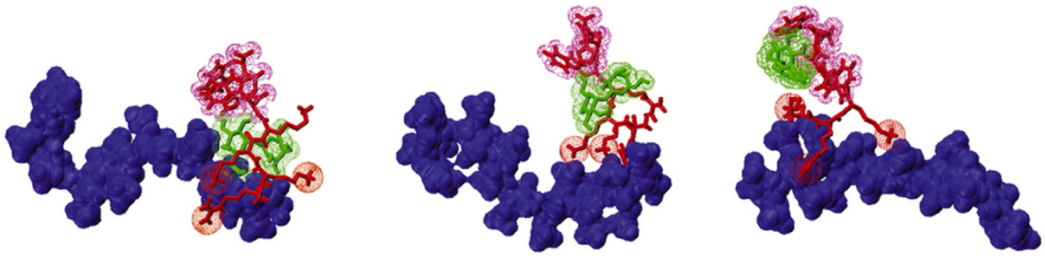

Figure A3.2. The molecular simulations for the binding conformations of trehalose-heparin-CPP to deliver trehalose into mammalian cells. Trehalose is indicated in green, heparin in blue, and the peptides in red. Adapted from: Wei, Y., Li, C., Zhang, L. & Xu, X. Design of novel cell penetrating peptides for the delivery of trehalose into mammalian cells. *Biochim. Biophys. Acta - Biomembr.* **1838,** 1911–1920 (2014). Copyright 2014 Elsevier.

Liposomes

Used in disciplines ranging from medicine, biology, and pharmaceutical science, liposomes are spherical vesicles composed of a lipid bilayer that encloses an aqueous compartment. The liposomes have applications as a delivery vehicle for drugs and other bioactive substances into cells [238]. Because of their structure and biocompatibility, liposomes have been investigated as a carrier for trehalose into the cytoplasm of mammalian cells [211, 238, 239]. Fluorescence and spectrophotometry studies of labelled trehalose-containing liposomes conducted by Holovati *et al.* suggested that liposomes could permeabilize human RBC membranes and safely deliver trehalose into the cytosol [238]. However, this method could only deliver micromolar concentrations of trehalose inside the cells. Holovati *et al.* further extended the study of these liposomes to examine their effect on RBC response to freezing and post-thaw membrane quality. Interestingly, they found improved post-thaw recovery of RBCs due to the application of liposomes, not their delivery of trehalose into the cytosol [239]. Liposomes loaded with trehalose and liposomes loaded with saline showed similar post-thaw recovery for the RBCs. It is important to note, however, that these trehalose-laden liposomes were only able to deliver approximately 15 mM trehalose into the cytosol of the RBCs, which may not have been enough to provide sufficient protection from cryoinjury.

Trehalose-laden liposomes have also been used to cryopreserve stem cells obtained from human umbilical cord blood[43]. Motta *et al.* tested different conditions of intracellular and extracellular trehalose along with DMSO [240]. They found that intra- and extracellular trehalose, with addition of a small amount of DMSO, improved cryopreservation of HSCs in terms of post-thaw viability and stemness similar to

DMSO. Intra- and extracellular trehalose delivered by the liposomes alone did not improve cryopreservation compared to the control. Although these results are promising, liposomes may not be able to load high amounts of trehalose into other types of mammalian cells, and resulting membrane permeabilization may be nonspecific, allowing entry or escape of other small molecules into or out of the cells. In addition, liposomes are not stable in aqueous solutions and they may coalesce to form large vesicles.

Nanoparticles

Research into the field of nanotechnology has garnered much interest, with applications of nanoplatforms ranging from food and water safety to regenerative medicine [41, 257]. Nanoparticles have been investigated as drug vehicles for delivery of chemotherapy, enabling protected delivery of small molecules across the cancer cell membranes [258]. Researchers have used this approach to deliver trehalose across cell membranes to achieve high intracellular trehalose concentrations [81, 241]. Zhang *et al.* developed a thermally responsive polymeric hydrogel nanocapsule for the encapsulation and delivery of trehalose into fibroblasts [241]. Nanocapsules were synthesized from Pluronic F127 (PF127), a triblock copolymer that can self-assemble in aqueous solution in a temperature-dependent manner, and polyethyleneimine (PEI), an endosomolytic cationic polymer found useful in cytosolic gene delivery[259-261]. Trehalose was successfully encapsulated in the nanocapsules; the capsules remained stable and held the trehalose inside during cellular uptake at 37 °C and then remained in the cytoplasm. Quick release of trehalose was enabled by thermally cycling the

nanoparticle between 37 °C and 22 °C and fibroblasts showed an intracellular trehalose concentration of up to 0.3 M after a 40-minute incubation. Neither the nanoparticles nor thermal cycling (cold shock at 22 °C) showed significant toxicity to the cells. Although this method achieved a high intracellular trehalose concentration in a short incubation time, the nanocapsule synthesis process was very involved and required many steps, following a tedious soaking-freezing-drying-heating procedure to encapsulate the trehalose. The fact that room temperature can induce release of trehalose from the nanocapsules makes it very difficult to handle the trehalose-laden nanocapsules for further use.

Rao *et al.* built upon the work with thermally responsive nanoparticles to deliver trehalose into hADSCs and cryopreserve them [81]. In a previous work, Zhang *et al.* improved upon the PF127 nanoconstruct by using chitosan, a naturally derived, biocompatible polysaccharide commonly found in seafood [262], as a crosslinker [263]. Rao *et al.* further improved upon this work by further cross-linking the nanoparticles with genipin to prevent release of trehalose from the nanocapsules at room or lower temperature. Instead, a pH responsive release of trehalose from the nanocapsules at 37 °C could be achieved [81]. The schematic for encapsulation of trehalose in the nanoparticle is shown in **Figure A3.3**.

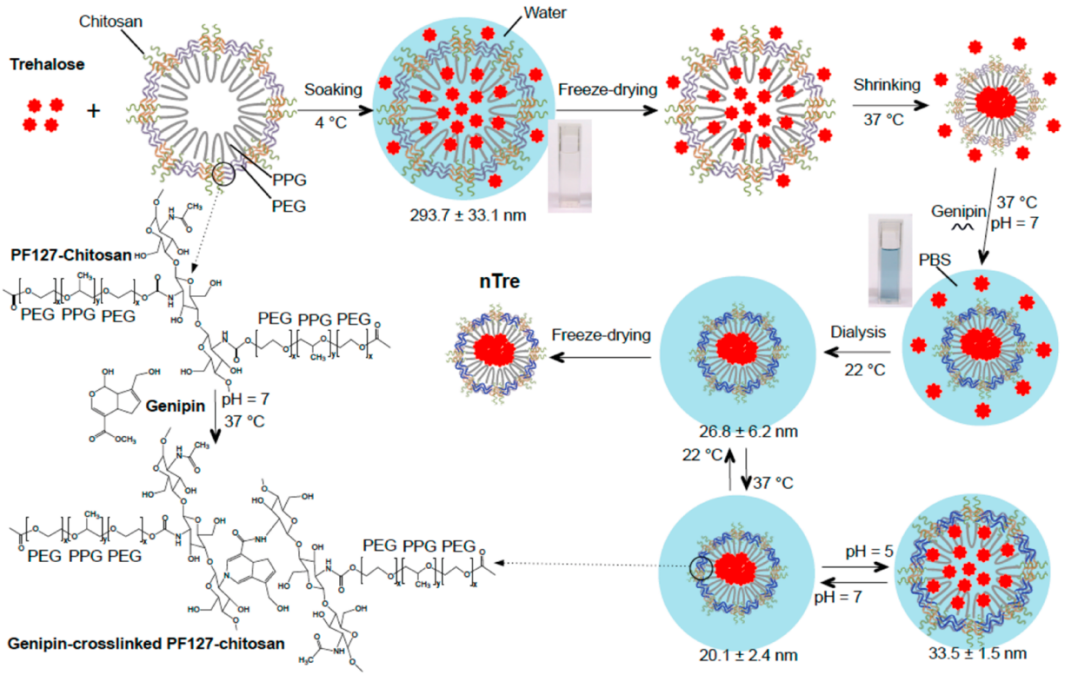

Figure A3.3. A schematic illustration of the procedure for encapsulating hydrophilic (i.e., water-soluble) trehalose in genipin-crosslinked Pluronic F127-chitosan nanoparticles (GNPs) to obtain the nanoparticle-encapsulated trehalose (nTre). After genipin crosslinking, the solution turns from light brown for the aqueous solution of Pluronic F127-chitosan nanoparticles (NPs) into blue for the aqueous solution of GNPs. The GNPs are pH responsive in size at 37 °C although they are not as thermally responsive in size at pH 7 as the Pluronic F127-chitosan NPs. The size (diameter) shown at various temperatures and pH values is for nTre made with a feeding ratio of 1:10 (trehalose:Pluronic F127-chitosan NPs) in weight. PPG: poly(propylene glycol); PEG: poly(ethylene glycol); and PBS: phosphate buffered saline (1x by default). Reprinted with permission from Rao *et al* [81]. Copyright 2015 American Chemical Society.

Cumulative release of trehalose from the pH-responsive nanoparticles was increased at a pH of 5 compared to a pH of 7. Late endosomes are known have an acidic pH, so the faster release of trehalose from the nanoparticles at pH 5 facilitates trehalose release in mammalian cells after cellular uptake. hADSCs were shown to uptake the nanoparticles and their viability was not affected by the nanoparticles themselves. Subsequent cryopreservation of trehalose-laden hADSCs showed comparable post-thaw viability to those cryopreserved with the conventional DMSO treatment. hADSCs also retained their stemness, shown by no significant difference in expression of stem cell genes and

markers and differentiation into osteo-, adipo-, and chondrogenic lineages. Nanoparticle-mediated delivery of trehalose shows great promise for cryopreservation of cell-based therapies, as no possibly harmful modification must be made to the cells or their membranes. Delivery of trehalose is specific—this method does not involve influx or efflux of other small molecules. Possible limitations could be the incubation time needed for sufficient intracellular trehalose concentration—in this study, hADSCs were incubated with the trehalose-laden nanoparticles for 24 hours before cryopreservation. However, nanoparticles designed with cell-targeting modalities and quick payload releases could shorten the incubation time needed and make this method even more attractive.

Other Methods

Zhang *et al.* explored an experimental method of using ultrasound to load trehalose into human platelets [242]. They used different frequencies and exposure times to optimize a procedure to load ~30 mM of trehalose into the platelets by applying 0.8 W/cm^2, 25 kHz ultrasound for 30 minutes. Although platelet number and average volume were not greatly affected by the ultrasound procedure, radiated platelets showed a significantly different morphology from the controls. This method is undesirable for cell preservation applications, as the membrane permeability is non-selective for trehalose, and ultrasound may also compromise activity or change morphology of different cell types as well.

Abazari *et al.* took a different approach to trehalose loading—instead of focusing on manipulating the cell or its membrane, they engineered trehalose itself to

become permeable to mammalian cells [243]. Conjugating the small molecule with six acetyl groups facilitated trehalose uptake into primary rat hepatocytes more efficiently than unmodified trehalose. Once inside the cell, the trehalose derivative could be deacetylated by non-specific esterases located inside the cell to yield trehalose. Although this method allowed for extremely efficient trehalose delivery, it raises some concerns about undesired cellular effects. Because the deacetylation of the modified trehalose occurs by a limited number of cell esterases, an accumulation of the trehalose derivative could occur that may produce harmful effects or not confer cryoprotection. Introduction of this modified molecule into cells intended for clinical use may also incur some risk.

Outlook and Conclusions

If cells are to be banked for research and clinical applications, it is desired that protective agents and the preservation process not greatly affect their structure and functionality. Additionally, ideally preserved cells would be ready for use immediately upon thawing, without the need to remove any agents from the cells or perform other processing steps. Protective agents and the methods for applying them to the cells also should not cause significant cytotoxicity or damage to the cells. If trehalose is to be used as an effective cryo- or lyoprotectant for preserving cells and tissues, its loading method should not significantly alter the cell structure or function, or cause cell damage or death. Methods that allow for selective entry of trehalose are also preferred, as the influx or efflux of other undesired small molecules could have a negative impact on the cells. Approaches that allow for quick trehalose uptake are preferred, as

cryopreservation of cells is usually desired within one day of procurement. Nanoparticles or other encapsulation methods appear to be promising for intracellular delivery of trehalose, as they allow for specific delivery of trehalose without modification of significant cell structures. Future directions for improving this approach include modifying the nanoparticle design to allow for faster and more efficient cellular uptake. Nanoparticles designed with a fast payload release could improve intracellular trehalose concentrations and cut down on incubation time. Cold-responsive nanoparticles capable of releasing trehalose upon exposure to cold temperatures (i.e., lower than room temperature) experienced by the cells during the cooling process would be well suited for cryopreservation applications. Overall, trehalose shows much promise as a nontoxic cryoprotectant that does not need to be removed from cells prior to applications in research or clinical settings. Much advance has been made in developing approaches for delivering the sugar across the plasma membrane into cells. The nanoparticle-mediated approach is particularly attractive. With further development, it might revolutionize the field by offering an organic solvent (e.g., DMSO)-free strategy for cell banking to facilitate the widespread use of living cells in modern medicine.

Acknowledgments

This work is partially supported by grants from NSF (CBET-1831019) and NIH (R01EB023632 and R43HL142371).

Chapter 7 Bibliography

[1] J.S. Richards, S.A. Pangas, The ovary: basic biology and clinical implications, J Clin Invest 120(4) (2010) 963-72.

[2] National Survey of Family Growth. https://www.cdc.gov/nchs/nsfg/index.htm. 2021).

[3] C.R. McCartney, J.C. Marshall, CLINICAL PRACTICE. Polycystic Ovary Syndrome, N Engl J Med 375(1) (2016) 54-64.

[4] A.N. Shelling, Premature ovarian failure, Reproduction 140(5) (2010) 633-41.

[5] L.D. Shea, T.K. Woodruff, A. Shikanov, Bioengineering the ovarian follicle microenvironment, Annu Rev Biomed Eng 16 (2014) 29-52.

[6] M. De Vos, J. Smitz, T.K. Woodruff, Fertility preservation in women with cancer, Lancet 384(9950) (2014) 1302-10.

[7] M. Salama, T.K. Woodruff, From bench to bedside: Current developments and future possibilities of artificial human ovary to restore fertility, Acta Obstet Gynecol Scand 98(5) (2019) 659-664.

[8] D.M. Green, C.A. Sklar, J.D. Boice, Jr., J.J. Mulvihill, J.A. Whitton, M. Stovall, Y. Yasui, Ovarian failure and reproductive outcomes after childhood cancer treatment: results from the Childhood Cancer Survivor Study, J Clin Oncol 27(14) (2009) 2374-81.

[9] W. van Dorp, R. Haupt, R.A. Anderson, R.L. Mulder, M.M. van den Heuvel-Eibrink, E. van Dulmen-den Broeder, H.I. Su, J.F. Winther, M.M. Hudson, J.M. Levine, W.H. Wallace, Reproductive Function and Outcomes in Female Survivors of

Childhood, Adolescent, and Young Adult Cancer: A Review, J Clin Oncol 36(21) (2018) 2169-2180.

[10] R.S. Hussein, Z. Khan, Y. Zhao, Fertility Preservation in Women: Indications and Options for Therapy, Mayo Clin Proc 95(4) (2020) 770-783.

[11] M. Shapira, H. Raanani, Y. Cohen, D. Meirow, Fertility preservation in young females with hematological malignancies, Acta Haematol 132(3-4) (2014) 400-13.

[12] J. Hirshfeld-Cytron, C. Gracia, T.K. Woodruff, Nonmalignant diseases and treatments associated with primary ovarian failure: an expanded role for fertility preservation, J Womens Health (Larchmt) 20(10) (2011) 1467-77.

[13] S. Joshi, B.N. Savani, E.J. Chow, M.H. Gilleece, J. Halter, D.A. Jacobsohn, J. Pidala, G.P. Quinn, J.Y. Cahn, A.A. Jakubowski, N.R. Kamani, H.M. Lazarus, J.D. Rizzo, H.C. Schouten, G. Socie, P. Stratton, M.L. Sorror, A.B. Warwick, J.R. Wingard, A.W. Loren, N.S. Majhail, Clinical guide to fertility preservation in hematopoietic cell transplant recipients, Bone Marrow Transplant 49(4) (2014) 477-84.

[14] F.J. Broekmans, M.R. Soules, B.C. Fauser, Ovarian aging: mechanisms and clinical consequences, Endocr Rev 30(5) (2009) 465-93.

[15] D. Stoop, F. van der Veen, M. Deneyer, J. Nekkebroeck, H. Tournaye, Oocyte banking for anticipated gamete exhaustion (AGE) is a preventive intervention, neither social nor nonmedical, Reprod Biomed Online 28(5) (2014) 548-51.

[16] J.R. Prentice, M. Anzar, Cryopreservation of Mammalian oocyte for conservation of animal genetics, Vet Med Int 2011 (2010).

[17] N. Songsasen, P. Comizzoli, J. Nagashima, M. Fujihara, D.E. Wildt, The domestic dog and cat as models for understanding the regulation of ovarian follicle development in vitro, Reprod Domest Anim 47 Suppl 6 (2012) 13-8.

[18] A. Podfigurna-Stopa, A. Czyzyk, M. Grymowicz, R. Smolarczyk, K. Katulski, K. Czajkowski, B. Meczekalski, Premature ovarian insufficiency: the context of long-term effects, J Endocrinol Invest 39(9) (2016) 983-90.

[19] K. Jankowska, Premature ovarian failure, Prz Menopauzalny 16(2) (2017) 51-56.

[20] J.C. Stevenson, P. Collins, H. Hamoda, I. Lambrinoudaki, A. Maas, K. Maclaran, N. Panay, Cardiometabolic health in premature ovarian insufficiency, Climacteric 24(5) (2021) 474-480.

[21] N.F.C. Henning, A.E. Jakus, M.M. Laronda, Building Organs Using Tissue-Specific Microenvironments: Perspectives from a Bioprosthetic Ovary, Trends Biotechnol (2021).

[22] J. Yu, M.A. Vodyanik, K. Smuga-Otto, J. Antosiewicz-Bourget, J.L. Frane, S. Tian, J. Nie, G.A. Jonsdottir, V. Ruotti, R. Stewart, Slukvin, II, J.A. Thomson, Induced pluripotent stem cell lines derived from human somatic cells, Science 318(5858) (2007) 1917-20.

[23] G. Wang, M. Farzaneh, Mini Review; Differentiation of Human Pluripotent Stem Cells into Oocytes, Curr Stem Cell Res Ther 15(4) (2020) 301-307.

[24] Y.S. Chun, K. Byun, B. Lee, Induced pluripotent stem cells and personalized medicine: current progress and future perspectives, Anat Cell Biol 44(4) (2011) 245-55.

[25] H.W. Denker, Potentiality of embryonic stem cells: an ethical problem even with alternative stem cell sources, J Med Ethics 32(11) (2006) 665-71.

[26] M.D. Pierson Smela, C.C. Kramme, P.R.J. Fortuna, J.L. Adams, R. Su, E. Dong, M. Kobayashi, G. Brixi, V.S. Kavirayuni, E. Tysinger, R.E. Kohman, T. Shioda, P. Chatterjee, G.M. Church, Directed differentiation of human iPSCs to functional ovarian granulosa-like cells via transcription factor overexpression, Elife 12 (2023).

[27] D. Jung, J. Xiong, M. Ye, X. Qin, L. Li, S. Cheng, M. Luo, J. Peng, J. Dong, F. Tang, W. Shen, M.M. Matzuk, K. Kee, In vitro differentiation of human embryonic stem cells into ovarian follicle-like cells, Nat Commun 8 (2017) 15680.

[28] K.M. Elias, N.W. Ng, K.U. Dam, A. Milne, E.R. Disler, A. Gockley, N. Holub, M.L. Seshan, G.M. Church, E.S. Ginsburg, R.M. Anchan, Fertility restoration in mice with chemotherapy induced ovarian failure using differentiated iPSCs, EBioMedicine 94 (2023) 104715.

[29] O. Hikabe, N. Hamazaki, G. Nagamatsu, Y. Obata, Y. Hirao, N. Hamada, S. Shimamoto, T. Imamura, K. Nakashima, M. Saitou, K. Hayashi, Reconstitution in vitro of the entire cycle of the mouse female germ line, Nature 539(7628) (2016) 299-303.

[30] G.D. Vatine, R. Barrile, M.J. Workman, S. Sances, B.K. Barriga, M. Rahnama, S. Barthakur, M. Kasendra, C. Lucchesi, J. Kerns, N. Wen, W.R. Spivia, Z. Chen, J. Van Eyk, C.N. Svendsen, Human iPSC-Derived Blood-Brain Barrier Chips Enable Disease Modeling and Personalized Medicine Applications, Cell Stem Cell 24(6) (2019) 995-1005 e6.

[31] A.A. Youssef, E.G. Ross, R. Bolli, C.J. Pepine, N.J. Leeper, P.C. Yang, The Promise and Challenge of Induced Pluripotent Stem Cells for Cardiovascular Applications, JACC Basic Transl Sci 1(6) (2016) 510-523.

[32] N.E. Vrana, V. Hasirci, G.B. McGuinness, A. Ndreu-Halili, Cell/tissue microenvironment engineering and monitoring in tissue engineering, regenerative medicine, and in vitro tissue models, Biomed Res Int 2014 (2014) 951626.

[33] H.M. Kinnear, C.E. Tomaszewski, F.L. Chang, M.B. Moravek, M. Xu, V. Padmanabhan, A. Shikanov, The ovarian stroma as a new frontier, Reproduction 160(3) (2020) R25-R39.

[34] J.K. Choi, P. Agarwal, H. Huang, S. Zhao, X. He, The crucial role of mechanical heterogeneity in regulating follicle development and ovulation with engineered ovarian microtissue, Biomaterials 35(19) (2014) 5122-8.

[35] T.K. Woodruff, L.D. Shea, A new hypothesis regarding ovarian follicle development: ovarian rigidity as a regulator of selection and health, J Assist Reprod Genet 28(1) (2011) 3-6.

[36] T.I.R. Hopkins, V.L. Bemmer, S. Franks, C. Dunlop, K. Hardy, I.E. Dunlop, Mapping the mechanical microenvironment in the ovary, bioRxiv (2021) 2021.01.03.425098.

[37] E.S. Gargus, K.L. Jakubowski, G.A. Arenas, S.J. Miller, S.S.M. Lee, T.K. Woodruff, Ultrasound Shear Wave Velocity Varies Across Anatomical Region in Ex Vivo Bovine Ovaries, Tissue Eng Part A 26(13-14) (2020) 720-732.

[38] C.D. Wood, M. Vijayvergia, F.H. Miller, T. Carroll, C. Fasanati, L.D. Shea, L.C. Brinson, T.K. Woodruff, Multi-modal magnetic resonance elastography for

noninvasive assessment of ovarian tissue rigidity in vivo, Acta Biomater 13 (2015) 295-300.

[39] E. Ouni, A. Peaucelle, K.T. Haas, O. Van Kerk, M.M. Dolmans, T. Tuuri, M. Otala, C.A. Amorim, A blueprint of the topology and mechanics of the human ovary for next-generation bioengineering and diagnosis, Nat Commun 12(1) (2021) 5603.

[40] Y.M. Efremov, T. Okajima, A. Raman, Measuring viscoelasticity of soft biological samples using atomic force microscopy, Soft Matter 16(1) (2020) 64-81.

[41] O. Chaudhuri, J. Cooper-White, P.A. Janmey, D.J. Mooney, V.B. Shenoy, Effects of extracellular matrix viscoelasticity on cellular behaviour, Nature 584(7822) (2020) 535-546.

[42] A. Levillain, M. Orhant, F. Turquier, T. Hoc, Contribution of collagen and elastin fibers to the mechanical behavior of an abdominal connective tissue, J Mech Behav Biomed Mater 61 (2016) 308-317.

[43] M.P. Kurylo, K. Grandfield, G.W. Marshall, V. Altoe, S. Aloni, S.P. Ho, Effect of proteoglycans at interfaces as related to location, architecture, and mechanical cues, Arch Oral Biol 63 (2016) 82-92.

[44] B. Xu, H. Li, Y. Zhang, Understanding the viscoelastic behavior of collagen matrices through relaxation time distribution spectrum, Biomatter 3(3) (2013).

[45] S. Nam, K.H. Hu, M.J. Butte, O. Chaudhuri, Strain-enhanced stress relaxation impacts nonlinear elasticity in collagen gels, Proc Natl Acad Sci U S A 113(20) (2016) 5492-7.

[46] C.B. Berkholtz, B.E. Lai, T.K. Woodruff, L.D. Shea, Distribution of extracellular matrix proteins type I collagen, type IV collagen, fibronectin, and laminin in mouse folliculogenesis, Histochem Cell Biol 126(5) (2006) 583-92.

[47] F. Amargant, S.L. Manuel, Q. Tu, W.S. Parkes, F. Rivas, L.T. Zhou, J.E. Rowley, C.E. Villanueva, J.E. Hornick, G.S. Shekhawat, J.J. Wei, M.E. Pavone, A.R. Hall, M.T. Pritchard, F.E. Duncan, Ovarian stiffness increases with age in the mammalian ovary and depends on collagen and hyaluronan matrices, Aging Cell 19(11) (2020) e13259.

[48] E. Ouni, C. Bouzin, M.M. Dolmans, E. Marbaix, S. Pyr Dit Ruys, D. Vertommen, C.A. Amorim, Spatiotemporal changes in mechanical matrisome components of the human ovary from prepuberty to menopause, Hum Reprod 35(6) (2020) 1391-1410.

[49] B.P. Best, Cryoprotectant Toxicity: Facts, Issues, and Questions, Rejuvenation Res 18(5) (2015) 422-36.

[50] A.W. Loren, P.B. Mangu, L.N. Beck, L. Brennan, A.J. Magdalinski, A.H. Partridge, G. Quinn, W.H. Wallace, K. Oktay, O. American Society of Clinical, Fertility preservation for patients with cancer: American Society of Clinical Oncology clinical practice guideline update, J Clin Oncol 31(19) (2013) 2500-10.

[51] R.G. Gosden, Prospects for oocyte banking and in vitro maturation, J Natl Cancer Inst Monogr (34) (2005) 60-3.

[52] K.D. Yu, S. Huang, J.X. Zhang, G.Y. Liu, Z.M. Shao, Association between delayed initiation of adjuvant CMF or anthracycline-based chemotherapy and

survival in breast cancer: a systematic review and meta-analysis, BMC Cancer 13 (2013) 240.

[53] W.H. Wallace, R.A. Anderson, D.S. Irvine, Fertility preservation for young patients with cancer: who is at risk and what can be offered?, Lancet Oncol 6(4) (2005) 209-18.

[54] R. Fabbri, Cryopreservation of human oocytes and ovarian tissue, Cell Tissue Bank 7(2) (2006) 113-22.

[55] F. Deepinder, A. Agarwal, Technical and ethical challenges of fertility preservation in young cancer patients, Reprod Biomed Online 16(6) (2008) 784-91.

[56] K.M. Pelican, R.E. Spindler, B.S. Pukazhenthi, D.E. Wildt, M.A. Ottinger, J. Howard, Progestin exposure before gonadotropin stimulation improves embryo development after in vitro fertilization in the domestic cat, Biol Reprod 83(4) (2010) 558-67.

[57] D.E. Wildt, C.J. Levinson, S.W. Seager, Laparoscopic exposure and sequential observation of the ovary of the cycling bitch, Anat Rec 189(3) (1977) 443-9.

[58] M.A. Kutzler, Induction and synchronization of estrus in dogs, Theriogenology 64(3) (2005) 766-75.

[59] C.R. Gracia, J. Chang, L. Kondapalli, M. Prewitt, C.A. Carlson, P. Mattei, S. Jeffers, J.P. Ginsberg, Ovarian tissue cryopreservation for fertility preservation in cancer patients: successful establishment and feasibility of a multidisciplinary collaboration, J Assist Reprod Genet 29(6) (2012) 495-502.

[60] C.A. Amorim, E.C.R. Leonel, Y. Afifi, A. Coomarasamy, S. Fishel, Cryostorage and retransplantation of ovarian tissue as an infertility treatment, Best Pract Res Clin Endocrinol Metab 33(1) (2019) 89-102.

[61] M.M. Dolmans, C. Marinescu, P. Saussoy, A. Van Langendonckt, C. Amorim, J. Donnez, Reimplantation of cryopreserved ovarian tissue from patients with acute lymphoblastic leukemia is potentially unsafe, Blood 116(16) (2010) 2908-14.

[62] X. He, Microfluidic Encapsulation of Ovarian Follicles for 3D Culture, Ann Biomed Eng 45(7) (2017) 1676-1684.

[63] M. Grynberg, M. Poulain, S. Sebag-Peyrelevade, S. le Parco, R. Fanchin, N. Frydman, Ovarian tissue and follicle transplantation as an option for fertility preservation, Fertil Steril 97(6) (2012) 1260-8.

[64] J. Vanacker, V. Luyckx, C. Amorim, M.M. Dolmans, A. Van Langendonckt, J. Donnez, A. Camboni, Should we isolate human preantral follicles before or after cryopreservation of ovarian tissue?, Fertil Steril 99(5) (2013) 1363-1368 e2.

[65] A.S. Van Eyck, C. Bouzin, O. Feron, L. Romeu, A. Van Langendonckt, J. Donnez, M.M. Dolmans, Both host and graft vessels contribute to revascularization of xenografted human ovarian tissue in a murine model, Fertil Steril 93(5) (2010) 1676-85.

[66] Z. Gavish, I. Spector, G. Peer, S. Schlatt, J. Wistuba, H. Roness, D. Meirow, Follicle activation is a significant and immediate cause of follicle loss after ovarian tissue transplantation, J Assist Reprod Genet 35(1) (2018) 61-69.

[67] J.M. Shaw, S.L. Cox, A.O. Trounson, G. Jenkin, Evaluation of the long-term function of cryopreserved ovarian grafts in the mouse, implications for human applications, Mol Cell Endocrinol 161(1-2) (2000) 103-10.

[68] J. Qu, P.A. Godin, M. Nisolle, J. Donnez, Distribution and epidermal growth factor receptor expression of primordial follicles in human ovarian tissue before and after cryopreservation, Hum Reprod 15(2) (2000) 302-10.

[69] C.A. Amorim, A.P. Rodrigues, D. Rondina, P.B. Goncalves, J.R. de Figueiredo, A. Giorgetti, Cryopreservation of ovine primordial follicles using dimethyl sulfoxide, Fertil Steril 79 Suppl 1 (2003) 682-6.

[70] M. Xu, A. Banc, T.K. Woodruff, L.D. Shea, Secondary follicle growth and oocyte maturation by culture in alginate hydrogel following cryopreservation of the ovary or individual follicles, Biotechnol Bioeng 103(2) (2009) 378-86.

[71] K. Jewgenow, L.M. Penfold, H.H. Meyer, D.E. Wildt, Viability of small preantral ovarian follicles from domestic cats after cryoprotectant exposure and cryopreservation, J Reprod Fertil 112(1) (1998) 39-47.

[72] G.J. Morris, E. Acton, Controlled ice nucleation in cryopreservation--a review, Cryobiology 66(2) (2013) 85-92.

[73] I. Massie, C. Selden, H. Hodgson, B. Fuller, S. Gibbons, G.J. Morris, GMP Cryopreservation of Large Volumes of Cells for Regenerative Medicine: Active Control of the Freezing Process, Tissue Engineering Part C: Methods 20(9) (2014) 693-702.

[74] V. Stensvaag, T. Furmanek, K. Lønning, A.J.A. Terzis, R. Bjerkvig, T. Visted, Cryopreservation of Alginate-Encapsulated Recombinant Cells for Antiangiogenic Therapy, Cell Transplantation 13(1) (2004) 35-44.

[75] V. Isachenko, E. Isachenko, J. Reinsberg, M. Montag, F. Braun, H. Van Der Ven, Cryopreservation of human ovarian tissue: effect of spontaneous and initiated ice formation, Reproductive BioMedicine Online 16(3) (2008) 336-345.

[76] Y. Yuan, Y. Yang, Y. Tian, J. Park, A. Dai, R.M. Roberts, Y. Liu, X. Han, Efficient long-term cryopreservation of pluripotent stem cells at -80 degrees C, Sci Rep 6 (2016) 34476.

[77] M.A. Cox, J. Kastrup, M. Hrubiško, Historical perspectives and the future of adverse reactions associated with haemopoietic stem cells cryopreserved with dimethyl sulfoxide, Cell and Tissue Banking 13(2) (2012) 203-215.

[78] S. Rowley, G. Anderson, Effect of DMSO exposure without cryopreservation on hematopoietic progenitor cells, Bone Marrow Transplant 11(5) (1993) 389-393.

[79] L. Weng, P.R. Beauchesne, Dimethyl sulfoxide-free cryopreservation for cell therapy: A review, Cryobiology 94 (2020) 9-17.

[80] C. Bueno, R. Montes, P. Menendez, The ROCK Inhibitor Y-27632 Negatively Affects the Expansion/Survival of Both Fresh and Cryopreserved Cord Blood-Derived CD34+ Hematopoietic Progenitor Cells, Stem Cell Reviews and Reports 6 (2010) 215-223.

[81] W. Rao, H. Huang, H. Wang, S. Zhao, J. Dumbleton, G. Zhao, X. He, Nanoparticle-Mediated Intracellular Delivery Enables Cryopreservation of Human

Adipose-Derived Stem Cells Using Trehalose as the Sole Cryoprotectant, ACS Applied Materials & Interfaces 7(8) (2015) 5017-5028.

[82] S. Chetty, F.W. Pagliuca, C. Honore, A. Kweudjeu, A. Rezania, D.A. Melton, A simple tool to improve pluripotent stem cell differentiation, Nature Methods 10(6) (2013) 553-556.

[83] M. Verheijen, M. Lienhard, Y. Schrooders, O. Clayton, R. Nudischer, S. Boerno, B. Timmermann, N. Selevsek, R. Schlapbach, H. Gmuender, S. Gotta, J. Geraedts, R. Herwig, J. Kleinjans, F. Caiment, DMSO induces drastic changes in human cellular processes and epigenetic landscape in vitro, Scientific Reports 9(1) (2019).

[84] T.A. Grein, D. Freimark, C. Weber, K. Hudel, C. Wallrapp, P. Czermak, Alternatives to Dimethylsulfoxide for Serum-Free Cryopreservation of Human Mesenchymal Stem Cells, The International Journal of Artificial Organs 33(6) (2010) 370-380.

[85] J. Seremak, A. Eroglu, Chemically Defined and Xeno-Free Cryopreservation of Human-Induced Pluripotent Stem Cells, Methods Mol Biol 2180 (2021) 569-579.

[86] J. Donnez, M.-M. Dolmans, Fertility Preservation in Women, New England Journal of Medicine 377(17) (2017) 1657-1665.

[87] Fertility preservation and reproduction in patients facing gonadotoxic therapies: an Ethics Committee opinion, Fertil Steril 110(3) (2018) 380-386.

[88] B. Vollenhoven, S. Hunt, Ovarian ageing and the impact on female fertility, F1000Res 7 (2018).

[89] A.C. Herta, F. Lolicato, J.E.J. Smitz, In vitro follicle culture in the context of IVF, Reproduction 156(1) (2018) F59-F73.

[90] Q. Yang, L. Zhu, L. Jin, Human Follicle in vitro Culture Including Activation, Growth, and Maturation: A Review of Research Progress, Front Endocrinol (Lausanne) 11 (2020) 548.

[91] S. Jorge, S. Chang, J.J. Barzilai, P. Leppert, J.H. Segars, Mechanical signaling in reproductive tissues: mechanisms and importance, Reprod Sci 21(9) (2014) 1093-107.

[92] E.S. Gargus, H.B. Rogers, K.E. McKinnon, M.E. Edmonds, T.K. Woodruff, Engineered reproductive tissues, Nat Biomed Eng 4(4) (2020) 381-393.

[93] E.E. Telfer, M.B. Zelinski, Ovarian follicle culture: advances and challenges for human and nonhuman primates, Fertil Steril 99(6) (2013) 1523-33.

[94] C.J. Chan, C. Bevilacqua, R. Prevedel, Mechanical mapping of mammalian follicle development using Brillouin microscopy, Communications Biology 4(1) (2021) 1133.

[95] E.R. West, M. Xu, T.K. Woodruff, L.D. Shea, Physical properties of alginate hydrogels and their effects on in vitro follicle development, Biomaterials 28(30) (2007) 4439-48.

[96] T.I.R. Hopkins, V.L. Bemmer, S. Franks, C. Dunlop, K. Hardy, I.E. Dunlop, Micromechanical mapping of the intact ovary interior reveals contrasting mechanical roles for follicles and stroma, Biomaterials 277 (2021) 121099.

[97] N.F.C. Henning, M.M. Laronda, The matrisome contributes to the increased rigidity of the bovine ovarian cortex and provides a source of new bioengineering tools to investigate ovarian biology, bioRxiv (2021) 2021.10.06.463107.

[98] J.S. Shah, R. Sabouni, K.C. Cayton Vaught, C.M. Owen, D.F. Albertini, J.H. Segars, Biomechanics and mechanical signaling in the ovary: a systematic review, J Assist Reprod Genet 35(7) (2018) 1135-1148.

[99] I. Kawashima, K. Kawamura, Regulation of follicle growth through hormonal factors and mechanical cues mediated by Hippo signaling pathway, Syst Biol Reprod Med 64(1) (2018) 3-11.

[100] A. Weber, J. Iturri, R. Benitez, J.L. Toca-Herrera, Measuring biomaterials mechanics with atomic force microscopy. 1. Influence of the loading rate and applied force (pyramidal tips), Microsc Res Tech 82(9) (2019) 1392-1400.

[101] F.B. Nutter, J.F. Levine, M.K. Stoskopf, Reproductive capacity of free-roaming domestic cats and kitten survival rate, Journal of the American Veterinary Medical Association 225(9) (2004) 1399-1402.

[102] E.R. West, L.D. Shea, T.K. Woodruff, Engineering the follicle microenvironment, Semin Reprod Med 25(4) (2007) 287-99.

[103] C.W. McCloskey, D.P. Cook, B.S. Kelly, F. Azzi, C.H. Allen, A. Forsyth, J. Upham, K.J. Rayner, D.A. Gray, R.W. Boyd, S. Murugkar, B. Lo, D. Trudel, M.K. Senterman, B.C. Vanderhyden, Metformin Abrogates Age-Associated Ovarian Fibrosis, Clin Cancer Res 26(3) (2020) 632-642.

[104] S.M. Briley, S. Jasti, J.M. McCracken, J.E. Hornick, B. Fegley, M.T. Pritchard, F.E. Duncan, Reproductive age-associated fibrosis in the stroma of the mammalian ovary, Reproduction 152(3) (2016) 245-260.

[105] S. Wang, Y. Zheng, J. Li, Y. Yu, W. Zhang, M. Song, Z. Liu, Z. Min, H. Hu, Y. Jing, X. He, L. Sun, L. Ma, C.R. Esteban, P. Chan, J. Qiao, Q. Zhou, J.C. Izpisua

Belmonte, J. Qu, F. Tang, G.H. Liu, Single-Cell Transcriptomic Atlas of Primate Ovarian Aging, Cell 180(3) (2020) 585-600 e19.

[106] H.E. Sumbul, B.S. Avci, M. Bankir, B.C. Pekoz, E. Gulumsek, A.S. Koc, Ovarian Stiffness Is Significantly Increased in Polycystic Ovary Syndrome and Related With Anti-Mullerian Hormone: A Point Shear Wave Elastography Study, Ultrasound Q 38(1) (2022) 83-88.

[107] V. Vogel, M. Sheetz, Local force and geometry sensing regulate cell functions, Nat Rev Mol Cell Biol 7(4) (2006) 265-75.

[108] A.R. Cameron, J.E. Frith, J.J. Cooper-White, The influence of substrate creep on mesenchymal stem cell behaviour and phenotype, Biomaterials 32(26) (2011) 5979-93.

[109] D.J. Mooney, R. Langer, D.E. Ingber, Cytoskeletal filament assembly and the control of cell spreading and function by extracellular matrix, J Cell Sci 108 (Pt 6) (1995) 2311-20.

[110] O. Chaudhuri, L. Gu, D. Klumpers, M. Darnell, S.A. Bencherif, J.C. Weaver, N. Huebsch, H.P. Lee, E. Lippens, G.N. Duda, D.J. Mooney, Hydrogels with tunable stress relaxation regulate stem cell fate and activity, Nat Mater 15(3) (2016) 326-34.

[111] P. Jamalzaei, M. Rezazadeh Valojerdi, L. Montazeri, H. Baharvand, Applicability of Hyaluronic Acid-Alginate Hydrogel and Ovarian Cells for In Vitro Development of Mouse Preantral Follicles, Cell J 22(Suppl 1) (2020) 49-60.

[112] N. Takahashi, W. Tarumi, B. Ishizuka, Involvement of hyaluronan synthesis in ovarian follicle growth in rats, Reproduction 147(2) (2014) 189-97.

[113] T.K. Woodruff, L.D. Shea, The role of the extracellular matrix in ovarian follicle development, Reprod Sci 14(8 Suppl) (2007) 6-10.

[114] S. Joo, S.H. Oh, S. Sittadjody, E.C. Opara, J.D. Jackson, S.J. Lee, J.J. Yoo, A. Atala, The effect of collagen hydrogel on 3D culture of ovarian follicles, Biomed Mater 11(6) (2016) 065009.

[115] S. Sahai, M. Wilkerson, A.M. Zaske, S.D. Olson, C.S. Cox, F. Triolo, A cost-effective method to immobilize hydrated soft-tissue samples for atomic force microscopy, Biotechniques 61(4) (2016) 206-209.

[116] H. Butt, M. Jaschke, Calculation of thermal noise in atomic force microscopy, Nanotechnology 6(1) (1995) 1-7.

[117] A.R. Harris, G.T. Charras, Experimental validation of atomic force microscopy-based cell elasticity measurements, Nanotechnology 22(34) (2011) 345102.

[118] T. Glozman, H. Azhari, A method for characterization of tissue elastic properties combining ultrasonic computed tomography with elastography, J Ultrasound Med 29(3) (2010) 387-98.

[119] J.E. Rowley, G.E. Rubenstein, S.L. Manuel, N.L. Johnson, J. Surgnier, P.P. Kapitsinou, F.E. Duncan, M.T. Pritchard, Tissue-specific Fixation Methods Are Required for Optimal In Situ Visualization of Hyaluronan in the Ovary, Kidney, and Liver, J Histochem Cytochem 68(1) (2020) 75-91.

[120] J. Yu, M.A. Vodyanik, K. Smuga-Otto, J. Antosiewicz-Bourget, J.L. Frane, S. Tian, J. Nie, G.A. Jonsdottir, V. Ruotti, R. Stewart, I.I. Slukvin, J.A. Thomson, Induced Pluripotent Stem Cell Lines Derived from Human Somatic Cells, Science 318(5858) (2007) 1917-1920.

[121] V.K. Singh, M. Kalsan, N. Kumar, A. Saini, R. Chandra, Induced pluripotent stem cells: applications in regenerative medicine, disease modeling, and drug discovery, Frontiers in Cell and Developmental Biology 3 (2015).

[122] J. Wang, J. Hao, D. Bai, Q. Gu, W. Han, L. Wang, Y. Tan, X. Li, K. Xue, P. Han, Z. Liu, Y. Jia, J. Wu, L. Liu, L. Wang, W. Li, Z. Liu, Q. Zhou, Generation of clinical-grade human induced pluripotent stem cells in Xeno-free conditions, Stem Cell Research & Therapy 6(1) (2015).

[123] C.-Y. Huang, C.-L. Liu, C.-Y. Ting, Y.-T. Chiu, Y.-C. Cheng, M.W. Nicholson, P.C.H. Hsieh, Human iPSC banking: barriers and opportunities, Journal of Biomedical Science 26(1) (2019).

[124] B. Jiang, L. Yan, J.G. Shamul, M. Hakun, X. He, Stem Cell Therapy of Myocardial Infarction: A Promising Opportunity in Bioengineering, Advanced Therapeutics 3 (2020) 1900182.

[125] Y. Xu, C. Chen, P.B. Hellwarth, X. Bao, Biomaterials for stem cell engineering and biomanufacturing, Bioact Mater 4 (2019) 366-379.

[126] C.A. Amorim, D. Rondina, A.P. Rodrigues, P.B. Goncalves, J.R. de Figueiredo, A. Giorgetti, Cryopreservation of isolated ovine primordial follicles with propylene glycol and glycerol, Fertil Steril 81 Suppl 1 (2004) 735-40.

[127] P. Mazur, Freezing of living cells: mechanisms and implications, American Journal of Physiology-Cell Physiology 247(3) (1984) C125-C142.

[128] F.W. Kleinhans, Membrane Permeability Modeling: Kedem–Katchalsky vs a Two-Parameter Formalism, Cryobiology 37(4) (1998) 271-289.

[129] K.R. Diller, Quantitative low temperature optical microscopy of biological systems, J Microsc 126(Pt 1) (1982) 9-28.

[130] F. Franks, biophysics and biochemistry at low temperatures, FEBS LETTERS 220(1) (1987).

[131] H. Huang, J.K. Choi, W. Rao, S. Zhao, P. Agarwal, G. Zhao, X. He, Alginate hydrogel microencapsulation inhibits devitrification and enables large-volume low-CPA cell vitrification, Advanced Functional Materials 25 (2015) 6839-6850.

[132] X. He, J.C. Bischof, Quantification of temperature and injury response in thermal therapy and cryosurgery, Crit Rev Biomed Eng 31(5-6) (2003) 355-422.

[133] X. He, Thermostability of biological systems: fundamentals, challenges, and quantification, Open Biomed Eng J 5 (2011) 47-73.

[134] H. Huang, G. Zhao, Y. Zhang, J. Xu, T.L. Toth, X. He, Predehydration and Ice Seeding in the Presence of Trehalose Enable Cell Cryopreservation, ACS Biomater Sci Eng 3(8) (2017) 1758-1768.

[135] P.M. Zavos, E.F. Graham, Effects of various degrees of supercooling and nucleation temperatures on fertility of frozen turkey spermatozoa, Cryobiology 20(5) (1983) 553-559.

[136] P. Mazur, Physical and Temporal Factors Involved in the Death of Yeast at Subzero Temperatures, Biophysical Journal 1(3) (1961) 247-264.

[137] F.S. Trad, M. Toner, J.D. Biggers, Effects of cryoprotectants and ice-seeding temperature on intracellular freezing and survival of human oocytes, Human Reproduction 14(6) (1999) 1569-1577.

[138] C.E. Morris, D.G. Georgakopoulos, D.C. Sands, Ice nucleation active bacteria and their potential role in precipitation, Journal de Physique IV (Proceedings) 121 (2004) 87-103.

[139] L.R. Maki, E.L. Galyan, M.-M. Chang-Chien, D.R. Caldwell, Ice Nucleation Induced by *Pseudomonas syringae*, Applied Microbiology 28(3) (1974) 456-459.

[140] F.W. Kleinhans, J.F. Guenther, D.M. Roberts, P. Mazur, Analysis of intracellular ice nucleation in Xenopus oocytes by differential scanning calorimetry, Cryobiology 52(1) (2006) 128-138.

[141] B. Jin, S. Seki, E. Paredes, J. Qiu, Y. Shi, Z. Zhang, C. Ma, S. Jiang, J. Li, F. Yuan, S. Wang, X. Shao, P. Mazur, Intracellular ice formation in mouse zygotes and early morulae vs. cooling rate and temperature-experimental vs. theory, Cryobiology 73(2) (2016) 181-186.

[142] I. Massie, C. Selden, H. Hodgson, B. Fuller, Cryopreservation of Encapsulated Liver Spheroids for a Bioartificial Liver: Reducing Latent Cryoinjury Using an Ice Nucleating Agent, Tissue Engineering Part C: Methods 17(7) (2011) 765-774.

[143] T. Kojima, T. Soma, N. Oguri, Effect of ice nucleation by droplet of immobilized silver iodide on freezing of rabbit and bovine embryos, Theriogenology 30(6) (1988) 199-1207.

[144] T. Kojima, T. Soma, N. Oguri, Effect of silver iodide as an ice inducer on viability of frozen-thawed rabbit morulae, Theriogenology 26(3) (1986) 341-352.

[145] L. Weng, S.L. Stott, M. Toner, Exploring Dynamics and Structure of Biomolecules, Cryoprotectants, and Water Using Molecular Dynamics Simulations:

Implications for Biostabilization and Biopreservation, Annu Rev Biomed Eng 21 (2019) 1-31.

[146] J.E. Lovelock, M.W. Bishop, Prevention of freezing damage to living cells by dimethyl sulphoxide, Nature 183(4672) (1959) 1394-5.

[147] Z.W. Yu, P.J. Quinn, Dimethyl sulphoxide: a review of its applications in cell biology, Biosci Rep 14(6) (1994) 259-81.

[148] I. Damjanov, P.W. Andrews, Teratomas produced from human pluripotent stem cells xenografted into immunodeficient mice - a histopathology atlas, Int J Dev Biol 60(10-11-12) (2016) 337-419.

[149] H. Hentze, P.L. Soong, S.T. Wang, B.W. Phillips, T.C. Putti, N.R. Dunn, Teratoma formation by human embryonic stem cells: evaluation of essential parameters for future safety studies, Stem Cell Res 2(3) (2009) 198-210.

[150] C. Ladanyi, A. Mor, M.S. Christianson, N. Dhillon, J.H. Segars, Recent advances in the field of ovarian tissue cryopreservation and opportunities for research, J Assist Reprod Genet 34(6) (2017) 709-722.

[151] C.R.L. Ellen, M.L. Carolina, A.A. Christiani, Cryopreservation of Preantral Follicles, in: B. Yusuf (Ed.), Cryopreservation Biotechnology in Biomedical and Biological Sciences, IntechOpen, Rijeka, 2018, p. Ch. 5.

[152] E. Cho, Y.Y. Kim, K. Noh, S.Y. Ku, A new possibility in fertility preservation: The artificial ovary, J Tissue Eng Regen Med 13(8) (2019) 1294-1315.

[153] M.M. Laronda, A.L. Rutz, S. Xiao, K.A. Whelan, F.E. Duncan, E.W. Roth, T.K. Woodruff, R.N. Shah, A bioprosthetic ovary created using 3D printed

microporous scaffolds restores ovarian function in sterilized mice, Nat Commun 8 (2017) 15261.

[154] M. Soares, K. Sahrari, C.A. Amorim, P. Saussoy, J. Donnez, M.M. Dolmans, Evaluation of a human ovarian follicle isolation technique to obtain disease-free follicle suspensions before safely grafting to cancer patients, Fertil Steril 104(3) (2015) 672-80 e2.

[155] R.J. Rodgers, H.F. Irving-Rodgers, D.L. Russell, Extracellular matrix of the developing ovarian follicle, Reproduction 126(4) (2003) 415-24.

[156] M. Kometas, G.M. Christman, J. Kramer, A. Rhoton-Vlasak, Methods of Ovarian Tissue Cryopreservation: Is Vitrification Superior to Slow Freezing?-Ovarian Tissue Freezing Methods, Reprod Sci 28(12) (2021) 3291-3302.

[157] R.C. Chian, Y. Wang, Y.R. Li, Oocyte vitrification: advances, progress and future goals, J Assist Reprod Genet 31(4) (2014) 411-20.

[158] C. Tian, L. Shen, C. Gong, Y. Cao, Q. Shi, G. Zhao, Microencapsulation and nanowarming enables vitrification cryopreservation of mouse preantral follicles, Nat Commun 13(1) (2022) 7515.

[159] E.P.F. Lopes, G.Q. Rodrigues, D.C.C. de Brito, R.M.P. Rocha, A.C.A. Ferreira, N.A.R. de Sa, R.F.D. Silva, G.L.H. de Alcantara, B.G. Alves, J.R. Figueiredo, M. Zelinski, A.P.R. Rodrigues, Vitrification of caprine secondary and early antral follicles as a perspective to preserve fertility function, Reprod Biol 20(3) (2020) 371-378.

[160] V. Isachenko, E. Isachenko, J. Reinsberg, M. Montag, F. Braun, H. van der Ven, Cryopreservation of human ovarian tissue: effect of spontaneous and initiated ice formation, Reprod Biomed Online 16(3) (2008) 336-45.

[161] J.M. Zhang, Y. Sheng, Y.Z. Cao, H.Y. Wang, Z.J. Chen, Effects of cooling rates and ice-seeding temperatures on the cryopreservation of whole ovaries, J Assist Reprod Genet 28(7) (2011) 627-33.

[162] Y. Jiang, X.L. Lian, Heart regeneration with human pluripotent stem cells: Prospects and challenges, Bioact Mater 5(1) (2020) 74-81.

[163] C.J. Hunt, Technical Considerations in the Freezing, Low-Temperature Storage and Thawing of Stem Cells for Cellular Therapies, Transfus Med Hemother 46(3) (2019) 134-150.

[164] Y. Li, J.C. Tan, L.S. Li, Comparison of three methods for cryopreservation of human embryonic stem cells, Fertility and sterility 93(3) (2010) 999-1005.

[165] Y. Miyamoto, H. Noguchi, H. Yukawa, K. Oishi, K. Matsushita, H. Iwata, S. Hayashi, Cryopreservation of Induced Pluripotent Stem Cells, Cell Med 3(1-3) (2012) 89-95.

[166] W. Liu, G. Chen, Cryopreservation of human pluripotent stem cells in defined medium, Curr Protoc Stem Cell Biol 31 (2014) 1C 17 1-13.

[167] K. Imaizumi, N. Nishishita, M. Muramatsu, T. Yamamoto, C. Takenaka, S. Kawamata, K. Kobayashi, S. Nishikawa, T. Akuta, A simple and highly effective method for slow-freezing human pluripotent stem cells using dimethyl sulfoxide, hydroxyethyl starch and ethylene glycol, PloS one 9(2) (2014) e88696.

[168] G. Zhao, X. Liu, K. Zhu, X. He, Hydrogel Encapsulation Facilitates Rapid-Cooling Cryopreservation of Stem Cell-Laden Core-Shell Microcapsules as Cell-Biomaterial Constructs, Advanced healthcare materials 6(23) (2017).

[169] Y. Zhang, H. Wang, S. Stewart, B. Jiang, W. Ou, G. Zhao, X. He, Cold-Responsive Nanoparticle Enables Intracellular Delivery and Rapid Release of Trehalose for Organic-Solvent-Free Cryopreservation, Nano Lett 19(12) (2019) 9051-9061.

[170] T. Miyazaki, H. Suemori, Slow Cooling Cryopreservation Optimized to Human Pluripotent Stem Cells, Adv Exp Med Biol 951 (2016) 57-65.

[171] T.W. Theunissen, B.E. Powell, H. Wang, M. Mitalipova, D.A. Faddah, J. Reddy, Z.P. Fan, D. Maetzel, K. Ganz, L. Shi, T. Lungjangwa, S. Imsoonthornruksa, Y. Stelzer, S. Rangarajan, A. D'Alessio, J. Zhang, Q. Gao, M.M. Dawlaty, R.A. Young, N.S. Gray, R. Jaenisch, Systematic identification of culture conditions for induction and maintenance of naive human pluripotency, Cell Stem Cell 15(4) (2014) 471-487.

[172] S. Chetty, F.W. Pagliuca, C. Honore, A. Kweudjeu, A. Rezania, D.A. Melton, A simple tool to improve pluripotent stem cell differentiation, Nat Methods 10(6) (2013) 553-6.

[173] A. Kumar, C. Marcolli, T. Peter, Ice nucleation activity of silicates and aluminosilicates in pure water and aqueous solutions – Part 2: Quartz and amorphous silica, Atmospheric Chemistry and Physics 19(9) (2019) 6035-6058.

[174] A.D. Harrison, K. Lever, A. Sanchez-Marroquin, M.A. Holden, T.F. Whale, M.D. Tarn, J.B. Mcquaid, B.J. Murray, The ice-nucleating ability of quartz immersed

in water and its atmospheric importance compared to K-feldspar, Atmospheric Chemistry and Physics 19(17) (2019) 11343-11361.

[175] M.A. Holden, T.F. Whale, M.D. Tarn, D. O'Sullivan, R.D. Walshaw, B.J. Murray, F.C. Meldrum, H.K. Christenson, High-speed imaging of ice nucleation in water proves the existence of active sites, Science Advances 5(2) (2019) eaav4316.

[176] W. Zhang, G. Yang, A. Zhang, L.X. Xu, X. He, Preferential vitrification of water in small alginate microcapsules significantly augments cell cryopreservation by vitrification, Biomed Microdevices 12(1) (2010) 89-96.

[177] J. Wang, G. Zhao, Z. Zhang, X. Xu, X. He, Magnetic induction heating of superparamagnetic nanoparticles during rewarming augments the recovery of hUCM-MSCs cryopreserved by vitrification, Acta Biomater 33 (2016) 264-274.

[178] N. Manuchehrabadi, Z. Gao, J. Zhang, H.L. Ring, Q. Shao, F. Liu, M. McDermott, A. Fok, Y. Rabin, K.G.M. Brockbank, M. Garwood, C.L. Haynes, J.C. Bischof, Improved tissue cryopreservation using inductive heating of magnetic nanoparticles, Science Translational Medicine 9(379) (2017) eaah4586.

[179] X. Liu, G. Zhao, Z. Chen, F. Panhwar, X. He, Dual Suppression Effect of Magnetic Induction Heating and Microencapsulation on Ice Crystallization Enables Low-Cryoprotectant Vitrification of Stem Cell-Alginate Hydrogel Constructs, ACS applied materials & interfaces 10(19) (2018) 16822-16835.

[180] Y. Cao, G. Zhao, F. Panhwar, X. Zhang, Z. Chen, L. Cheng, C. Zang, F. Liu, Y. Zhao, X. He, The Unusual Properties of Polytetrafluoroethylene Enable Massive-Volume Vitrification of Stem Cells with Low-Concentration Cryoprotectants, Adv Mater Technol 4(1) (2019) 1800289.

[181] S. Stewart, X. He, Intracellular Delivery of Trehalose for Cell Banking, Langmuir 35(23) (2019) 7414-7422.

[182] J.H. Crowe, L.M. Crowe, Preservation of mammalian cells-learning nature's tricks, Nat Biotechnol 18(2) (2000) 145-6.

[183] C. Gläfke, M. Akhoondi, H. Oldenhof, H. Sieme, W.F. Wolkers, Cryopreservation of platelets using trehalose: the role of membrane phase behavior during freezing, Biotechnology Progress 28(5) (2012) 1347-1354.

[184] A. Eroglu, M.J. Russo, R. Bieganski, A. Fowler, S. Cheley, H. Bayley, M. Toner, Intracellular trehalose improves the survival of cryopreserved mammalian cells, Nat Biotechnol 18(2) (2000) 163-7.

[185] G.F. Mastromonaco, L.A. Gonzalez-Grajales, M. Filice, P. Comizzoli, Somatic cells, stem cells, and induced pluripotent stem cells: how do they now contribute to conservation?, Adv Exp Med Biol 753 (2014) 385-427.

[186] K. Jewgenow, F. Göritz, The recovery of preantral follicles from ovaries of domestic cats and their characterisation before and after culture, Animal Reproduction Science 39(4) (1995) 285-297.

[187] E.J. Kim, J. Lee, H.W. Youm, S.K. Kim, J.R. Lee, C.S. Suh, S.H. Kim, Comparison of Follicle Isolation Methods for Mouse Ovarian Follicle Culture In Vitro, Reprod Sci 25(8) (2018) 1270-1278.

[188] H. Huang, G. Zhao, Y. Zhang, J. Xu, T.L. Toth, X. He, Predehydration and Ice Seeding in the Presence of Trehalose Enable Cell Cryopreservation, ACS Biomaterials Science & Engineering 3(8) (2017) 1758-1768.

[189] A. Morizane, D. Doi, T. Kikuchi, K. Nishimura, J. Takahashi, Small-molecule inhibitors of bone morphogenic protein and activin/nodal signals promote highly efficient neural induction from human pluripotent stem cells, J Neurosci Res 89(2) (2011) 117-26.

[190] G. Lee, S.M. Chambers, M.J. Tomishima, L. Studer, Derivation of neural crest cells from human pluripotent stem cells, Nat Protoc 5(4) (2010) 688-701.

[191] S.M. Chambers, C.A. Fasano, E.P. Papapetrou, M. Tomishima, M. Sadelain, L. Studer, Highly efficient neural conversion of human ES and iPS cells by dual inhibition of SMAD signaling, Nat Biotechnol 27(3) (2009) 275-80.

[192] B. Jiang, Z. Xiang, Z. Ai, H. Wang, Y. Li, W. Ji, T. Li, Generation of cardiac spheres from primate pluripotent stem cells in a small molecule-based 3D system, Biomaterials 65 (2015) 103-14.

[193] T.G. Otsuji, J. Bin, A. Yoshimura, M. Tomura, D. Tateyama, I. Minami, Y. Yoshikawa, K. Aiba, J.E. Heuser, T. Nishino, K. Hasegawa, N. Nakatsuji, A 3D sphere culture system containing functional polymers for large-scale human pluripotent stem cell production, Stem Cell Reports 2(5) (2014) 734-45.

[194] M.M. Laronda, F.E. Duncan, J.E. Hornick, M. Xu, J.E. Pahnke, K.A. Whelan, L.D. Shea, T.K. Woodruff, Alginate encapsulation supports the growth and differentiation of human primordial follicles within ovarian cortical tissue, J Assist Reprod Genet 31(8) (2014) 1013-28.

[195] C.A. Amorim, A. Van Langendonckt, A. David, M.M. Dolmans, J. Donnez, Survival of human pre-antral follicles after cryopreservation of ovarian tissue,

follicular isolation and in vitro culture in a calcium alginate matrix, Hum Reprod 24(1) (2009) 92-9.

[196] K.Y. Lee, D.J. Mooney, Alginate: properties and biomedical applications, Prog Polym Sci 37(1) (2012) 106-126.

[197] A. Camboni, A. Van Langendonckt, J. Donnez, J. Vanacker, M.M. Dolmans, C.A. Amorim, Alginate beads as a tool to handle, cryopreserve and culture isolated human primordial/primary follicles, Cryobiology 67(1) (2013) 64-9.

[198] J. Vanacker, C.A. Amorim, Alginate: A Versatile Biomaterial to Encapsulate Isolated Ovarian Follicles, Ann Biomed Eng 45(7) (2017) 1633-1649.

[199] M. Verheijen, M. Lienhard, Y. Schrooders, O. Clayton, R. Nudischer, S. Boerno, B. Timmermann, N. Selevsek, R. Schlapbach, H. Gmuender, S. Gotta, J. Geraedts, R. Herwig, J. Kleinjans, F. Caiment, DMSO induces drastic changes in human cellular processes and epigenetic landscape in vitro, Scientific Reports 9(1) (2019) 1-12.

[200] H. Huang, J.K. Choi, W. Rao, S. Zhao, P. Agarwal, G. Zhao, X. He, Alginate Hydrogel Microencapsulation Inhibits Devitrification and Enables Large-Volume Low-CPA Cell Vitrification, Advanced Functional Materials 25(44) (2015) 6839-6850.

[201] A. Eroglu, M. Toner, T.L. Toth, Beneficial effect of microinjected trehalose on the cryosurvival of human oocytes, Fertil Steril 77(1) (2002) 152-8.

[202] J.J. Pancrazio, F. Wang, C.A. Kelley, Enabling tools for tissue engineering, Biosens Bioelectron 22(12) (2007) 2803-11.

[203] J.H. Crowe, F.A. Hoekstra, L.M. Crowe, Anhydrobiosis, Annual Review of Physiology 54(1) (1992) 579-599.

[204] J.H. Crowe, J.F. Carpenter, L.M. Crowe, THE ROLE OF VITRIFICATION IN ANHYDROBIOSIS, Annual Review of Physiology 60(1) (1998) 73-103.

[205] J.H. Crowe, L.M. Crowe, W.F. Wolkers, A.E. Oliver, X. Ma, J.-H. Auh, M. Tang, S. Zhu, J. Norris, F. Tablin, Stabilization of Dry Mammalian Cells: Lessons from Nature, Integrative and Comparative Biology 45(5) (2005) 810-820.

[206] G.M. Beattie, J.H. Crowe, A.D. Lopez, V. Cirulli, C. Ricordi, A. Hayek, Trehalose: a cryoprotectant that enhances recovery and preserves function of human pancreatic islets after long-term storage, Diabetes 46(3) (1997) 519-23.

[207] I. Puhlev, N. Guo, D.R. Brown, F. Levine, Desiccation tolerance in human cells, Cryobiology 42(3) (2001) 207-17.

[208] X. He, A. Amin, A. Fowler, M. Toner, Thermally Induced Introduction of Trehalose into Primary Rat Hepatocytes., Cell Preservation Technology 4(3) (2006) 178-187.

[209] M. Zhang, H. Oldenhof, H. Sieme, W.F. Wolkers, Freezing-induced uptake of trehalose into mammalian cells facilitates cryopreservation, Biochim Biophys Acta 1858(6) (2016) 1400-9.

[210] M. Zhang, H. Oldenhof, B. Sydykov, J. Bigalk, H. Sieme, W.F. Wolkers, Freeze-drying of mammalian cells using trehalose: preservation of DNA integrity, Sci Rep 7(1) (2017) 6198.

[211] C. Stoll, J.L. Holovati, J.P. Acker, W.F. Wolkers, Synergistic effects of liposomes, trehalose, and hydroxyethyl starch for cryopreservation of human erythrocytes, Biotechnol Prog 28(2) (2012) 364-71.

[212] G.R. Satpathy, Z. Torok, R. Bali, D.M. Dwyre, E. Little, N.J. Walker, F. Tablin, J.H. Crowe, N.M. Tsvetkova, Loading red blood cells with trehalose: a step towards biostabilization, Cryobiology 49(2) (2004) 123-36.

[213] X. Zhou, H. He, B. Liu, T. Hua, Loading Trehalose into Red Blood Cells by Improved Hypotonic Method, Cell Preservation Technology 6(2) (2008) 119-124.

[214] R. Reuss, J. Ludwig, R. Shirakashi, F. Ehrhart, H. Zimmermann, S. Schneider, M.M. Weber, U. Zimmermann, H. Schneider, V.L. Sukhorukov, Intracellular delivery of carbohydrates into mammalian cells through swelling-activated pathways, J Membr Biol 200(2) (2004) 67-81.

[215] R. Shirakashi, C.M. Kostner, K.J. Muller, M. Kurschner, U. Zimmermann, V.L. Sukhorukov, Intracellular delivery of trehalose into mammalian cells by electropermeabilization, J Membr Biol 189(1) (2002) 45-54.

[216] B. Dovgan, A. Barlic, M. Knezevic, D. Miklavcic, Cryopreservation of Human Adipose-Derived Stem Cells in Combination with Trehalose and Reversible Electroporation, J Membr Biol 250(1) (2017) 1-9.

[217] W.F. Wolkers, N.J. Walker, F. Tablin, J.H. Crowe, Human platelets loaded with trehalose survive freeze-drying, Cryobiology 42(2) (2001) 79-87.

[218] A.E. Oliver, K. Jamil, J.H. Crowe, F. Tablin, Loading Human Mesenchymal Stem Cells with Trehalose by Fluid-Phase Endocytosis, Cell Preservation Technology 2(1) (2004) 35-49.

[219] S.Z. Zhang, H. Qian, Z. Wang, J.L. Fan, Q. Zhou, G.M. Chen, R. Li, S. Fu, J. Sun, Preliminary study on the freeze-drying of human bone marrow-derived mesenchymal stem cells, J Zhejiang Univ Sci B 11(11) (2010) 889-94.

[220] N. Guo, I. Puhlev, D.R. Brown, J. Mansbridge, F. Levine, Trehalose expression confers desiccation tolerance on human cells, Nature Biotechnology 18(2) (2000) 168-171.

[221] A. GarcíA De Castro, A. Tunnacliffe, Intracellular trehalose improves osmotolerance but not desiccation tolerance in mammalian cells, FEBS Letters 487(2) (2000) 199-202.

[222] M.J. Russo, H. Bayley, M. Toner, Reversible permeabilization of plasma membranes with an engineered switchable pore, Nature Biotechnology 15(3) (1997) 278-282.

[223] A. Eroglu, M.J. Russo, R. Bieganski, A. Fowler, S. Cheley, H. Bayley, M. Toner, Intracellular trehalose improves the survival of cryopreserved mammalian cells, Nature Biotechnology 18(2) (2000) 163-167.

[224] J.P. Acker, X.-M. Lu, V. Young, S. Cheley, H. Bayley, A. Fowler, M. Toner, Measurement of trehalose loading of mammalian cells porated with a metal-actuated switchable pore, Biotechnology and Bioengineering 82(5) (2003) 525-532.

[225] S.S. Buchanan, S.A. Gross, J.P. Acker, M. Toner, J.F. Carpenter, D.W. Pyatt, Cryopreservation of stem cells using trehalose: evaluation of the method using a human hematopoietic cell line, Stem Cells Dev 13(3) (2004) 295-305.

[226] S.S. Buchanan, M.A. Menze, S.C. Hand, D.W. Pyatt, J.F. Carpenter, Cryopreservation of Human Hematopoietic Stem and Progenitor Cells Loaded with

Trehalose: Transient Permeabilization via the Adenosine Triphosphate-Dependent P2Z Receptor Channel, Cell Preservation Technology 3(4) (2005) 212-222.

[227] G.D. Elliott, X.-H. Liu, J.L. Cusick, M. Menze, J. Vincent, T. Witt, S. Hand, M. Toner, Trehalose uptake through P2X7 purinergic channels provides dehydration protection, Cryobiology 52(1) (2006) 114-127.

[228] N. Chakraborty, M.A. Menze, H. Elmoazzen, H. Vu, M.L. Yarmush, S.C. Hand, M. Toner, Trehalose transporter from African chironomid larvae improves desiccation tolerance of Chinese hamster ovary cells, Cryobiology 64(2) (2012) 91-6.

[229] T. Uchida, M. Furukawa, T. Kikawada, K. Yamazaki, K. Gohara, Intracellular trehalose via transporter TRET1 as a method to cryoprotect CHO-K1 cells, Cryobiology 77 (2017) 50-57.

[230] A. Eroglu, S.E. Bailey, M. Toner, T.L. Toth, Successful cryopreservation of mouse oocytes by using low concentrations of trehalose and dimethylsulfoxide, Biol Reprod 80(1) (2009) 70-8.

[231] A. Eroglu, J.A. Lawitts, M. Toner, T.L. Toth, Quantitative microinjection of trehalose into mouse oocytes and zygotes, and its effect on development, Cryobiology 46(2) (2003) 121-34.

[232] P. Bhowmick, A. Eroglu, D.L. Wright, M. Toner, T.L. Toth, Osmometric behavior of mouse oocytes in the presence of different intracellular sugars, Cryobiology 45(2) (2002) 183-7.

[233] A.L. Lynch, R. Chen, P.J. Dominowski, E.Y. Shalaev, R.J. Yancey, Jr., N.K. Slater, Biopolymer mediated trehalose uptake for enhanced erythrocyte cryosurvival, Biomaterials 31(23) (2010) 6096-103.

[234] D.M. Sharp, A. Picken, T.J. Morris, C.J. Hewitt, K. Coopman, N.K. Slater, Amphipathic polymer-mediated uptake of trehalose for dimethyl sulfoxide-free human cell cryopreservation, Cryobiology 67(3) (2013) 305-11.

[235] A.L. Lynch, R. Chen, N.K. Slater, pH-responsive polymers for trehalose loading and desiccation protection of human red blood cells, Biomaterials 32(19) (2011) 4443-9.

[236] S.A. Mercado, N.K. Slater, Increased cryosurvival of osteosarcoma cells using an amphipathic pH-responsive polymer for trehalose uptake, Cryobiology 73(2) (2016) 175-80.

[237] Y. Wei, C. Li, L. Zhang, X. Xu, Design of novel cell penetrating peptides for the delivery of trehalose into mammalian cells, Biochim Biophys Acta 1838(7) (2014) 1911-20.

[238] J.L. Holovati, M.I.C. Gyongyossy-Issa, J. Acker, Investigating Interactions of Trehalose-Containing Liposomes with Human Red Blood Cells, Cell Preservation Technology 6(2) (2008) 133-146.

[239] J.L. Holovati, M.I.C. Gyongyossy-Issa, J.P. Acker, Effects of trehalose-loaded liposomes on red blood cell response to freezing and post-thaw membrane quality, Cryobiology 58(1) (2009) 75-83.

[240] J.P. Motta, F.H. Paraguassu-Braga, L.F. Bouzas, L.C. Porto, Evaluation of intracellular and extracellular trehalose as a cryoprotectant of stem cells obtained from umbilical cord blood, Cryobiology 68(3) (2014) 343-8.

[241] W. Zhang, J. Rong, Q. Wang, X. He, The encapsulation and intracellular delivery of trehalose using a thermally responsive nanocapsule, Nanotechnology 20(27) (2009) 275101.

[242] S. Zhang, J. Fan, X. Xu, G. Chen, F. Zhu, L. Yan, An experimental study of the use of ultrasound to facilitate the loading of trehalose into platelets, Cryobiology 59(2) (2009) 135-40.

[243] A. Abazari, L.G. Meimetis, G. Budin, S.S. Bale, R. Weissleder, M. Toner, Engineered Trehalose Permeable to Mammalian Cells, PLOS ONE 10(6) (2015) e0130323.

[244] M.P. Rols, Electropermeabilization, a physical method for the delivery of therapeutic molecules into cells, Biochim Biophys Acta 1758(3) (2006) 423-8.

[245] I. Kaasen, J. McDougall, A.R. Strom, Analysis of the otsBA operon for osmoregulatory trehalose synthesis in Escherichia coli and homology of the OtsA and OtsB proteins to the yeast trehalose-6-phosphate synthase/phosphatase complex, Gene 145(1) (1994) 9-15.

[246] J.S. Wiley, R. Sluyter, B.J. Gu, L. Stokes, S.J. Fuller, The human P2X7 receptor and its role in innate immunity, Tissue Antigens 78(5) (2011) 321-32.

[247] E. Adinolfi, C. Pizzirani, M. Idzko, E. Panther, J. Norgauer, F. Di Virgilio, D. Ferrari, P2X(7) receptor: Death or life?, Purinergic Signal 1(3) (2005) 219-27.

[248] E. Adinolfi, L. Raffaghello, A.L. Giuliani, L. Cavazzini, M. Capece, P. Chiozzi, G. Bianchi, G. Kroemer, V. Pistoia, F. Di Virgilio, Expression of P2X7 receptor increases in vivo tumor growth, Cancer Res 72(12) (2012) 2957-69.

[249] M. Watanabe, T. Kikawada, T. Okuda, Increase of internal ion concentration triggers trehalose synthesis associated with cryptobiosis in larvae of Polypedilum vanderplanki, J Exp Biol 206(Pt 13) (2003) 2281-6.

[250] T. Kikawada, Factors Inducing Successful Anhydrobiosis in the African Chironomid Polypedilum vanderplanki: Significance of the Larval Tubular Nest, Integrative and Comparative Biology 45(5) (2005) 710-714.

[251] K.T. Watanabe M, Minagawa N, Yukhiro F, Okuda T, Mechanism allowing an insect to survive complete dehydration and extreme temperatures, Journal of Experimental Biology 205 (2002) 2799-2802.

[252] T. Kikawada, A. Saito, Y. Kanamori, Y. Nakahara, K. Iwata, D. Tanaka, M. Watanabe, T. Okuda, Trehalose transporter 1, a facilitated and high-capacity trehalose transporter, allows exogenous trehalose uptake into cells, Proc Natl Acad Sci U S A 104(28) (2007) 11585-90.

[253] S. Ramadurai, M. Werner, N.K.H. Slater, A. Martin, V.A. Baulin, T.E. Keyes, Dynamic studies of the interaction of a pH responsive, amphiphilic polymer with a DOPC lipid membrane, Soft Matter 13(20) (2017) 3690-3700.

[254] A.S.S. Hoffman, P. S.; El-Sayed, M. E. H.; Murthy, N.; Bulmus, V.; Lackey, C.; Cheung, C., Design of "Smart" Nano-Scale Delivery Systems for Biomolecular Therapeutics, Journal of Biomedical Nanotechnology, 3(3) (2007) 213-217.

[255] R. Chen, S. Khormaee, M.E. Eccleston, N.K. Slater, The role of hydrophobic amino acid grafts in the enhancement of membrane-disruptive activity of pH-responsive pseudo-peptides, Biomaterials 30(10) (2009) 1954-61.

[256] A.L. Lynch, N.K. Slater, Influence of intracellular trehalose concentration and pre-freeze cell volume on the cryosurvival of rapidly frozen human erythrocytes, Cryobiology 63(1) (2011) 26-31.

[257] Y.L. Boce Zhang, Hongda Chen, Nanotechnology Applications to Improve Food Safety, in: J.C. Joseph J. Jen (Ed.), Food Safety in China: Science, Technology, Management and Regulation, Wiley2017, pp. 609-635.

[258] D. Banerjee, S. Sengupta, Nanoparticles in cancer chemotherapy, Prog Mol Biol Transl Sci 104 (2011) 489-507.

[259] M. Breunig, S. Bauer, A. Goepferich, Polymers and nanoparticles: intelligent tools for intracellular targeting?, Eur J Pharm Biopharm 68(1) (2008) 112-28.

[260] J.K. Vasir, V. Labhasetwar, Biodegradable nanoparticles for cytosolic delivery of therapeutics, Adv Drug Deliv Rev 59(8) (2007) 718-28.

[261] S.H. Choi, S.H. Lee, T.G. Park, Temperature-sensitive pluronic/poly(ethylenimine) nanocapsules for thermally triggered disruption of intracellular endosomal compartment, Biomacromolecules 7(6) (2006) 1864-70.

[262] M. Prabaharan, Review paper: chitosan derivatives as promising materials for controlled drug delivery, J Biomater Appl 23(1) (2008) 5-36.

[263] W. Zhang, K. Gilstrap, L. Wu, R.B. K. C, M.A. Moss, Q. Wang, X. Lu, X. He, Synthesis and Characterization of Thermally Responsive Pluronic F127−Chitosan Nanocapsules for Controlled Release and Intracellular Delivery of Small Molecules, ACS Nano 4(11) (2010) 6747-6759.